QUADRUPOLE MOMENTS IN THE LEAD ISOTOPES

BY

ANDRÉ MARTHE ROGER JOYE

A thesis submitted to
The Australian National University
for the degree of
Doctor of Philosophy
May 1977

To My Parents

PREFACE

This thesis describes a series of experiments designed to measure the quadrupole moments of the first excited states of the stable even-mass lead isotopes. The work was carried out in the Department of Physics and in the Department of Nuclear Physics at the Australian National University under the supervision of Dr A.M. Baxter.

The project was initiated by Dr D.C. Kean, and the work was carried out jointly by him, Dr A.M. Baxter, Dr R.H. Spear, and myself. The experimental arrangement was designed by Dr M.T. Esat, Dr Kean, and Dr Spear. The method used to calibrate the 14UD Pelletron accelerator was devised largely by Dr Kean and the analysis of the energy calibration data was performed by myself. The procedure for making thin, highly uniform, lead chloride targets was developed by myself. The lineshape fitting program was written by me and the extraction of excitation probabilities from the raw data was performed largely by me, with some assistance from Dr Baxter. The remainder of the data analysis, including the writing of a least-squares program for determining $B(E\lambda)$ and $Q_{J\pi}$ values from the measured excitation probabilities, and modifications to the Coulomb excitation computer program, were performed by myself.

Some of the work described in this thesis has appeared or will appear in the following publications:

(1) The Quadrupole Moment of the First 3^- State in ^{208}Pb, A.M.R. Joye, A.M. Baxter, M.P. Fewell, D.C. Kean, and R.H. Spear, Phys. Rev. Lett. 38 (1977) 807.

(2) Static Quadrupole Moments of the First Excited States of ^{204}Pb and ^{206}Pb,
A.M.R. Joye, A.M. Baxter, R.H. Spear, and D.C. Kean,
to be published.

(3) Energy Calibration of the A.N.U. 14UD Pelletron Accelerator,
R.H. Spear, D.C. Kean, M.T. Esat, A.M.R. Joye, and M.P. Fewell,
to be published in Nucl. Instr. Meth.

It has been a pleasure to work with Dr Baxter, and I take this opportunity to thank him for his valuable supervision and assistance during the course of this work. I am particularly grateful for his willingness to read and comment on the preliminary draft of this thesis while on sabbatical leave. A special note of thanks is due to Dr Kean not only for his great interest and participation at all stages of this work, but also for his constructive criticism during the writing of this thesis. I would like to express my sincere thanks to Dr Spear for his considerable involvement in this work, and to Professor S. Hinds for the many valuable discussions I have had with him. Finally, I would like to thank Mr M.P. Fewell and Dr T.H. Zabel for their willingness to help with data accumulation without hesitation.

I have enjoyed working in the Department of Physics and I am grateful to Professor S. Hinds for giving me this opportunity. I would also like to thank Professor J.O. Newton for extending to me the use of the excellent facilities at the Department of Nuclear Physics.

No part of this thesis has been submitted for a degree at any other university.

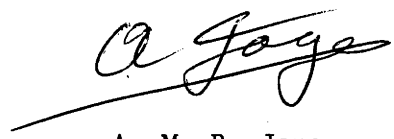

A. M. R. Joye

Canberra,
May 1977.

TABLE OF CONTENTS

ABSTRACT

The static quadrupole moments $Q_{J\pi}$ and reduced excitation probabilities (BEλ) of the first excited states of the nuclei ^{204}Pb, ^{206}Pb, and ^{208}Pb have been determined using the reorientation effect in Coulomb excitation. The Coulomb excitation probabilities were measured by resolving inelastically and elastically backward-scattered ^{4}He, ^{12}C, and ^{16}O projectiles in an annular surface barrier detector. In the case of ^{204}Pb and ^{206}Pb, safe bombarding energies were determined for all projectiles. In the case of ^{208}Pb, safe bombarding energies were measured for ^{16}O, but were assumed for ^{4}He. The small values obtained for Q_{2+} indicate that ^{204}Pb is only weakly deformed, and that ^{206}Pb approaches sphericity. The measured value of Q_{3-} for ^{208}Pb is much smaller in magnitude than those obtained in previous measurements, and is consistent with most theoretical predictions.

CHAPTER 1

INTRODUCTION

Although Coulomb excitation has been used for many years to study the collective properties of nuclei (Al56), it was not until 12 years ago that de Boer et al. (deBo65) used the reorientation effect in Coulomb excitation to measure the electric quadrupole moment of the first 2^+ excited state of ^{114}Cd. The unexpectedly large static quadrupole moment ($Q_{2+} = -0.70 \pm 0.21$ eb) measured by de Boer et al. aroused considerable interest since such a large value was contrary to the previously well-established picture of ^{114}Cd as a typical vibrational nucleus. In subsequent years, a number of processes (for example, Coulomb-nuclear interference, virtual excitation via the giant dipole resonance, and the attenuation of gamma-ray angular distributions) which can significantly affect the results deduced from reorientation measurements have come to light, and consequently results from early experiments have been found to be unreliable. However, the elucidation of these processes and advances in experimental techniques have improved the reliability of reorientation measurements, and in the last few years the reorientation effect has become a useful tool to measure the quadrupole moment of excited states in nuclei from ^{18}O (Fe77) to ^{208}Pb.

The present thesis reports the measurement of the electric quadrupole moment of the first excited states of the isotopes ^{204}Pb, ^{206}Pb, and ^{208}Pb. The dramatic discrepancy between the experimental and theoretical values for the quadrupole moment Q_{3-} of the 2.61 MeV 3^- state in ^{208}Pb, has aroused considerable attention in recent years. While most theoretical calculations give Q_{3-} between - 0.09eb and - 0.20 eb (Gu75), Barnett et al. (Ba69) have measured a value

$Q_{3-} = -1.3 \pm 0.6$ eb and, in a subsequent experiment (Ba72), reported $Q_{3-} = -0.9 \pm 0.4$ eb or -1.1 ± 0.4 eb, depending on the value assumed for Q_{2+} in ^{206}Pb. It is therefore of considerable interest to resolve the large discrepancy between the theoretical values and previous experimental results.

The problem regarding Q_{3-} in ^{208}Pb provided an incentive for investigating the quadrupole moments Q_{2+} of the first 2^+ states in ^{204}Pb and ^{206}Pb. There have been no previous measurements of Q_{2+} for ^{206}Pb, and only one value $Q_{2+} = +0.19 \pm 0.14$ eb has been reported (0174) for ^{204}Pb. These two nuclei are of further interest because they lie between the doubly-magic nucleus ^{208}Pb, and the so-called transition region $A = 192 - 194$ where nuclei are known to change shape from prolate ($A \lesssim 190$) to oblate ($A \gtrsim 196$). Moreover, the quadrupole moments Q_{2+} for ^{204}Pb and ^{206}Pb provide a good test for the shell model which has been found to be particularly successful in the regions of double closed shells.

In the present chapter, some simple theoretical models are described with particular emphasis on predictions for $Q_{J\pi}$ and reduced transition probabilities; more advanced theoretical treatments will be discussed in chapter 6. Section 1.5 shows how nuclear shapes can be treated in terms of relatively few collective parameters, and a model-independent method for determining these parameters from experimental data is described. However, a precise definition of electric quadrupole moments will first be given.

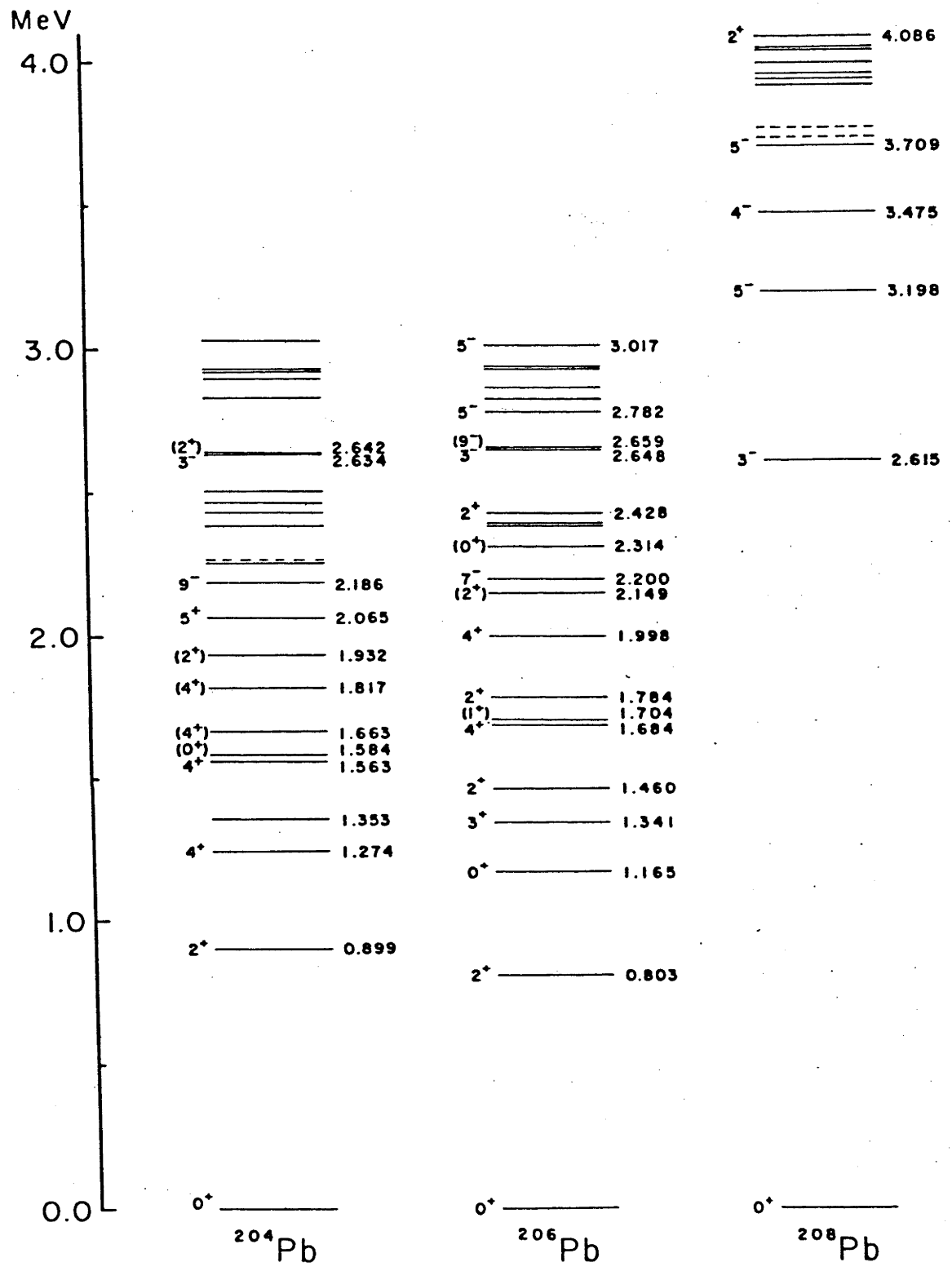

Fig. 1.1 Energy level schemes for the isotopes ^{204}Pb, ^{206}Pb, and ^{208}Pb. (Data taken from Ma71, Se72, and Le71.)

1.1 The Electric Quadrupole Moment

The static electric quadrupole moment is a measure of the extent to which the nuclear charge distribution deviates from spherical symmetry. Classically the quadrupole moment of a charge distribution is defined as

$$e\,Q = \int (3z^2 - r^2)\rho\, d\tau \tag{1.1}$$

where ρ is the charge density. Clearly for a spherical charge distribution $Q = 0$. A charge distribution stretched in the z direction (prolate) will give a positive quadrupole moment (in the intrinsic frame of reference - see section 1.5), and an oblate distribution will give a negative quadrupole moment. In a quantum-mechanical treatment the charge density ρ is replaced by the probability density $|\,|JJ\rangle\,|^2$ and the spectroscopic quadrupole moment is defined by

$$e\,Q_{J\pi} = e\,\langle JJ|(3z^2 - r^2)|JJ\rangle \tag{1.2a}$$

$$= e\,\langle JJ|(16\pi/5)^{\frac{1}{2}} r^2 Y_{20}(\theta,\phi)|JJ\rangle \tag{1.2b}$$

where Y_{20} is a spherical harmonic function, (r,θ,ϕ) are the nuclear coordinates, and the term $|J,M=J\rangle$ represents the wave function of a nuclear state with spin J and z-component $M=J$. Equation (1.2) can be generalized to higher-order moments

$$e\,Q_{J\pi}^{(\lambda)} = e\,\langle JJ|[16\pi/(2\lambda+1)]^{\frac{1}{2}}\, r^{\lambda} Y_{\lambda o}(\theta,\phi)|JJ\rangle\ . \tag{1.3}$$

However, since nuclear states have a definite parity they cannot have

odd-order electric multipole moments; in particular, the dipole moment is zero. The quadrupole moment is therefore the lowest order deformation which can occur.

Quantum-mechanically, the only externally detectable quantity having a definite direction in a nucleus is its total angular momentum J; the measured spectroscopic quadrupole moment therefore depends on the orientation of the charge distribution relative to that of J. When $J = 0$ no direction can be defined; all directions must be given equal weight and hence $Q_{J\pi} = 0$. Angular momentum coupling rules imply that for $J = 1/2$ $Q_{J\pi} = 0$.

1.2 The Extreme Single-Particle Shell Model

In terms of the extreme single-particle shell model, the ground state quadrupole moment of an odd-proton nucleus can be calculated from eq. (1.2) with an appropriate wave function $|jj\rangle$ for the proton. The result for the quadrupole moment due to a single proton (sp) is (Ma55),

$$Q_{sp} = - e \frac{2j - 1}{2j + 2} \langle r^2 \rangle \qquad (1.4)$$

where $\langle r^2 \rangle$ is the mean square distance of the proton from the centre of the nucleus. The negative sign in eq. (1.4) reflects the concentration of the particle density in the equatorial plane for the magnetic substate $m = j$. For a single proton-hole, the quadrupole moment is $-Q_{sp}$. An odd-neutron nucleus has a quadrupole moment due to the recoil motion of the rest of the nucleus. For a neutron located at r_n, with respect to the centre of mass, the rest of the nucleus represents a charge Z at a distance $r_n/(A-1)$ from the centre of mass, and the effective quadrupole moment is

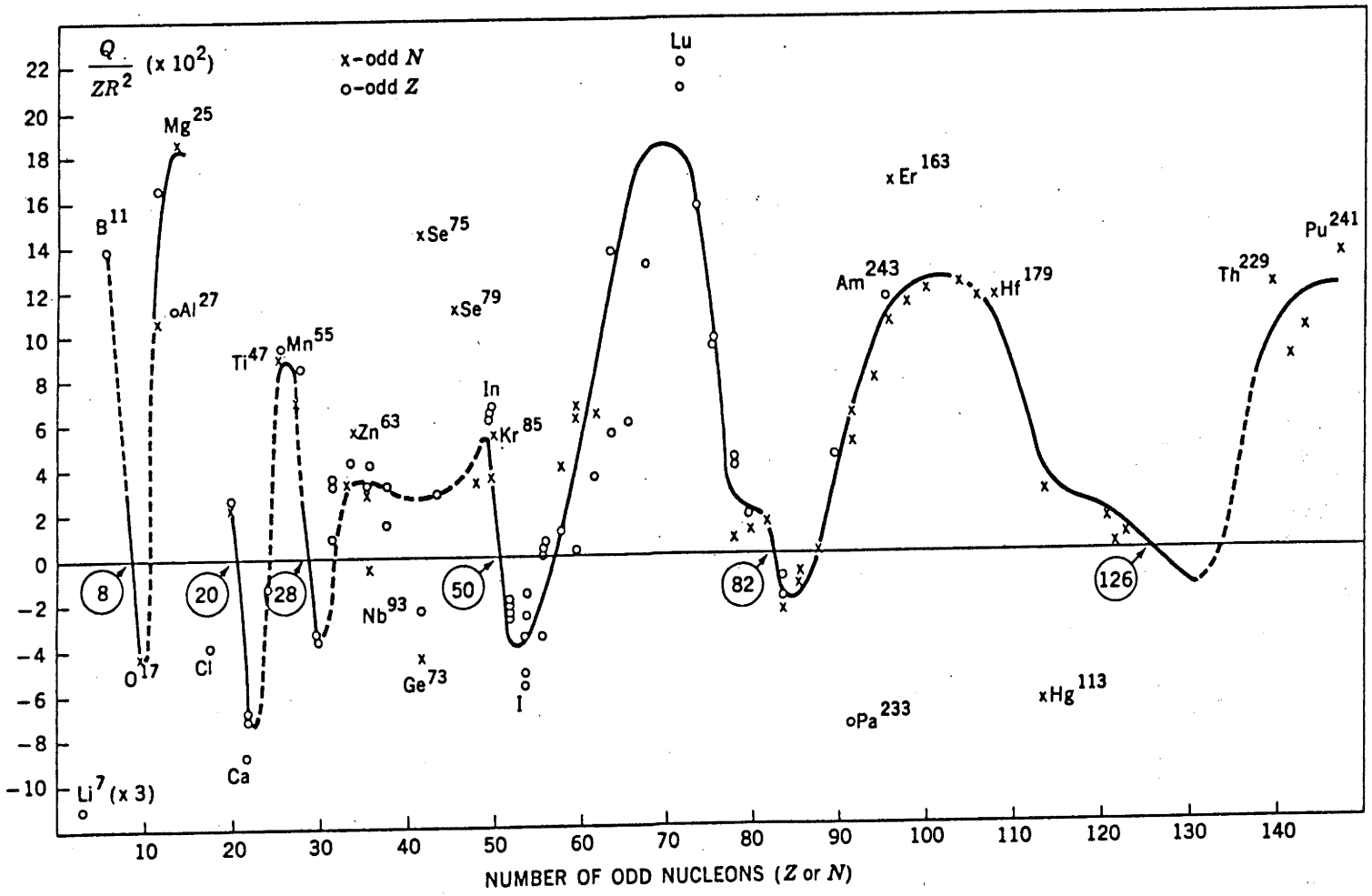

Fig. 1.2. Quadrupole moments of ground states of odd-mass nuclei (from Co71)

$$Q_{sn} = \frac{Z}{(A-1)^2} Q_{sp} . \qquad (1.5)$$

Fig. 1.2 shows the systematic trends in the ground state quadrupole moments of nuclei as a function of the number of odd nucleons; the quantity $Q/Z R^2$ (where $R = 1.07A^{1/3}$ fm) is a measure of nuclear deformation. According to the extreme single-particle model the value of Q/ZR^2 should be $\sim 1/Z$ for an odd-proton nucleus, and $\sim 1/(A-1)^2$ for an odd-neutron nucleus. Fig. 1.2 shows that the change in Q from positive to negative as the nuclear number goes through closed shells is correctly predicted, and that the magnitude of Q/ZR^2 in these regions roughly agrees. However, in regions away from closed shells there are a number of major discrepancies:

a) The predicted values are much too small in magnitude.

b) When Q is fairly large, there is no difference in the order of magnitude of the quadrupole moments of odd-proton and odd-neutron nuclei.

c) There is a preponderance of positive quadrupole moments.

These discrepancies indicate that the simple single-particle model is too naive and that a large number of nucleons contribute to the observed quadrupole moments.

1.3 The Vibrational Model

In the simple vibrational model, it is assumed that the nucleus performs harmonic vibrations about the spherical shape. The vibrations of the surface are represented by

$$R(\theta,\phi,t) = R_o[1 + \Sigma_{\lambda\mu}\, \alpha_{\lambda\mu}(t)\, Y_{\lambda\mu}(\theta,\phi)] \qquad (1.6)$$

through the time dependence of the amplitude $\alpha_{\lambda\mu}(t)$. The terms with $\lambda = 0$ and $\lambda = 1$ in eq. (1.6) do not give rise to surface oscillations; $\lambda = 0$ represents a compression (or dilatation) without change of shape (because nuclear matter is almost incompressible, these vibrations have high excitation energies), and the terms with $\lambda = 1$ are associated with a displacement of the centre of mass. The surface oscillations of lowest order are therefore the quadrupole mode with $\lambda = 2$.

In quantum mechanics, the vibrations can be treated as phonons with angular momentum λ, z-component μ, and energy $\hbar\omega_\lambda$. In the simple vibrational model, the vibrational states can have excitation energies

$$\Delta E_N = \hbar\omega_\lambda N_\lambda \qquad N_\lambda = 0,1,2,... \qquad (1.7)$$

where N_λ is the number of phonons. Phonons obey Bose-Einstein statistics (i.e. they are bosons). For example, two quadrupole ($\lambda = 2$) phonons can give rise to degenerate states with spins $0^+, 2^+$, and 4^+. In a real nucleus, the degeneracy is removed, and the observation in numerous nuclei (e.g. the even-mass Cd isotopes) of a $0^+, 2^+, 4^+$ triplet at twice the excitation energy of the one-phonon 2^+ state has been taken as evidence for the occurrence of collective vibrations. Collective 3^- states due to one octupole phonon have also been observed in several nuclei (for example the even-mass Pb and Cd isotopes). One-octupole-phonon states have higher excitation energies than one-quadrupole-phonon states and the liquid-drop model (which assumes an imcompressible charged fluid and irrotational flow) predicts $\hbar\omega_3 \approx 2\hbar\omega_2$ The sequence of levels expected from the simple vibrational model is shown in fig. 1.3.

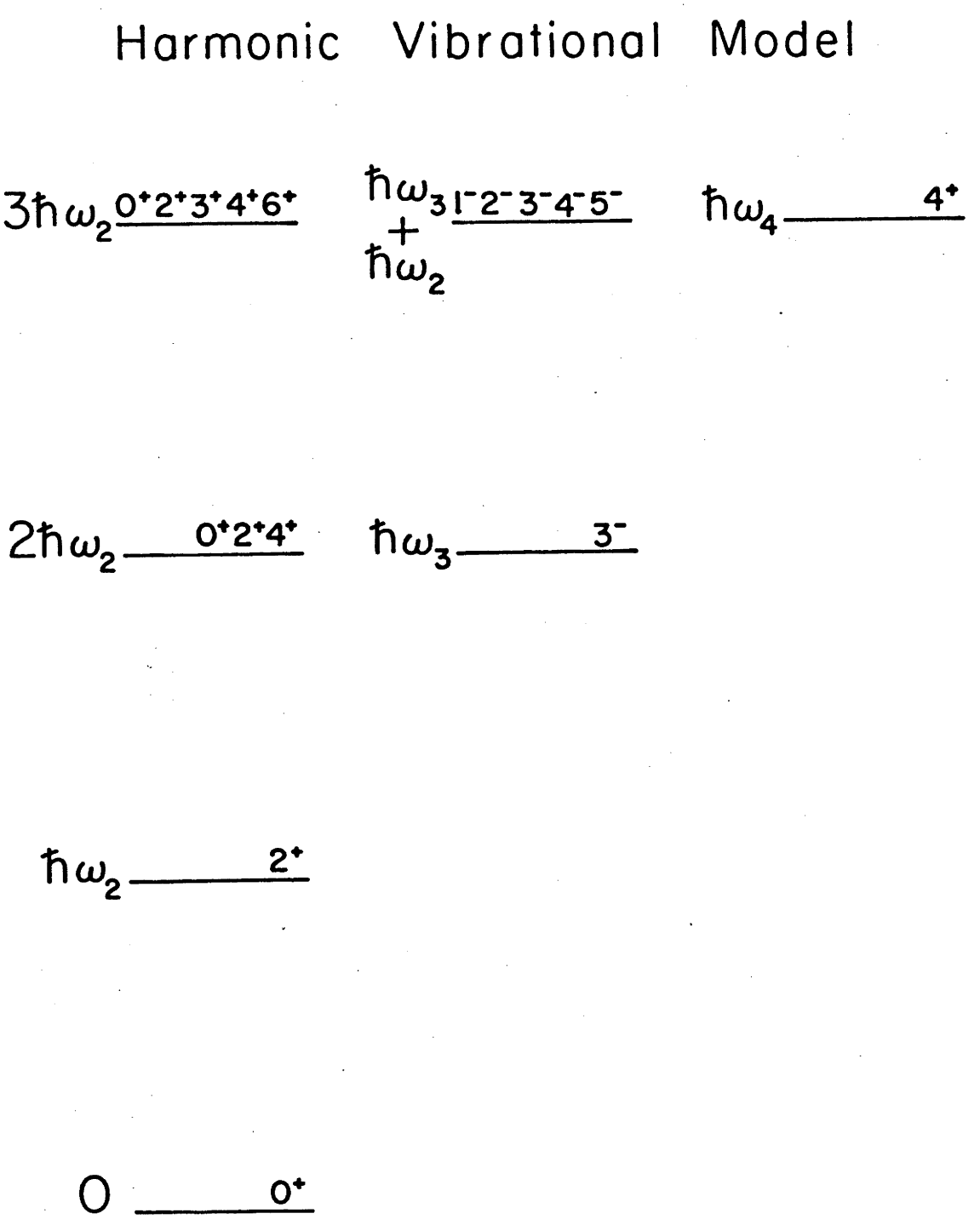

Fig. 1.3 Energy level scheme predicted by the simple harmonic vibrational model.

The simple vibrational model predicts the relation

$$B(E\lambda;\ N_\lambda = 2 \rightarrow N_\lambda = 1) \ = \ 2\ B(E\lambda;\ N_\lambda = 1 \rightarrow N_\lambda = 0) \qquad (1.8)$$

between the reduced transition probabilities for the two- and one-phonon states. Transitions between vibrational states are governed by the selection rule $\Delta N_\lambda = \pm 1$; matrix elements $\langle N_\lambda || E\lambda || N'_\lambda \rangle$ are zero unless this rule is satisfied. As a consequence of the selection rule "cross-over" transitions are forbidden and static electric quadrupole moments are zero. For $\lambda = 2$, both these predictions have been found to disagree with experiment - "good vibrators" such as ^{114}Cd have non-zero quadrupole moments, and $2^{+'} \rightarrow 0^+$ transitions have been observed, although these are much weaker than $2^{+'} \rightarrow 2^+$ transitions.

1.4 The Rotational Model

In the simple rotational model (see for example, Bo75), the nucleus is assumed to be a spheroid possessing axial symmetry. Levels composing the ground state rotational band of an even-even nucleus have spins and parities $J^\pi = 0^+, 2^+, 4^+, 6^+, \ldots$ and the energy spacing between these levels is proportional to $J(J+1)$. For this rotational band, the reduced transition probabilities are given by

$$B(E2;\ J+2 \rightarrow J) \ = \ \frac{15}{32\pi} \ \frac{(J+1)(J+2)}{(2J+3)(2J+5)}\ e^2 \left(Q^i_{rot}\right)^2 \qquad (1.9)$$

where Q^i_{rot} is the intrinsic quadrupole moment defined with respect to the symmetry axis of the nucleus. In the rotational model, the spectroscopic quadrupole moment Q_{J^π} of a state J^π is related to

Q^i_{rot} by

$$Q_{J^\pi} = \frac{3K^2 - J(J+1)}{(J+1)(2J+3)} Q^i_{rot} \qquad (1.10)$$

where K is the projection of J on the nuclear symmetry axis. In the ground state band of an even-even nucleus, $K = 0$ and Q_{J^π} will be negative for prolate shapes ($Q^i_{rot} > 0$). Combining eqs. (1.9) and (1.10), one obtains for the 2^+ state of the ground state band the relation

$$|Q_{J^\pi}| = 0.9059[B(E2; 0^+ \rightarrow 2^+)]^{\frac{1}{2}} \qquad (1.11)$$

which defines the so-called "rotational value" for the quadrupole moment.

1.5 Intrinsic Shapes

Since the nuclear shape has a profound influence on the collective properties of a nucleus, it is clearly desirable to introduce the concept of an intrinsic quadrupole moment Q^i, taken relative to the principal axis (axis of symmetry) of the nucleus. The intrinsic quadrupole moment Q^i is not only more closely related to the shape of the nucleus than the spectroscopic quadrupole moment Q_{J^π}, but it does not suffer the problem of Q_{J^π} which becomes zero for $J = 0$ or $\frac{1}{2}$. The intrinsic quadrupole moment is of theoretical interest because in many theoretical models it is related to observable quantities such as the reduced excitation probabilities and Q_{J^π}. The concept of an intrinsic quadrupole moment was introduced in the rotational model but in this simple model the nucleus was assumed to have a fixed spheroidal shape, which has axial symmetry.

In general, a nucleus is not necessarily axially symmetric and the nuclear shape is not fixed; instead, the nucleus can spend

a fraction of its time in various shapes. In this section, a scheme to treat nuclear shapes, in general, in terms of few collective parameters, is discussed; later, a model-independent method for determining these parameters from experimental data, will be described.

1.5.1 Generalized Treatment of Nuclear Shapes

In the present section, the nucleus is treated as an equivalent ellipsoid (as opposed to a spheroid which is axially symmetric), as shown in fig. 1.4, with the same charge, volume, and quadrupole moment. Higher-order deformations are ignored. The intrinsic coordinate system is defined by the principal axes of the ellipsoid and because of reflection symmetry it follows that $\alpha_{21} = \alpha_{2-1} = 0$ and $\alpha_{22} = \alpha_{2-2}$ for the $\alpha_{2\mu}$ coefficients in eq. (1.6). Therefore, instead of characterising a randomly oriented ellipsoid with five $\alpha_{2\mu}$ coefficients, its shape is characterised by α_{20} and α_{22} and its orientation in space is described by three Eulerian angles. The two deformation variables α_{20} and α_{22} are usually (see for example Bo75,p677ff) expressed in terms of the parameters β and γ defined by

$$\alpha_{20} = \beta \cos\gamma \quad \text{and} \quad \alpha_{22} = 2^{-\frac{1}{2}} \beta \sin\gamma \, . \tag{1.12}$$

Using eqs. (1.6), (1.12) and the definition of spherical harmonics, the length of the three principal axes can be written as

$$R_k = R_o[1 + \delta \cos(\gamma - \tfrac{2}{3}\pi k)] \tag{1.13}$$

where $k = 1,2,3$ correspond to the x',y',z' axes in fig. 1.4 and

$$\delta = [5/(4\pi)]^{\frac{1}{2}} \beta \, . \tag{1.14}$$

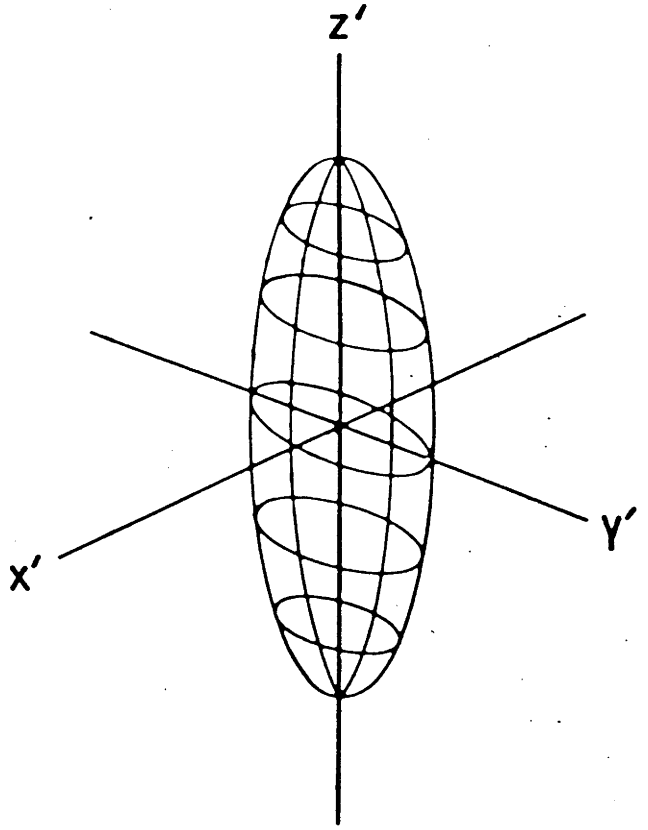

Fig. 1.4 Ellipsoidal shape for quadrupole deformation with β and γ positive (from Hy64).

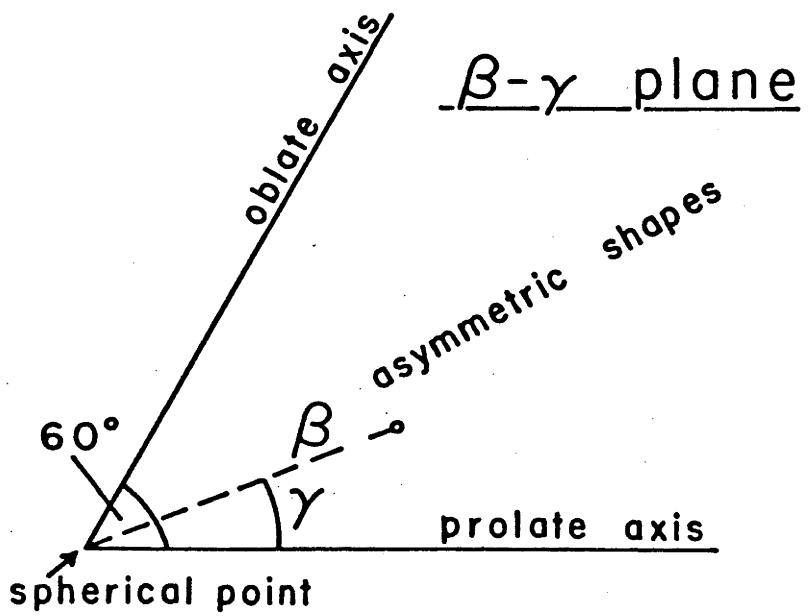

Fig. 1.5 The parameters β and γ as polar coordinates in the β-γ plane.

In eq. (1.13) it is sufficient to consider only positive values of β and values of γ in the range $0^o - 60^o$; other values correspond to a relabelling of the axes. From eq. (1.13), it can be seen that $\beta = 0$ corresponds to a spherical shape ($R_1 = R_2 = R_3$); $\beta > 0$, $\gamma = 0^o$ to a prolate shape ($R_1 = R_2 < R_3$); $\beta > 0$, $\gamma = 60^o$ to an oblate shape ($R_1 = R_3 > R_2$); and $\beta > 0$, $0^o < \gamma < 60^o$ to asymmetric shapes ($R_1 \neq R_2 \neq R_3$).

Any ellipsoidal shape can be represented by a point (β,γ) on a two-dimensional polar diagram as in fig. 1.5; the distance of a point from the origin equals the deformation parameter β and the polar angle corresponds to the asymmetry parameter γ. In figs. 1.6 - 1.8 the potential energy of quadrupole deformation $V(\beta,\gamma)$ is plotted on $\beta\gamma$ diagrams for three extreme cases:

a) Fig. 1.6 shows $V(\beta,\gamma)$ for an anharmonic vibrator. It can be seen that a minimum occurs at $\beta = 0$, corresponding to a spherical nucleus, and that the potential is almost independent of γ. The potential energy of deformation is obtained as a function of β by plotting the values of $V(\beta,\gamma)$ along the $\gamma = 0^o$ and $\gamma = 60^o$ axes (note that $(\beta,60^o) \equiv (-\beta,0^o)$ and this is shown on the left of the figure (the dashed line represents a harmonic vibrator). The expected energy level scheme is shown on the right of fig. 1.6; it can be seen that the two- and three-phonon states are no longer degenerate.

b) Typical prolate and oblate nuclei are represented in fig. 1.7. These nuclei have very deep minima at $\beta = 0.4$ and are permanently deformed. Both nuclei have an identical energy level scheme (shown on the right of the figure).

c) Fig. 1.8a shows $V(\beta,\gamma)$ for a triaxially deformed nucleus with permanent β and γ deformations. The rotational energy level scheme according to the Davydov-Filippov model (Da58) is shown in fig. 1.8b.

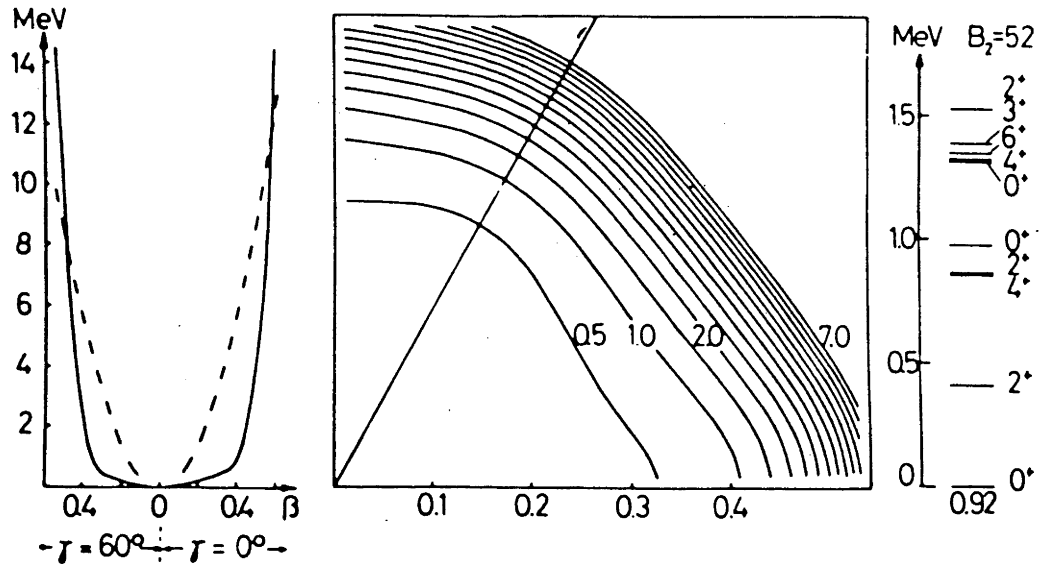

Fig. 1.6. Contour plot of $V(\beta,\gamma)$ and energy level scheme of an anharmonic vibrator (from Be75).

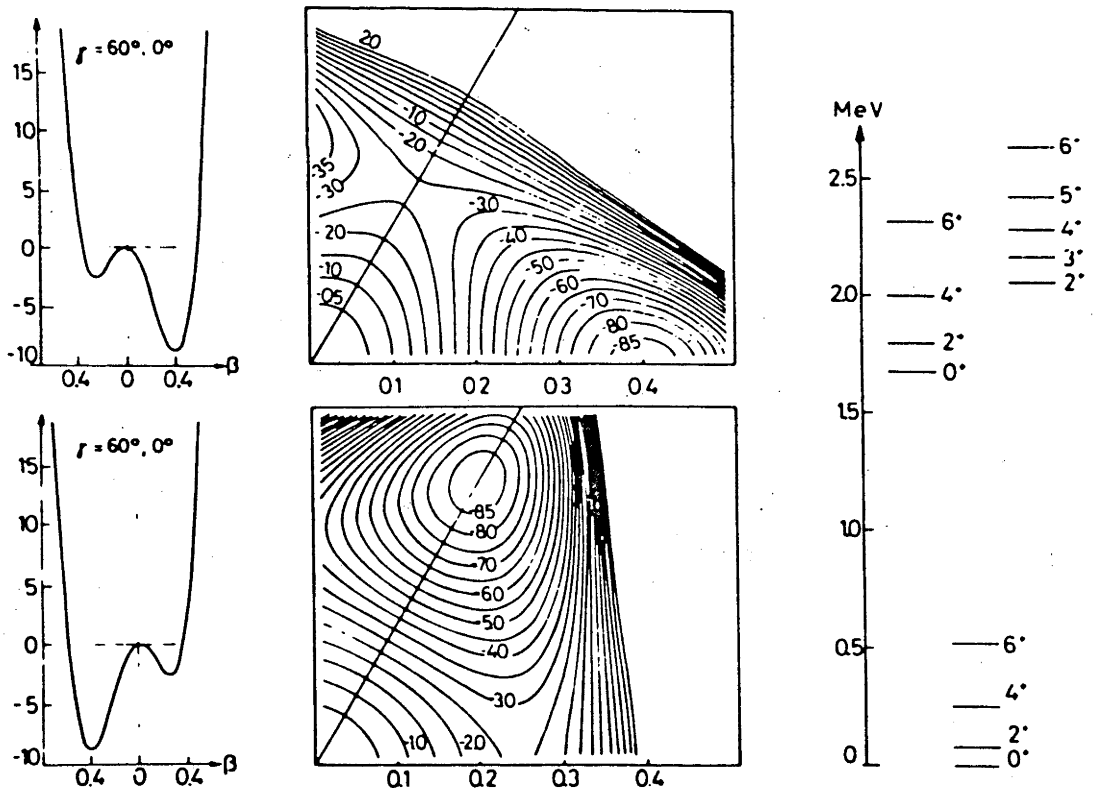

Fig. 1.7 Contour plots of $V(\beta,\gamma)$, and energy level scheme of a prolate (top) and oblate (bottom) deformed nucleus (from Be75).

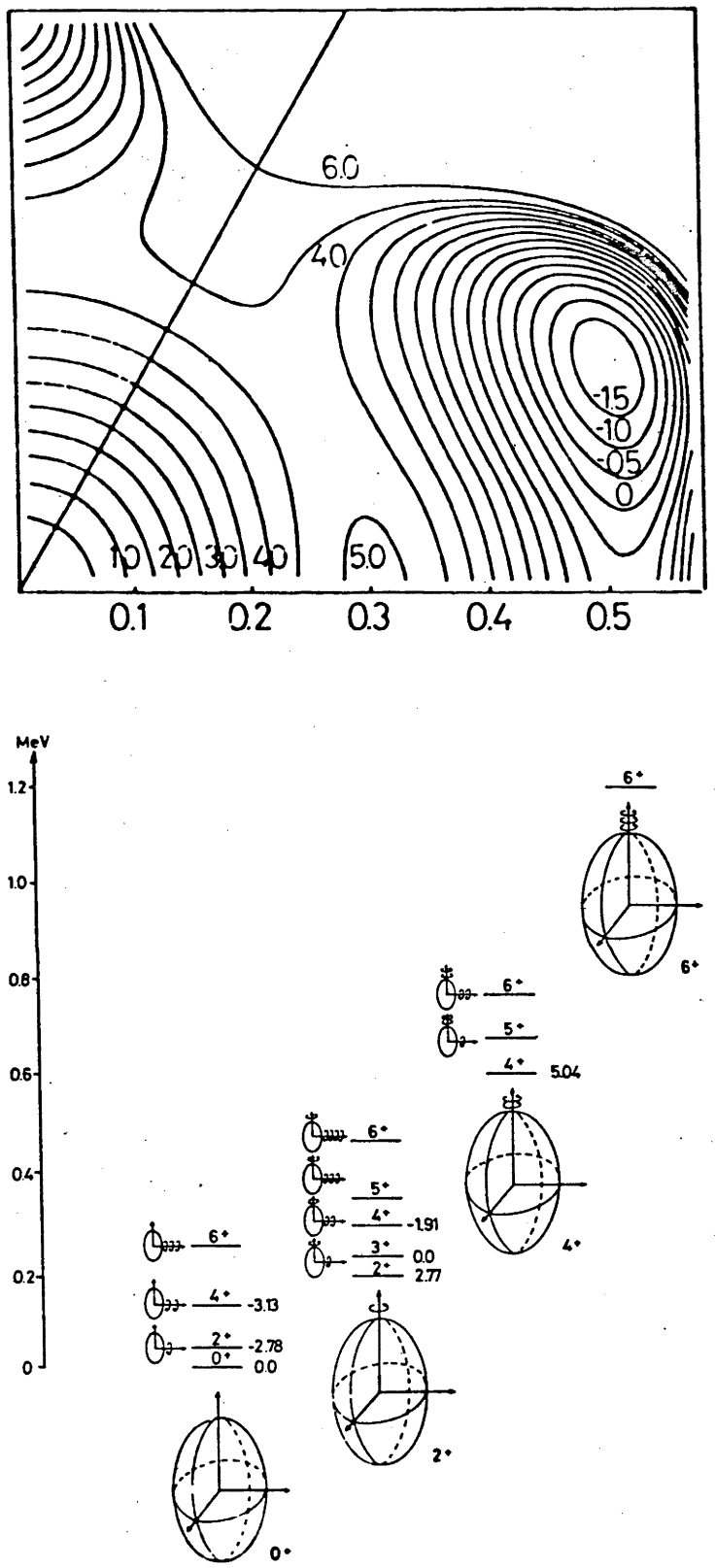

Fig. 1.8. Triaxially deformed nucleus - (a) contour plot of $V(\beta,\gamma)$, (b) corresponding energy level scheme according to the Davydov-Filippov model (from Be75).

1.5.2 The Sum-Rule Method

Kumar (Ku72, Ku75) has suggested a model-independent sum-rule method using electromagnetic data to determine experimental values of collective parameters in the intrinsic frame of reference. An extended version of this method was used by Cline (Cl72, Cl72a) to analyse E2 data in several regions of the periodic table. Although the method has been described in detail by Kumar and by Cline, a brief outline is given below. The sums

$$P_s^{(2)} = (2J_s+1)^{-1} \sum_r |\langle s||E2||r\rangle|^2 \qquad (1.15)$$

and

$$P_s^{(3)} = -5^{\frac{1}{2}} (2J_s+1)^{-1}(-1)^{2J_s} \sum_{rt} \begin{Bmatrix} 2 & 2 & 2 \\ J_s & J_r & J_t \end{Bmatrix} \langle s||E2||r\rangle \times \langle r||E2||t\rangle \langle t||E2||s\rangle \qquad (1.16)$$

(where s, r, and t refer to nuclear states) are evaluated using the reduced matrix elements obtained from experiment. The intrinsic quadrupole moment Q_s^i and the asymmetry parameter γ_s^i are obtained from

$$Q_s^i = \left((16\pi/5)\, P_s^{(2)}\right)^{\frac{1}{2}} \qquad (1.17)$$

and

$$\mathrm{Cos}\, 3\gamma_s^i = -(7/2)^{\frac{1}{2}} P_s^{(3)} \left(P_s^{(2)}\right)^{-3/2} . \qquad (1.18)$$

The sums $P_s^{(2)}$ and $P_s^{(3)}$ are the expectation values (multiplied by a factor of $\sqrt{5}$) of the zero-coupled products of E2 tensor operators $\{E2 \times E2\}^0$ and $\{[E2 \times E2]^2 \times E2\}^0$ respectively. These sums are invariant under rotation of the coordinate frame and have the same value in both the laboratory and intrinsic frames. Higher-order sums $P_s^{(4)}$ and $P_s^{(6)}$ can be used to determine the fluctuations in the magnitude and in the

asymmetry of the nuclear deformation, but a larger number of states must be included in the analysis in order to give meaningful results. It must be emphasized that the values of Q_s^i and γ_s^i, determined according to the above method, are completely model independent and can be treated as observables; these parameters are a convenient way of representing strongly correlated data such as Q_{J^π} and B(E2).

To interpret the results of the sum rule method in terms of the nuclear shape, the adiabatic approximation must be used and certain assumptions must be made concerning the charge distribution (for example, a uniform distribution of charges, and a sharp cut-off) and, to this extent, the nuclear shape which is deduced becomes model dependent. As before, the nucleus is treated as an ellipsoid, and the parameters (β_s,γ_s) which describe the ellipsoid are related to the intrinsic observables (Q_s^i, γ_s^i) by $\gamma_s = \gamma_s^i$ and by

$$\beta_s = (\pi/5)^{\frac{1}{2}} Q_s^i \left(Z \langle s|r^2|s\rangle\right)^{-1} . \qquad (1.19)$$

The value of the mean square charge radius $\langle s|r^2|s\rangle$ can be obtained directly from electron-scattering or from mu-mesic data. Alternatively, following the procedure outlined by Kumar, $\langle s|r^2|s\rangle$ may be expressed in terms of the radius R of a sphere of equivalent volume. (In the present work $R = 1.2\ A^{1/3}$ fm.) If the latter procedure is followed, then in the limit of small deformation, eq. (1.19) reduces to

$$\beta_s = (5\pi)^{\frac{1}{2}}/3 \quad Q_s^i \left(Z\ R^2\right)^{-1} , \qquad (1.20)$$

which is the relation of Bohr and Mottelson (Bo53) for a spheroid. The effect of this approximation is to change β_s by less than 1% for values of $\beta < 0.16$.

The sum-rule method will be applied in chapter 6 for a systematic study of the shapes of nuclei between A = 184 and A = 206.

CHAPTER 2

THE MEASUREMENT OF QUADRUPOLE MOMENTS

In the present chapter, the different experimental methods which can be used to measure electric quadrupole moments are briefly described. Since in the present work quadrupole moments were determined from the reorientation effect in Coulomb excitation, the relevant aspects of Coulomb excitation theory are discussed. Some important effects which can affect the value of $Q_{J\pi}$ obtained from reorientation experiments, and which must be taken into account, are also treated. At the end of this chapter, an outline is also given of a computer program which was used to calculate excitation probabilities from Coulomb excitation theory.

2.1 Methods for Measuring Quadrupole Moments of Excited States

The most common method of determining a nuclear quadrupole moment $Q_{J\pi}$ to measure its interaction with an electric field gradient. Most experiments measure the interaction energy, and this is proportional to the product of the quadrupole moment and the electric field gradient (Ja62 eq. (4.17)). To extract $Q_{J\pi}$, the electric field gradient must then either be calculated or measured independently. For an axially symmetric spheroid with symmetry axis z exposed to a constant electric field gradient dE/dz, the interaction energy may be written quantum mechanically as (Hä74),

$$E_Q = \frac{1}{4} e Q_{J\pi} (dE/dz) [3M^2 - J(J+1)] / J(2J-1) \qquad (2.1)$$

where J is the spin and M is the magnetic quantum number of the

nuclear state. For states with $J = 0$ or $\frac{1}{2}$ the interaction energy is zero; as discussed in section 1.5, this does not imply that the intrinsic quadrupole moment Q^i, which is referred to the symmetry axis, is necessarily zero. Since the interaction is quadratic in M, states whose magnetic quantum numbers differ only in sign are degenerate. (This degeneracy can be removed by the presence of an additional magnetic field.) When $M = J$ the interaction energy reaches a maximum,

$$E_Q = \frac{1}{4} e Q_{J\pi}(dE/dz) \qquad M = J . \tag{2.2}$$

The various ways of producing an electric field gradient at the nuclear site give rise to the different experimental methods employed. These methods have been described by de Boer and Eichler (deBo68), McGowan and Stelson (McGo74), Häusser (Hä74), Bodenstedt (Bo75a), and references therein, and are briefly outlined below.

a) External field gradients

The highest electric field gradients that can be produced by external electrodes in the laboratory are of the order of $10^{14} V\,cm^{-2}$, giving rise to a maximum interaction energy $E_Q \approx 10^{-11} eV$ for $Q_{J\pi} = 1\,b$. This is too small to be measured experimentally.

b) The Mössbauer Method

In crystalline solids a nucleus situated at a lattice point can be subject to strong local electric (and magnetic) fields, usually referred to as hyperfine fields. In the Mössbauer method, the absorber is made by implanting the nucleus being studied in a host lattice with a low order of symmetry and, in this way, hyperfine fields up to $10^{18} Vcm^{-2}$ can be obtained at the nuclear site. The source consists

of the same nuclei embedded in a cubic crystal lattice where, because of symmetry, the hyperfine fields are zero. (This is sometimes referred to as an unsplit source.) The absorber nuclei are excited by resonant gamma-ray absorption and then interact with the hyperfine field causing a splitting of the magnetic substates of the states taking part in the transition (providing their spin $> \frac{1}{2}$) . The energy shifts are of the order of $10^{-7} - 10^{-6}$ eV and can be measured from the absorption spectrum. The source and absorber must be cooled to minimise lattice vibrations and gamma-rays must have energies low enough ($\lesssim$ 200 keV) so that they are emitted without recoil. The major uncertainty in the values obtained for quadrupole moments arises from the uncertainty in the strength of the hyperfine field at the nuclear site. These uncertainties are usually large, and Mössbauer measurements at present are more useful in providing ratios of quadrupole moments for different nuclear states or for different isotopes.

c) Perturbed angular correlation experiments

As for the Mössbauer method the nucleus being studied is implanted in a crystal lattice. The interaction of the quadrupole moment with the electric hyperfine field causes a precession of the nucleus which perturbs the angular distribution of the deexcitation gamma rays. From the precession frequency $\omega_Q = E_Q/\hbar$ and knowledge of the hyperfine field, $Q_{J\pi}$ can be determined. Two methods have been used to measure ω_Q:

1) A single crystal source or target is prepared and the time-integrated correlation (or distribution) is observed as a function of the orientation of the crystal symmetry axis. The precession frequency is obtained from the measured attenuation coefficients. (These are a

function of $(\omega_Q\tau)^2$, where τ is the lifetime of the state.)

2) A polycrystaline source or target can be used and the angular correlation (or distribution) is obtained as a function of time (differential method).

These methods are applicable provided that the mean lifetime τ of the state is greater than the period of precession; i.e. $\tau \gtrsim \hbar/E_Q \approx 10^{-9}$ sec. The main drawback of this technique is that the accuracy of the measured $Q_{J\pi}$ is limited by the accuracy with which the electric field gradient can be determined. Furthermore, because of the M^2 degeneracy (eq. (2.1)) the sign of the interaction E_Q and hence that of $Q_{J\pi}$ can only be determined by measuring the circular polarization of one of the gamma rays, by polarising the initial state, or by measuring the β-γ directional correlation with an unpolarized source.

In addition to using radioactive nuclei implanted in crystals, other nuclei can be studied using recoil implantation; nuclei following nuclear reactions or Coulomb excitation recoil to implant themselves in a suitable target backing (Gr70,B172). This method, however, has the additional complication of changes to the electric field gradient due to radiation damage to the crystal lattice (He71).

d) Muonic X-rays

A muon moving in a lower atomic orbit can spend a large fraction of its time inside the nuclear volume, and this feature can be used to probe the nuclear charge distribution. The muonic orbits are $m_\mu/m_e = 200$ times closer to the nucleus than the corresponding electronic orbits and electric field gradients are therefore much larger. The hyperfine interaction can give rise to energy shifts $E_Q^{(\mu)} \approx 100$ keV

and this is comparable to the excitation energies of low-lying nuclear levels so that the muonic X-rays and nuclear gamma rays are strongly mixed. The quadrupole hyperfine splitting is proportional to $Q_{J\pi}Z^3$ and with present Ge(li) detectors the method is limited to nuclei with $Z \gtrsim 25$. The value of $Q_{J\pi}$ is obtained by assuming a shape for the radial nuclear charge distribution and this is model dependent.

e) Inelastic scattering

It is possible to obtain a measure of the nuclear deformation by measuring cross sections for inelastic scattering of protons, deuterons, and helium ions at energies where the nuclear interaction predominates. (This method then does not rely on the electromagnetic interaction.) These data are analysed in terms of a model describing the nuclear surface using a deformed optical potential and the method of coupled channels (to include multipole excitations). A model-dependent value of $Q_{J\pi}$ can then be determined from the set of parameters giving the best fit to the data.

f) Coulomb excitation

Coulomb excitation refers to the process whereby the close passage of a charged particle (the projectile) can give rise to transitions from the ground state to excited states in a target nucleus. If the excited nucleus is deformed, it will have a quadrupole moment $Q_{J\pi}$ which can interact with the time-dependent electric field gradient produced by the projectile. The interaction between $Q_{J\pi}$ and the electric field gradient causes the magnetic substates to be split in energy (see eq. (2.1)) and because of the strong dependence of the Coulomb excitation probability on excitation energy, the extent to which the various magnetic substates are populated therefore depends

on $Q_{J\pi}$. The change in population of the magnetic substates corresponds to a reorientation of the nuclear spin axis and this forms the basis for the term "reorientation effect" (Br55,Br56).

Whether or not the target nucleus (A_2,Z_2) and the projectile (A_1,Z_1) come within the range of nuclear forces, Coulomb excitation will occur. However, if the initial bombarding energy E of the projectile is low enough, the distance of closest approach (between centres and assuming spherical nuclei)

$$d = 1.44(1 + A_1/A_2)Z_1Z_2/E \quad \text{fm} \tag{2.3}$$

will be sufficiently large that Coulomb excitation is essentially the only process taking place. Energies for which this is the case are referred to as "safe energies" and a more quantitative definition of these will be given in chapter 5. The reason for performing experiments at safe energies is that the Coulomb interaction is well understood whereas a model must be assumed for the nuclear interaction.

The reorientation effect has been used to measure quadrupole moments of the first excited states of stable even-even nuclei from ^{18}O to ^{208}Pb. The quadrupole moments of higher states can, in principle, also be measured (see for example O'Br77) but multiple excitation via lower excited states is an important effect (in addition to interference from higher excited states; see subsection 2.2.4) and the relevant matrix elements must be known to a high accuracy if $Q_{J\pi}$ is to be determined with reasonably small errors. The theoretical basis of Coulomb excitation is described in detail in section 2.2 and a survey of experimental techniques is made in chapter 3.

2.2 Semiclassical Coulomb Excitation Theory

Coulomb excitation theory is now well established and a number of excellent treatments of the subject have been given by Alder et al. (Al56), de Boer and Eichler (deBo68), Häusser (Hä74), McGowan and Stelson (McGo74), Newton (Ne75), and by Alder and Winther (Al75). While only a quantum mechanical treatment is rigorously correct, an insight into the physical processes that take place is more easily gained from semiclassical theory and computations of excitation probabilities are considerably simplified. In many cases, the two are in close agreement and as will be shown later, it is possible to modify the results from semiclassical theory to account for quantal effects. The remainder of this section will therefore deal only with semiclassical theory.

2.2.1 General Description

The most significant approximation in semiclassical theory is the treatment of the dynamics of the Coulomb excitation process in terms of classical Rutherford scattering; that is, particles are assumed to follow hyperbolic orbits. For this approximation to be valid, the following conditions must be satisfied:

1) The ratio of the distance of closest approach d, to the de Broglie wavelength λ of the projectile must be large; this is parametrised in terms of

$$\eta = d/2\lambda\!\!\!^{-} = a/\lambda\!\!\!^{-} = Z_1 Z_2 \, e^2/\hbar v_i >> 1 \qquad (2.4)$$

where $\lambda\!\!\!^{-} = \lambda/2\pi$, a is half the distance of closest approach, and v_i is the initial velocity of the projectile in the centre of mass system.

2) The energy ΔE of the excited state must be small compared to the bombarding energy of the projectile, i.e. $\Delta E/E \ll 1$, so that the energy loss of the projectile does not unduly modify the orbit. By using the symmetrised velocity $v = (v_i v_f)^{\frac{1}{2}}$ (where v_f is the final projectile velocity), the semiclassical treatment can be made to correspond more closely to the correct quantal solution.

Assuming that conditions 1) and 2) are satisfied, the excitation cross section for a level f is given in the centre of mass system by

$$(d\sigma/d\Omega)_f = P_{if} (d\sigma/d\Omega)_R \tag{2.5}$$

where P_{if} is the probability of excitation from an initial level i to a final level f, and $(d\sigma/d\Omega)_R$ is the cross section for elastic scattering given by the Rutherford law,

$$(d\sigma/d\Omega)_R = (1/4)\, a^2 \sin^{-4} (\theta/2) \tag{2.6}$$

where θ is the centre of mass scattering angle.

The probability P_{if} for the excitation is given by

$$P_{if} = (2J_i + 1)^{-1} \sum_{M_i M_f} |b_{if}|^2 \tag{2.7}$$

where M_i and M_f are the magnetic substate quantum numbers of the initial and final states and the b_{if} are the transition amplitudes between the magnetic substates $|J_i M_i\rangle$ and $|J_f M_f\rangle$. Note that in eq. (2.7) it is assumed that the initial state is unpolarized and that any polarization of the final state is undetected; one therefore averages over the magnetic substates of the initial state (giving the $(2J_i + 1)^{-1}$ factor) and sums over the final substates.

2.2.2 Perturbation Theory

Time-dependent perturbation theory (see Di66 for example) may be used to evaluate transition amplitudes. To second order, the transition amplitude from an initial magnetic substate $|J_i M_i\rangle$ to a final magnetic substate $|J_f M_f\rangle$ is expressed as

$$b_{if}^{(2)} = b_{if}^{(1)} + \sum_n b_{inf} \tag{2.8}$$

where $b_{if}^{(1)}$ is the first order transition amplitude

$$b_{if}^{(1)} = (i\hbar)^{-1} \int_{-\infty}^{\infty} \langle J_f M_f | H_{int}(t) | J_i M_i \rangle \exp(it(E_f - E_i)/\hbar) dt \tag{2.9}$$

and

$$b_{inf} = (i\hbar)^{-2} \int_{-\infty}^{\infty} \langle J_f M_f | H_{int}(t) | J_n M_n \rangle \exp(it(E_f - E_n)/\hbar) dt \times \int_{-\infty}^{t} \langle J_n M_n | H_{int}(t') | J_i M_i \rangle \exp(it'(E_n - E_i)/\hbar) dt' \tag{2.10}$$

where the subscript n refers to an intermediate state.

In this case, the time-dependent Hamiltonian $H_{int}(t)$ refers to the Coulomb interaction and, treating the projectile as a point charge Ze, it is given classically by

$$H_{int}(t) = \int \frac{\rho(\underset{\sim}{r})Ze}{|\underset{\sim}{r} - \underset{\sim}{R}(t)|} \, dV \tag{2.11}$$

where $\underset{\sim}{R}(t)$ is the position of the projectile in the centre of mass system, $\rho(\underset{\sim}{r})$ is the charge density of the protons in the nucleus, dV is a volume element at position $\underset{\sim}{r}$, and the integration is over all the nuclear volume. Equation (2.11) can be expanded in terms

of multipole moments (Ja62),

$$H_{int}(t) = 4\pi\, Ze \sum_{\lambda=1}^{\infty} \sum_{\mu=-\lambda}^{\lambda} (2\lambda+1)^{-1}\, R^{-\lambda-1}\, Y_{\lambda\mu}(\theta_p,\phi_p)\, M^{*}(E\lambda,\mu) \tag{2.12}$$

where $Y_{\lambda\mu}(\theta_p,\phi_p)$ is a spherical harmonic and $M(E\lambda,\mu)$ is the nuclear electric multipole operator of order λ. The monopole-monopole term is already accounted for by the prescribed motion along a Rutherford orbit and is therefore not included in eq. (2.12). With this latter expression for $H_{int}(t)$ it may be shown (see Al56 for example) that the transition amplitude $b_{if}^{(1)}$ is proportional to the matrix element $\langle J_i M_i | M(E\lambda,\mu) | J_f M_f \rangle$ which in turn is proportional to the reduced matrix element $\langle J_i || M(E\lambda) || J_f \rangle$; similarly, b_{inf} is proportional to the product $\langle J_i || M(E\lambda) || J_n \rangle \langle J_n || M(E\lambda) || J_f \rangle$.

By substituting the second-order transition amplitude (eq. (2.8)) into eq. (2.7), the total excitation probability may be expressed as

$$P_{if} = P_{if}^{(11)} + \sum_n P_{inf}^{(12)} \tag{2.13}$$

where

$$P_{if}^{(11)} \propto \langle J_i || M(E\lambda) || J_f \rangle |^2 \tag{2.14}$$

represents the first-order excitation probability, and

$$P_{inf}^{(12)} \propto \langle J_i || M(E\lambda) || J_f \rangle \langle J_i || M(E\lambda) || J_n \rangle \langle J_n || M(E\lambda) || J_f \rangle \tag{2.15}$$

arises from interference between first and second order excitation. Higher order terms $P^{(22)}$ are small and have not been included. For a three level system, the types of processes that may give rise to

the terms in eq. (2.15) are shown pictorially in fig. 2.1, and are discussed in more detail in subsections 2.2.3 and 2.2.4.

The first-order excitation probability is given explicitly by

$$P_{if}^{(11)} = F(\theta,\xi)\, B(E\lambda;\ i \to f) \tag{2.16}$$

where $F(\theta,\xi)$ is an excitation function. The reduced transition probability

$$B(E\lambda;\ i \to f) = (2\,J_i + 1)^{-1} |\langle J_i || M(E\lambda) || J_f \rangle|^2 \tag{2.17}$$

is related to the partial width Γ_λ for decay by a gamma ray of multipolarity $E\lambda$ from state f to state i by

$$\Gamma_\lambda = \frac{8\pi(\lambda+1)}{\lambda[(2\lambda+1)!!]^2} \cdot \left(\frac{E_\gamma}{\hbar c}\right)^{2\lambda+1} \cdot B(E\lambda;\ f \to i) \tag{2.18}$$

(see Sk67 for example) where E_γ is the energy of the gamma ray. The function $F(\theta,\xi)$ is a maximum at $\theta = 180^\circ$ and decreases slowly with decreasing angle until at forward angles it falls off rapidly. The function $F(\theta,\xi)$ is strongly dependent on the adiabaticity parameter ξ which is the ratio of the collision time a/v and the period of the nuclear transition $\hbar/\Delta E$, i.e.

$$\xi = a\Delta E/(\hbar v)\ . \tag{2.19}$$

The excitation will be strong when $\xi \lesssim 1$ and can be shown to fall off approximately as $\exp(-2\pi\xi)$ when $\xi >> 1$ (Bi65). Clearly, the higher the excitation energy of a state, the less strongly it will be excited.

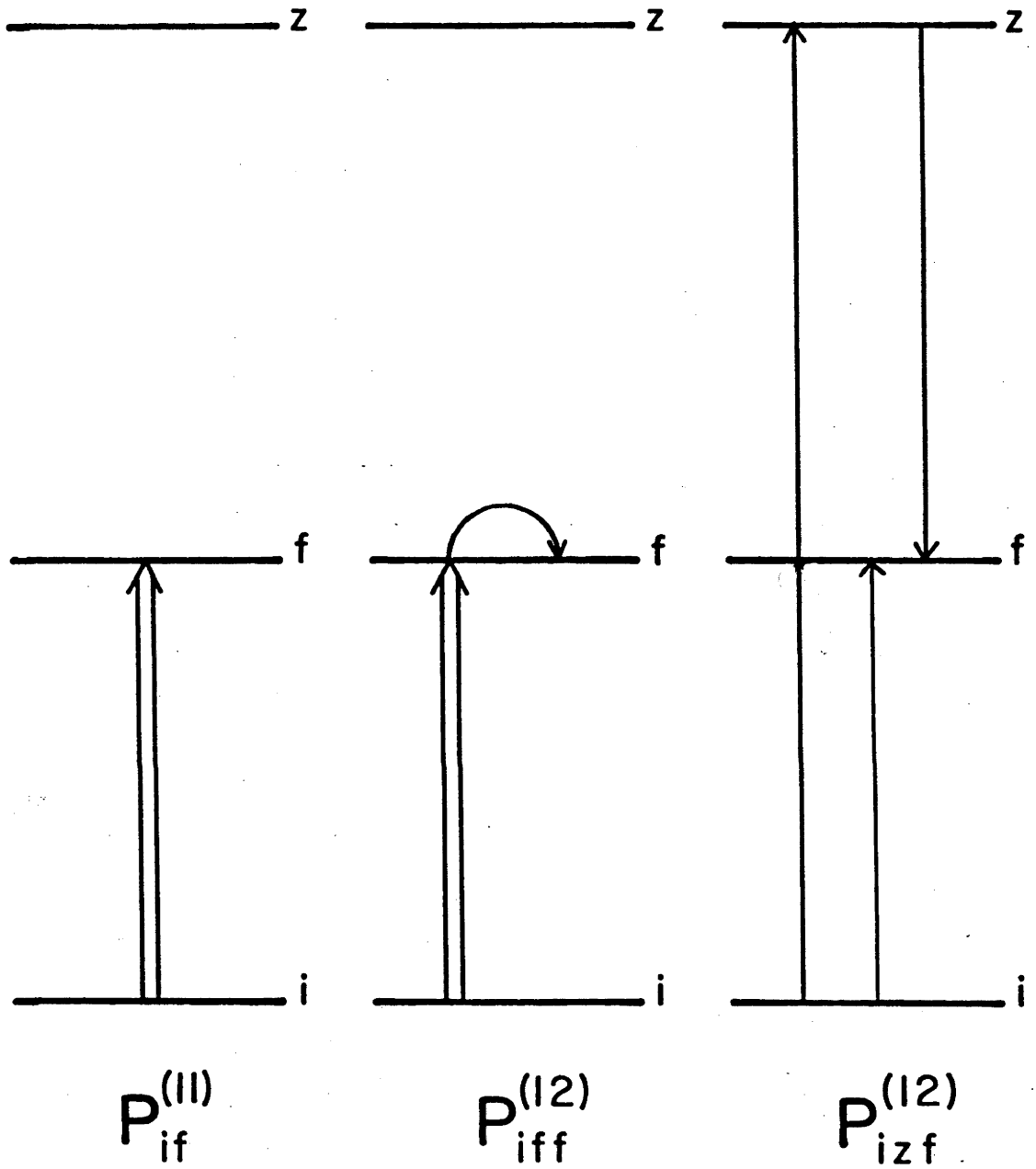

Fig. 2.1 Schematic representation of first order (double arrow) and second order (single arrow) processes for cases where n = f and n = z. The centre diagram represents the reorientation effect and the right hand diagram represents excitation via a higher state.

2.2.3 The Reorientation Effect

If the intermediate state n is in fact one of the magnetic substates of f then (2.15) becomes

$$P_{iff}^{(12)} \propto \left|\langle J_i||M(E\lambda)||J_f\rangle\right|^2 \langle J_f||M(E\lambda)||J_f\rangle \quad . \tag{2.20}$$

The observed static electric multipole moments of state f are related to the reduced matrix element $\langle J_f||M(E\lambda)||J_f\rangle$; for the quadrupole moment the relation for a state with spin J is

$$Q_{J^\pi} = \left(\frac{16\pi}{5}\right)^{\frac{1}{2}} \left[\frac{J(2J-1)}{(J+1)(2J+1)(2J+3)}\right]^{\frac{1}{2}} \langle J||M(E2)||J\rangle \quad . \tag{2.21}$$

The term $P_{iff}^{(12)}$ therefore represents the reorientation effect. The size of the reorientation effect can be compared to that of first order excitation by considering the quantity

$$P_{iff}^{(12)} \Big/ P_{if}^{(11)} = \rho(\theta,\xi) Q_{J^\pi} \tag{2.22}$$

where $\rho(\theta,\xi)$ is the sensitivity parameter given by

$$\rho(\theta,\xi) = k_J \frac{A_1}{Z_2} \frac{\Delta E}{(1+A_1/A_2)} K(\theta,\xi) \tag{2.23}$$

where

$$k_J = (175/32\pi)^{\frac{1}{2}} \approx 1.32 \quad \text{for} \quad J = 2$$

$$k_J = (21/4\pi)^{\frac{1}{2}} \approx 1.29 \quad \text{for} \quad J = 3 \ .$$

The dependence of the function $K(\theta,\xi)$ on θ and ξ is shown in fig. 2.2. Clearly, a large projectile mass and a large scattering angle will increase the size of the reorientation effect. The reorientation effect is also larger for states with high excitation energies.

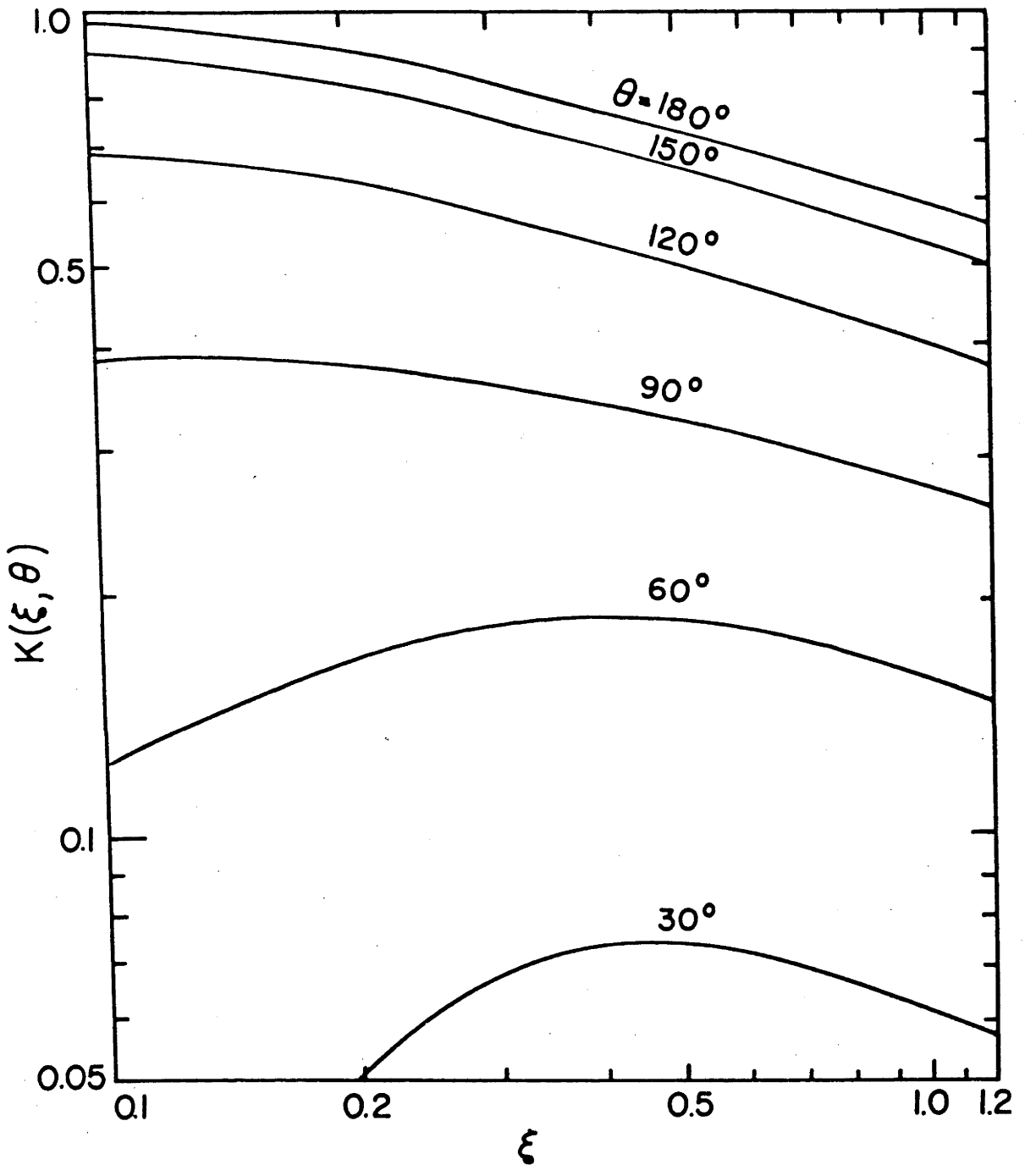

Fig. 2.2. The function $K(\theta,\xi)$ in eq. (2.23) (from deBo68)

Considering only first-order excitation and reorientation, one can then write (from eqs. (2.13), (2.16), and (2.22)) the excitation probability as

$$P_{if} = F(\theta,\xi)\, B(E\lambda;\ i \to f)\, [1 + \rho(\theta,\xi) Q_{J\pi}] \ . \qquad (2.24)$$

The dependence of P_{if} on $Q_{J\pi}$ can be used to determine $Q_{J\pi}$, and such experiments are described in detail in section 3.1.

2.2.4 Interference from Higher States

As implied in eq. (2.13), if the intermediate state n is a higher excited state z in the nucleus, then one must add terms of the form

$$P^{(12)}_{izf} = B(\theta,\xi_{iz},\xi_{zf}) \langle J_i||M(E\lambda)||J_f\rangle \langle J_i||M(E\lambda')||J_z\rangle \times \langle J_z||M(E\lambda'')||J_f\rangle \qquad (2.25)$$

to the excitation probability in eq. (2.24). The probability of multiple excitation becomes particularly large when bombarding with heavy ions.

In reorientation experiments the interference from higher states must be taken into account because their contribution to the total excitation probability of state f is of the same order of magnitude as that from the reorientation effect. It has been found (St67) that if the quadrupole moment of the first 2^+ state is being measured, then interference from the higher 2^+ states is the most important, however ideally all other states should also be considered.

Although the magnitudes of the matrix elements in eq. (2.25) are often known from other experiments, most experiments measure the

square of a matrix element and its sign is unknown. This means that the sign of the matrix product in eq. (2.25) is not usually known and this gives rise to an ambiguity in the measured value of Q_{J^π} depending on whether the interference is constructive (the excitation probability is increased) or destructive (the excitation probability is decreased) and for this reason, two values of Q_{J^π} are usually quoted. The sign of the interference is most conveniently described in terms of the quantity (Ku69)

$$P_4 = M_{if}M_{iz}M_{fz}M_{ff} \Big/ |M_{if}M_{iz}M_{fz}M_{ff}| \qquad (2.26)$$

where M_{if} represents the reduced matrix element $\langle J_i||M(E\lambda)||J_f\rangle$. This quantity has the advantage of being independent of the phase chosen for the matrix elements.

Although it is difficult to measure P_4 experimentally, a number of techniques have been used to determine the sign of the interference for ^{102}Ru(Fa76), ^{106,108,110}Pd (Be70,Ha76), ^{114}Cd(La72), ^{186,188}Os (Ba76), and ^{194}Pt (Ba76). When considering the first 2^+ state it was found, for interference from the second 2^+ state (i.e. the $2^{+'}$ state), that $P_4 = -1$ for all these cases except ^{194}Pt. A value $P_4 = -1$ means that the interference is constructive when $Q_{2+} < 0$ and destructive when $Q_{2+} > 0$. Kumar (Ku69) has made theoretical calculations based on the pairing-plus-quadrupole model and predicts P_4 to be negative for all isotopes of W, Os, and Pt except ^{192}Pt. Considering the two limits of collective motion, Kumar has shown that in the vibrational limit $P_4 = -1$, and that in the rotational limit $P_4 = -1$ if the $2^{+'}$ state belongs to a γ-band ($K = 2$) and $P_4 = +1$ if the $2^{+'}$ state belongs to a β-band ($K=0$). The result for ^{194}Pt remains a problem as the implication that the $2^{+'}$ state belongs

to a β-band is not consistent with the spectroscopy of ^{194}Pt (Ba76).

2.2.5 Interference from the Giant Dipole Resonance

In addition to the interference from intermediate states with relatively low excitation energies, it has been found (Ei64) that virtual excitation of a final state f via the 1^- states of the giant dipole resonance (GDR) can have a significant effect on reorientation measurement. (The probability of actually populating these 1^- states is, however, vanishingly small because of their high excitation energy.) In perturbation theory, the interference term has a form similar to that of eq. (2.25), i.e.

$$P_{if}^{(12)} = \langle J_i||M(E\lambda)||J_f\rangle \sum_n D(\theta,\xi_{in},\xi_{nf}) \langle J_i||M(E\lambda')||J_n\rangle \langle J_n||M(E\lambda'')||J_f\rangle \tag{2.27}$$

where n refers to the states in the GDR.

For a 2^+ final state, $\lambda' = \lambda'' = 1$ and if we make the assumption $|\langle J_i||M(E1)||J_n\rangle| = |\langle J_n||M(E1)||J_f\rangle|$ then $P_{if}^{(12)}$ becomes proportional to the minus-two moment of the photoabsorption cross section,

$$\sigma_{-2} = \int \frac{\sigma(E)}{E^2}\,dE = \frac{16\pi^3}{9\hbar c} \sum_n \frac{|\langle J_i||M(E1)||J_n\rangle|^2}{E_n - E_i} \tag{2.28}$$

which can be experimentally determined. From photoabsorption measurements it has been found (Le57) that

$$\sigma_{-2} = 3.5\ k\ A^{5/3}\ \mu b/MeV \tag{2.29}$$

where $k \approx 1$ for most nuclei with $A \geq 20$.

Classically, the dipole interaction between the projectile and the target nucleus may be interpreted as a dipole polarization of the nucleus. For a deformed nucleus the interaction energy V_{pol} between

the projectile and the induced dipole moment of the target nucleus is found to be proportional to σ_{-2} (de Bo68, Hä74). The effect of the GDR can thus be included by adding V_{pol} to the Hamiltonian $H_{int}(t)$, and this correction can be conveniently incorporated into the de Boer-Winther computer program discussed in section 2.3.

For final states other than 2^+ (and 0^+), $\lambda'' \neq 1$ and therefore $P_{if}^{(12)}$ in eq. (2.27) is not proportional to σ_{-2}. The effect of the GDR may be calculated by treating the GDR as a single intermediate state. In many cases the values of all the reduced matrix elements in eq. (2.27) are not known and some must be estimated.

2.2.6 Quantal Corrections

The quantum mechanically correct form of eq. (2.24) may be written as

$$P_{if} = F(\theta,\xi,\eta)\ B(E\lambda;\ i\rightarrow f)\ \ [1 + \rho(\theta,\xi,\eta)Q_{J\pi}] \qquad (2.30)$$

where η is defined in eq. (2.4) and $\eta = \infty$ in the semiclassical approximation. For reorientation experiments, the semiclassical treatment gives sufficiently accurate (i.e. to better than 1%) excitation probabilities if $\eta \gtrsim 50$ but for smaller values a quantal correction must be applied.

It may be shown (Al69) that the quantal correction to the excitation amplitude is of the order of $1/\eta$; this means that the correction to $F(\theta,\xi,\infty)$ will be of order $1/\eta^2$ and that to $\rho(\theta,\xi,\infty)$ of order $1/\eta$. The quantal corrections can be conveniently applied by using the relations (Al69, Ha74),

$$\frac{F(\theta,\xi,\eta)}{F(\theta,\xi,\infty)} = 1 + \left(\frac{\eta_0}{\eta}\right)^2 \left[\frac{F(\theta,\xi,\eta_0)}{F(\theta,\xi,\infty)} - 1 \right] \qquad (2.31)$$

and

$$\frac{\rho(\theta,\xi,\eta)}{\rho(\theta,\xi,\infty)} = 1 + \frac{\eta_0}{\eta} \left[\frac{\rho(\theta,\xi,\eta_0)}{\rho(\theta,\xi,\infty)} - 1 \right] . \qquad (2.32)$$

These equations imply that it is only necessary to calculate the functions $F(\theta,\xi,\eta)$ and $\rho(\theta,\xi,\eta)$ for one value $\eta = \eta_0$ and results for other values of η can be extrapolated. Values of these functions for $\eta = 4$, 8 and ∞ have been tabulated by Alder et al. (Al72) for E2 excitation but regretably not for E3.

Typical quantal corrections applied in the case of ^{204,206}Pb are listed in table 2.1. It can be seen that although the quantal correction to $F(\theta,\xi,\infty)$ is small ($\leq 0.2\%$), that to $\rho(\theta,\xi,\infty)$ is as large as 17%. However, as will be pointed out in chapter 3 the value of Q_{2+} is, in the present experiment, proportional to the difference in ρ for different projectiles; using $\rho_{^4He} = 0.04$ and $\rho_{^{16}O} = 0.16$ (see figs. 5.6 and 5.7), the quantal correction to the value $|\rho_{^{16}O} - \rho_{^4He}|$ is 0.3%. Quantal corrections are therefore expected to have a small effect on Q_{2+} in the present work (see subsection 5.4.2).

Table 2.1 Typical values of quantal corrections applied in the case of ^{204,206}Pb ($\theta = 171.6^{\circ}$)

Projectile	η	$F(\theta,\xi,\eta)/F(\theta,\xi,\infty)$	$\rho(\theta,\xi,\eta)/\rho(\theta,\xi,\infty)$
15 MeV ^{4}He	13.4	0.9980	1.17
46 MeV ^{12}C	39.8	0.9998	1.06
60 MeV ^{16}O	53.6	0.9999	1.04

2.2.7 Corrections to the Rutherford Orbit

A number of processes can give rise to small changes in the Rutherford orbit. If it is assumed that the main effect of these deviations is associated with a change in the distance of closest approach, then the effect can be simulated by a small change in the bombarding energy, i.e.

$$E_{eff} = E + \delta E \tag{2.33}$$

where δE is the correction applied to the bombarding energy E (in the laboratory frame of reference). Calculated values of δE for the various effects are listed in Table 2.2.

a) Electron screening

The atomic electrons around the target nucleus have the effect of screening the repulsive potential of the nucleus. The distance of closest approach is therefore decreased and an expression for the effective increase in bombarding energy has been given by Saladin et al. (Sa69),

$$\delta E = + Z_1 \, (32.65 \, Z_2^{7/5} - 40 \, Z_2^{2/5}) \, (1 + A_1/A_2) \text{ eV} . \tag{2.34}$$

b) Vacuum polarization

In quantum electrodynamics an interesting phenomenon is the virtual polarization of the vacuum arising from the existence of the electron-positron field. An important consequence of vacuum polarization is the increase in the electrostatic interaction between two charges. At separations between the charges of the order of 10^{-15} m, the correction to the Coulomb law is of the order of 0.5%,

and increases logarithmically at smaller separations (Fo54). A manifestation of vacuum polarization is its contribution to the energy difference between the $2p_{\frac{1}{2}}$ and $2s_{\frac{1}{2}}$ atomic levels in hydrogen (the Lamb shift). In the present work, vacuum polarization is accounted for by using an effective bombarding energy obtained by adding to the actual bombarding energy the correction (A175),

$$\delta E = - 1.55\ E\ \sin(\theta/2)\ \ln\left[\frac{134.5\ E\ \mathrm{Sin}(\theta/2)}{Z_1 Z_2 (1+A_1/A_2)(1+\mathrm{Sin}(\theta/2))}\right] \mathrm{keV} \quad (2.35)$$

where θ is the scattering angle in the centre of mass system. (Note that δE is in the laboratory system.)

c) Relativistic Effects.

Relativistic effects associated with charges in the Rutherford orbit can be estimated by the correction (A175),

$$\delta E = - 0.54\ \frac{E^2}{A_1(1+A_1/A_2)} \cdot \frac{1-\mathrm{Sin}(\theta/2)}{1+\mathrm{Sin}(\theta/2)}\ [1 + 2\ \mathrm{Sin}\ (\theta/2)]\ \mathrm{kev} \quad (2.36)$$

to the bombarding energy. As can be seen from Table 2.2, relativistic corrections are negligible in the present work.

Table 2.2 Corrections δE(keV) applied to the bombarding energy to account for electron screening, vacuum polarization, and relativistic effects (laboratory angle of 171.6°). The percentage change in the excitation probability P_{J^π} of $^{204,206}Pb$ (E2 excitation) and of ^{208}Pb (E3 excitation) due to these corrections is also listed.

Projectile	Electron Screening	Vacuum Polarization	Relativistic Effects	Total Corrections	$^{204,206}Pb$ ΔP_{2+}	^{208}Pb ΔP_{3-}
15 MeV ^4He	31	- 42	- 0.1	- 11	- 0.38%	- 1.12%
46 MeV ^{12}C	98	-126	- 0.3	- 28	- 0.32%	-
60 MeV ^{16}O	133	-161	- 0.4	- 28	- 0.25%	- 0.69%

2.3 Computer Calculations

As mentioned previously, when bombarding with heavy ions, interference due to excitation via higher states becomes important. In general, it is difficult to account for these using perturbation

theory and it is more convenient to use the multiple Coulomb excitation program of de Boer and Winther (Wi66).

The nuclear wave function $|\psi(t)\rangle$ satisfies the Schrödinger equation

$$i\hbar \frac{\partial}{\partial t} |\psi(t)\rangle = [H_o + H_{int}(t)] \; |\psi(t)\rangle \qquad (2.37)$$

where H_o is the Hamiltonian of the free nucleus. If the eigenstates $|r\rangle$ of H_o are defined by $H_o|r\rangle = E_r|r\rangle$, the nuclear wave function $|\psi(t)\rangle$ can be expanded in terms of these, i.e.

$$|\psi(t)\rangle = \Sigma \, b_r(t)|r\rangle \; \exp(i E_r t/\hbar) \qquad (2.38)$$

where $b_r(t)$ are time-dependent amplitudes. From these definitions, it can be seen that the Schrödinger equation is equivalent to the following set of coupled linear differential equations

$$i\hbar \, \dot{b}_r(t) = \sum_s \langle r|H_{int}(t)|s\rangle \; \exp[i(E_r - E_s)t/\hbar] \; b_s(t) \; . \qquad (2.39)$$

The program performs a numerical integration with respect to t in order to obtain the final excitation amplitudes. It must be noted that the values obtained from the program are still semiclassical (i.e. they assume a semiclassical trajectory) and corrections for quantal effects must be applied.

The accuracy to which the integration is performed is specified by the accuracy control parameter a_c (Wi66). At the end of each integration step, an estimate of the truncation error F (defined in Wi66) is made; if $F > a_c$ the step width is halved, and if $F < a_c/50$ the step width is doubled. Parameter a_c also controls the range of integration; small values of a_c increase the range.

The accuracy of the computed excitation probabilities P_{comp} was tested by decreasing a_c in powers of 10 until the results obtained converged to the same value of P_{comp} to within 0.1%. For values down to $P_{comp} \approx 10^{-3}$ this requirement was easily satisfied by setting $a_c \leq 10^{-6}$. However, for smaller values $P_{comp} \approx 10^{-5}$ (such small excitation probabilities were encountered for the 3^- state in ^{208}Pb, when bombarding with 15 MeV ^4He ions) it was found that setting $a_c \leq 10^{-8}$ was no longer adequate and computed values fluctuated within 1% of a mean value. While the cause for these fluctuations is not entirely clear, they may be explained by the following:

a) The expression used to calculate the truncation error may be an underestimate when small excitation amplitudes are involved, so that the resulting step widths are too large.

b) When very small values of a_c are used, the range of integration is unnecesarily increased and the larger number of integration steps may give rise to a bigger truncation error.

It was therefore decided to modify the program such that $F' = 14\,F$ was taken as the estimate of the truncation error. This had the effect of forcing the integration to proceed by smaller steps without increasing the integration range. The integration steps were further kept small by requiring that $F' < a_c/200$ before the width was doubled. Although computation time was approximately doubled these modifications ensured that (for $a_c \leq 10^{-8}$) the values obtained for P_{comp} were accurate to better than 10^{-8}, i.e. 0.1% of $P = 10^{-5}$.

The use of this Coulomb excitation program in the data analysis will be described in chapter 5.

CHAPTER 3

EXPERIMENTAL TECHNIQUE IN REORIENTATION MEASUREMENTS

In this chapter, the experimental methods which have been used to measure electric quadrupole moments using the reorientation effect in Coulomb excitation are briefly described, and the relative merits of each method are discussed. The experimental procedure employed in the present work is described in detail in section 3.2. The presence of certain contaminants in the targets could severely affect the data; section 3.3 describes the measures taken to reduce target contamination, and the tests performed on the targets to derive upper limits for these contaminants. Finally, because the excitation probabilities are very sensitive to the bombarding energy (see table 3.5) it was necessary to perform an energy calibration for the two accelerators used in the present experiment (see section 3.4).

3.1 Experimental Techniques used in Reorientation Measurements

In recent years, a number of different experimental techniques have been used to determine the electric quadrupole moment of the first excited states of nuclei by means of reorientation effect (Ch72, Kl75). In principle, measurement of the excitation probability and knowledge of the $B(E\lambda)$ (e.g. from lifetime measurements) should be sufficient (see eq. (2.24)). However, the small effect of the quadrupole moment on the total excitation probability (for ^{16}O projectiles it is 16% per barn for $^{204,206}Pb$, and 20% per barn for ^{208}Pb) means that the $B(E\lambda)$ must be known to a greater accuracy than is normally available from previous work. For this reason, it is usual to measure excitation probabilities P_α and P_β for different bombarding conditions so as to vary the size of the

reorientation effect. This procedure yields two or more equations (identical to eq. (2.24)),

$$P_\alpha = F_\alpha B(E\lambda) [1 + \rho_\alpha Q_{J\pi}] \quad (3.1a)$$

$$P_\beta = F_\beta B(E\lambda) [1 + \rho_\beta Q_{J\pi}] \quad (3.1b)$$

where the functions F and ρ may be evaluated from perturbation theory or with the de Boer-Winther program. If absolute values of P_α and P_β are measured, then equations (3.1a) and (3.1b) may be solved simultaneously to obtain $B(E\lambda)$ and $Q_{J\pi}$. If only relative values are measured, then

$$P_\alpha/P_\beta \approx F_\alpha/F_\beta[1 + (\rho_\alpha - \rho_\beta)Q_{J\pi}] \quad (3.2)$$

and only $Q_{J\pi}$ can be determined. In both cases, the sensitivity of the experiment to the quadrupole moment depends on the quantity $|\rho_\alpha - \rho_\beta|$ which may be maximised by appropriate choices of the parameters A_1, θ, and ξ (see eq. (2.23)).

a) Dependence of the reorientation effect on bombarding energy.

As can be seen from fig. 2.2, the function $K(\theta,\xi)$ (in eq. (2.23)) is only weakly dependent on ξ. This means that in experiments which vary the bombarding energy (and hence ξ) the variation in the excitation probability P is relatively insensitive to $Q_{J\pi}$. In addition, the need to perform experiments at safe energies and yet still obtain reasonable count rates places a severe restriction on the range of bombarding energies that may be used. This type of experiment is therefore rarely performed.

b) Dependence of the reorientation effect on scattering angle.

Varying the scattering angle θ can produce large changes in the value of $K(\theta,\xi)$ (see fig. 2.2) and therefore $|\rho_\alpha - \rho_\beta|$ can be

made large, particularly if heavy ions are used. Since the data may be collected at several angles simultaneously, this method makes economical use of accelerator time. However, at forward angles the differential cross section changes rapidly with θ (see for example Bi65, fig. 2.5). Extreme precautions must therefore be taken to define the scattering angle precisely(to of the order of 0.1^{o}).

c) Dependence of the reorientation effect on projectile mass.

Bombarding with projectiles of different mass can produce large changes in ρ. The requirement to operate at safe bombarding energies with each projectile results in similar values of ξ; the value of the function $K(\theta,\xi)$ is then almost constant and therefore $|\rho_\alpha - \rho_\beta|$ is roughly proportional to the difference in mass of the projectiles. Typical projectiles that have been used are ^{4}He, ^{12}C, ^{16}O, and ^{32}S, because the excitation energy of their first excited state is sufficiently high that the excitation probability is low compared to that of the target nucleus and the respective inelastic peaks are well separated in the spectrum. It is advantageous to detect the scattered projectiles near 180^{o}, not only because $K(\theta,\xi)$ attains a maximum, but because then the functions $F(\theta,\xi)$ and $K(\theta,\xi)$ vary only slowly with angle and θ does not have to be precisely defined.

3.1.1 Measurements Involving Gamma Rays

a) Gamma-Ray Singles Experiments.

This method has been fully described by Steadman et al. (St70) and consists of measuring the intensities of gamma rays detected in singles from a thick natural target bombarded with different

projectiles. From the relative intensities I_α/I_β, the relative contribution of the reorientation effect in each isotope can be determined and the difference in the quadrupole moments between the isotopes is obtained,

$$I_\alpha/I_\beta = I_\alpha(Q_\alpha = 0)/I_\beta(Q_\beta = 0)\,[1 + \bar{\rho}_\alpha Q_\alpha - \bar{\rho}_\beta Q_\beta] \qquad (3.3)$$

where

$$\bar{\rho} = (A_1/Z_2)\ \Delta E\ \overline{K(\theta,\xi)}/(1 + A_1/A_2) \qquad (3.4)$$

and $\overline{K(\theta,\xi)}$ is the function $K(\theta,\xi)$ averaged over θ and ξ. If the value of Q_{J^π} for one isotope is known (from other measurements) then one may obtain Q_{J^π} for the others. This technique is experimentally simple and since the cross section integrated over a large number of angles is measured (by placing the Ge(Li) detector close to the target) high count rates are obtained. One must, however, make a correction for the variation of the detection efficiency with gamma-ray energy. Frequently, a major difficulty in this type of experiment is the extraction of accurate intensities from complex singles gamma-ray spectra.

Of particular relevance to the present work is the use of this technique by Barnett et al. (Ba72) to measure Q_{3^-} for the 3^- state in ^{208}Pb. The value obtained depended on an assumed value for the quadrupole moment Q_{2^+} of the first 2^+ state in ^{206}Pb.

b) Particle-gamma ray coincidence experiments.

In this method, coincidences between inelastically scattered particles (detected in a surface barrier detector) and deexcitation gamma rays are observed, and the excitation probability is obtained from the coincidence yield I_{coinc} and the singles yield $(I_{el} + I_{inel})$ in the surface barrier detector. In this type of experiment one

must take into account the efficiency of the gamma-ray detector, the gamma-ray angular distribution, and dead time losses in the coincidence electronics and in the analog to digital converters (ADC's).

The gamma-ray angular distribution is attenuated when the highly ionised atoms recoil in vacuum; any unpaired atomic electrons will produce randomly oriented magnetic fields which interact with the magnetic dipole moment of the nucleus causing a precession of the nuclear spin axis. For this reason, one must measure the gamma-ray angular distribution to determine the hyperfine attenuation coefficients. The dependence on the attenuation coefficients can be eliminated by using thick targets (or thick target backings) so that the nuclei no longer recoil in vacuum.

With this technique, $Q_{J\pi}$ can be determined by using different projectiles or by detecting particles at different angles; in some experiments, B(Eλ) values have also been obtained. This latter method has been used by Olin et al. (Ol74) to measure the quadrupole moment of the first 2^+ state in ^{204}Pb.

c) Reorientation precession method

This method differs from those described in parts a) and b) in that it does not measure excitation probabilities but determines $Q_{J\pi}$ from its effect on the gamma ray angular distribution, i.e. on the magnetic substate populations (see section 2.1f) of the excited state. Two experimental arrangements to measure this effect have been suggested by de Boer and Eichler (de Bo68) and these have been applied in experiments performed by Grodzins et al. (Gr73) and by Hasselgren et al. (Ha76). The basic principle of the method is to measure gamma-ray yields at two angles in coincidence with scattered

projectiles detected (in a surface barrier detector) at a fixed angle. The quadrupole moment is then obtained from the ratio of the two yields.

This type of measurement is difficult because the effect of Q_{J^π} on the angular distribution pattern is small. Quantal corrections are also more important than in experiments that measure excitation probabilities. On the other hand, the value of Q_{J^π} obtained is less sensitive to multiple excitations through higher excited states; such experiments are also distinguished by their ability to determine the sign of the interference from higher states (see subsection 2.2.4).

3.1.2 Particle Spectroscopy

The most direct determination of the inelastic cross section is the detection of the scattered particles using high resolution particle spectrometry; the excitation probabilities are obtained directly from the intensity ratio $I_{inel}/(I_{el} + I_{inel})$. The major requirement is the ability to separate the elastic and inelastic groups, and for this reason the targets must be made thin ($\lesssim$ 20 $\mu g/cm^2$ for ^{16}O ions). The elastic peak is always much larger than the inelastic peak and the low energy tail on the elastic peak can considerably affect the extraction of the inelastic peak areas. If the tail height is reduced, then so is the uncertainty in the inelastic peak area; it is therefore very important to minimise the tailing on the peaks.

a) Magnetic spectrographs

Excellent particle energy resolution can be obtained with the new generation of magnetic spectrographs of the split-pole and QD^3 type (Sp67, Mi70). These spectrographs can compensate for kinematic

broadening, which is particularly a problem for heavy ions. This makes it possible to use solid angles up to 7 msr for the split-pole and 14 msr for the QD^3. The energy resolution is then limited primarily by energy loss and straggling in the target. Magnetic spectrographs do not suffer from the pulse height defect problems of surface barrier detectors (see subsection 3.2.3) with the consequent tailing on peaks, and for heavy ions the line shape obtained with a magnetic spectrograph should be better than that obtained with a surface barrier detector. Nevertheless, tailing can still occur due mainly to slit-edge scattering of the beam and of the projectiles scattered from the target. For magnetic spectrographs, there is the problem that the scattered ions leaving the target can be in different charge states and the elastic and inelastic peaks arising from each charge state must be summed to obtain the total elastic and inelastic particle yields.

b) Surface barrier detectors

When the excitation energy of the first excited state is high, the target thickness can be increased and this then determines the energy resolution; the inferior energy resolution of silicon surface barrier detectors is then less significant, and little advantage in energy resolution is gained by using a magnetic spectrograph. While, in general, surface barrier detectors are simpler and less expensive than magnetic spectrographs, many added benefits derive from the use of annular surface barrier detectors. Solid angles of the order of 40 msr can be obtained with an annular surface barrier detector and, in view of the small excitation probabilities involved in the present work, this is a major advantage

over the magnetic spectrograph. By using an annular detector near 180^{o} the amount of kinematic broadening is a minimum (see subsection 3.2.3) and, as mentioned before, the variation of $F(\theta,\xi)$ and $K(\theta,\xi)$ with θ is slow. The axial symmetry provided by an annular detector minimises the effect of changes in beam trajectory on the mean scattering angle. On the other hand, surface barrier detectors suffer from pulse height defect problems which give rise to tailing on peaks and these are particularly important when detecting heavy ions (see subsection 3.2.3). Tailing is also produced by slit edge scattering. It is therefore more difficult to obtain good lineshapes with surface barrier detectors than with magnetic spectrographs.

As before, values of $B(E\lambda)$ and $Q_{J\pi}$ can be obtained by varying the scattering angle or by using different projectiles. The latter is the basis for the present work and is described in detail in the next section.

3.2 Experimental Procedure

The experimental procedure consisted of bombarding thin isotopically enriched $PbCl_2$ targets with ^{4}He, ^{12}C and ^{16}O ions; a summary of bombarding energies at which data were collected for each isotope is given in Table 3.1. The scattered projectiles were detected with an annular surface barrier detector positioned at a mean laboratory scattering angle ψ_m of 171.6^{o}.

While the ^{204}Pb and ^{206}Pb experiments were similar, it was necessary to introduce certain changes in the ^{208}Pb experiment because of the higher excitation energy of the 3^{-} state and its

low excitation probability. These changes will be pointed out where appropriate.

The amount of tailing in the spectra was measured by the peak-to-valley ratio (P/V ratio) obtained by dividing the height of the inelastic peak by the minimum height of the background between the elastic and inelastic peaks.

Table 3.1 Bombarding energies at which data were collected.

Target Nucleus	Projectile	Bombarding Energy (MeV)
^{204}Pb	^{4}He	13.80, 14.45, 14.75, 15.30, 15.90, 16.30, 16.80, 17.50, 18.00, 18.50
	^{12}C	45, 46, 47, 48, 49, 50, 51, 52, 54, 56, 60
	^{16}O	59, 60, 61, 62, 63, 64, 65, 67, 70, 72, 75, 77, 78.5, 80, 85
^{206}Pb	^{4}He	13.80, 14.45, 14.75, 15.30, 15.90, 16.30, 16.80, 17.50, 18.00, 18.50
	^{12}C	44, 46, 48, 50, 52, 60
	^{16}O	60, 61, 62, 63, 64, 65, 67, 70, 72, 75, 77, 80, 85
^{208}Pb	^{4}He	15.1, 15.3
	^{16}O	59, 60, 61, 62, 63, 64

3.2.1 Accelerator Beams

The ^{16}O and ^{12}C beams were obtained from the ANU 14UD Pelletron accelerator (Op74) and the ^{4}He beams were obtained from an EN tandem accelerator. On both machines, an anti-scatter baffle was placed in front of the switching magnet to remove beam scattered from the walls of the analysing magnet box. On the EN accelerator it was found that beam degradation from slit edge scattering could be reduced by

maintaining the energy-defining slit in a highly polished condition. Beam quality was also improved by using thin stripper foils.

Beam dumps made of aluminium for the 14UD and carbon for the EN tandem were used to collect the beams. The use of materials of low atomic mass was necessary to ensure that particles backscattered from the dump and striking the detector had an energy sufficiently low not to interfere with the region of interest in the spectra. A carbon beam dump was not used on the 14UD because of a general policy of maintaining a clean, carbon-free vacuum for this accelerator.

3.2.2 Target Chamber Geometry

Experiments were performed in aluminium scattering chambers (Op75) with an inside diameter (ID) of 51 cm. The target chambers, and the experimental geometry, were similar on the two accelerators. The chamber on the 14UD was nickel plated as part of the clean vacuum policy for this accelerator. A schematic drawing of the experimental geometry is shown in fig. 3.1.

All collimators were made of tantalum and the edges were highly polished. Collimator C1, placed on a collimator mount CM, prevented the beam from striking the back of an annular detector AD. By employing special-order detectors with a large diameter hole, a 4.6 mm inside diameter could be used for C1 and this contributed to the reduction of slit edge scattering. A 3 mm thick tantalum absorber TA reduced the flux of X-rays (generated by the beam intercepted at C1) reaching the detector. Collimator C1 was electrically insulated so that by measuring the current, beam focussing could be monitored.

It was necessary to use electron suppression to prevent secondary electrons, emitted from target T, producing a large number of low energy pulses. Permanent bar magnets BM were placed on either

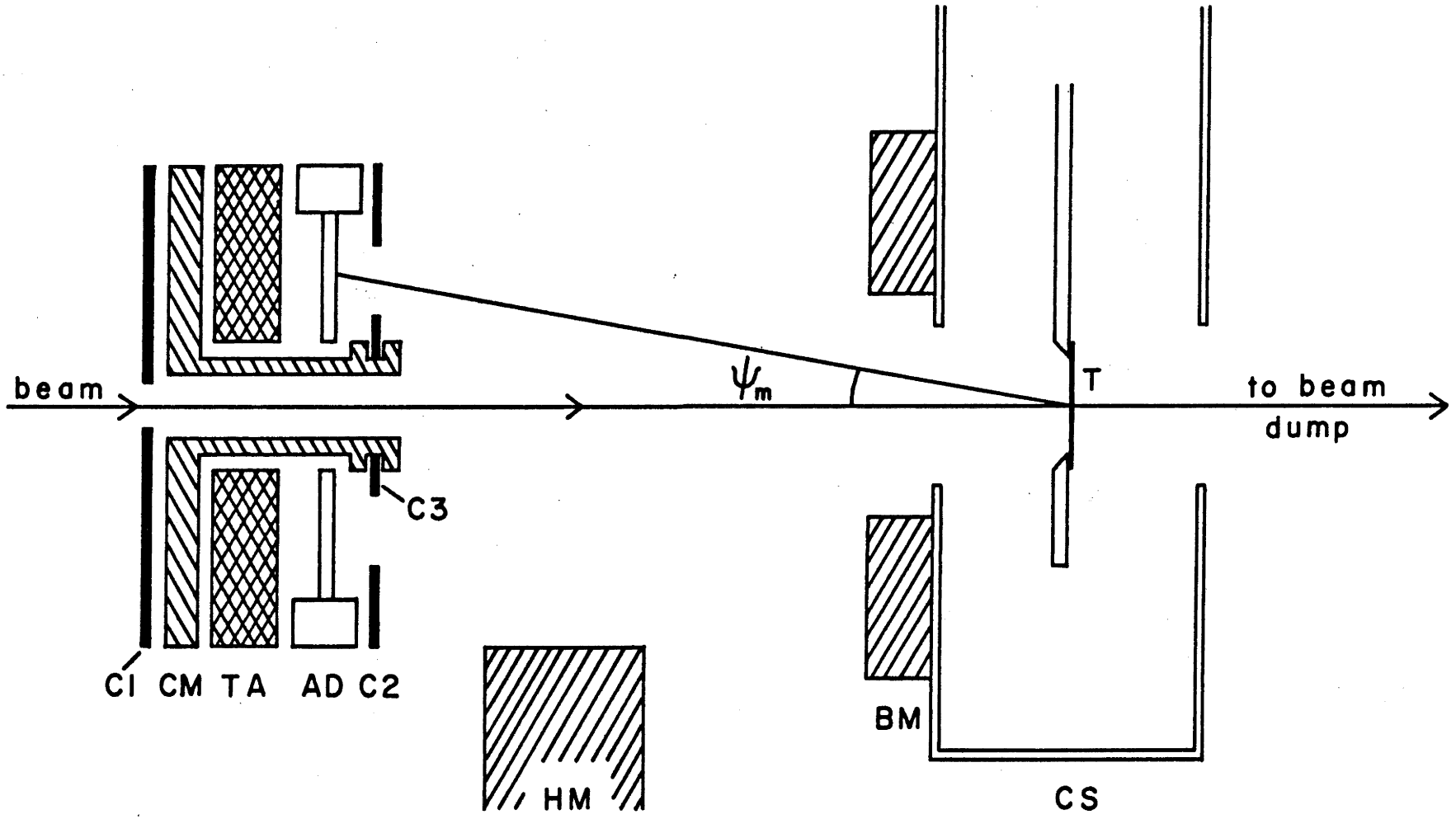

Fig. 3.1 Target chamber geometry. (Abbreviations are defined in the text.)

side in front of the detector, and a horseshoe magnet HM below. On the EN accelerator runs, the target was surrounded by a copper shroud CS cooled with liquid nitrogen to inhibit the deposition on the target of carbon and other impurities during bombardment.

Collimators C2 and C3, placed in front of the detector, prevented particles scattered from the target from reaching the detector edges. These collimators define the effective solid angle $d\Omega$ (about 42 msr) and the mean laboratory angle ψ_m (about 171.6^o) at which the particles were detected. The kinematic broadening is about 4 keV for ^4He, 30 keV for ^{12}C, and 44 kev for ^{16}O. It can be seen that the use of an annular detector gives a relatively large solid angle for an acceptable amount of kinematic broadening. Moreover, between the minimum and maximum scattering angles defined by collimators C2 and C3, the excitation probability for $^{204,206}Pb$ varies only by 0.13% for ^4He, 0.34% for ^{12}C, and 0.40% for ^{16}O. In the case of ^{208}Pb, the excitation probability varies by 0.41% for ^4He, and 1.08% for ^{16}O.

3.2.3 Annular Surface Barrier Detectors and Associated Electronics

Annular surface barrier detectors (supplied by Ortec Inc.) used in this series of experiments had an active area of 300 mm^2 and a sensitive thickness of about 200 μm (sufficient to completely stop ^4He particles up to 19 MeV and ^{16}O up to about 170 MeV). The electronics consisted of an Ortec 125 preamplifier and a Tennelec 203 BLR main amplifier. Evidence of pulse pile-up was particularly noticeable in the ^4He spectra and this problem was reduced by setting the amplifier time constant at 0.25 or 0.5 μs (although these short time constants would be expected to give slightly worse energy resolution).

Typical values for energy resolution, measured at the FWHM, were 35 keV for ^{4}He, 110 keV for ^{12}C and 145 keV for ^{16}O; the principal contributions being from detector resolution and from target thickness (see table 3.2).

When detecting heavy ions, several processes in the detector give rise to low energy tails. A heavy charged particle (e.g. ^{16}O as distinct from ^{4}He) has large specific energy losses and creates a dense cloud of electron-hole pairs along its path. The ionisation density is such as to create a region of reduced electric field inside this cloud; before the applied external electric field can disperse the cloud, significant recombination of charge carriers can take place. The statistical fluctuations in the resulting loss of pulse amplitude can cause tailing. The recombination of charge carriers can be decreased by increasing the applied electric field, and for this reason detectors with high collection fields $\gtrsim 10^{4}$ V/cm were employed in the present work. The situation could be further improved by cooling the detector and by over-biasing (although the electric field only varies as the square root of the applied voltage), but these measures were not found to be necessary.

Another important contribution to peak tailing arises from nuclear collision processes. Since the probability of a nuclear interaction increases with decreasing velocity of the charged particle, heavy ions lose a significant fraction of their energy by nuclear collision processes, in which the incident energy does not give rise to electron-hole creation. The statistical variations in this energy loss cause the tailing. These processes are a function of the detector material and cannot be avoided. An additional problem important for heavy ions is the decrease in energy resolution

caused by fluctuations of the energy loss in the dead layer in front of the detector.

Radiation damage by heavy ions can create electrically-active defects in the crystal lattice of the detector. These defects produce local variations in the electric field and affect the recombination rate of the charge carriers with peak tailing as a result. Because of the large number of spectra collected and the long running times (typically 24 hrs) associated with each, the detectors were subjected to large doses of heavy ions, and because of their limited life were replaced as necessary. Evidence of extensive radiation damage was increased tailing in the spectra and a marked increase in leakage current.

The ^{4}He spectra in the ^{208}Pb experiment, because of the low excitation probabilities involved, required very long running times (100 hrs), thicker targets (100 $\mu g/cm^2$) and larger beams (200 nA). With the resulting high count rate, pulse pile-up peaks were clearly observed and in order to improve the spectra, pile-up rejection circuitry was introduced. This system consisted principally of a pile-up gate which gives a logic output when two pulses from the preamp arrive within a specified time interval; the logic signal then closes a linear gate to reject these unwanted pulses. This system reduced the count rate of pulses into the pulse height analyser by 10%. Although the pile-up peaks themselves could not be removed, the tail extending on their low energy side (due to partial overlap of pulses) was considerably reduced and spectrum quality thereby improved.

3.2.4 Target Quality

In the present work, target quality was a crucial factor in obtaining adequate peak-to-valley ratios. The first targets made consisted of lead metal evaporated on a carbon backing. The enriched isotope, supplied in nitrate form, was first converted to the oxide by heating in air; when subsequently heated in vacuum the oxide was reduced to the metal which then evaporated onto carbon backings. The behaviour of these targets was found to be somewhat erratic. While a few gave reasonable P/V ratios (typically 20:1 for 15.2 MeV ^{4}He ions on ^{206}Pb) most gave very inferior results. Target quality was also found to vary from one spot to another on a given target. Visual inspection of these targets under a microscope showed that in addition to the uniform lead coating, the target was dotted with small lumps of material. Examination of "bad" targets showed many such lumps while "good" targets were almost devoid of them. These lumps were probably caused by spitting from the crucible during the evaporation, even though care was taken to heat the crucible slowly.

It was therefore decided to use lead chloride, $PbCl_2$, which is easy to prepare chemically from the nitrate form, and when heated appears to sublime. By progressively heating the crucible, the rate of evaporation could be easily controlled, and uniform targets reliably obtained. The targets could be subjected to ^{4}He beam currents up to 300 nA for long periods without any significant deterioration. When tested with an ^{16}O beam the targets were found to slowly evaporate, but it was possible to prevent this by evaporating a thin layer (1 - 2 $\mu g/cm^2$) of carbon onto the front surface of the target. A small portion was left uncovered so that the thickness of this layer could later be measured. The additional

carbon layer was also necessary for the relatively thick targets used in ^{4}He bombardment of ^{208}Pb. Target requirements for ^{12}C beams were similar to those for ^{16}O.

By optimising the focussing on the 14UD, it was possible to obtain beam spot sizes < 1 mm at the target; this produced a rapid deterioration of the target. This problem was overcome by deliberately defocussing the beam.

The target thickness employed in the present work are given in Table 3.2; as always, these values represent a compromise between count rates and spectrum quality.

Table 3.2 Typical target thicknesses

Isotope	Projectile	Thickness of $PbCl_2$	
		$\mu g/cm^2$	keV
^{204}Pb and ^{206}Pb	15 MeV ^{4}He	40 - 65	7 - 11
	46 MeV ^{12}C	22	31
	60 MeV ^{16}O	10 - 20	24 - 48
^{208}Pb	15 MeV ^{4}He	97 - 121	16 - 20
	60 MeV ^{16}O	18	43

3.3 Target Contaminants

With the present experimental technique, it is important that no significant contaminant peaks lie beneath the Pb elastic or inelastic peaks. Target contaminants can be categorised into

isotopic contaminants (i.e. other Pb isotopes) and those due to other elemental impurities (i.e. isotopes of the elements other than lead). Since highly enriched targets were used (see table 3.3), corrections for isotopic contaminants were small; these are treated in sections 4.3 and 4.4. Contaminant peaks which would be located underneath the elastic peak of a Pb isotope with mass A would arise from impurities in the mass ranges A ± 10 for ^{4}He, A ± 4 for ^{12}C, and A ± 3 for ^{16}O. Possible contaminants

Table 3.3 Percentage isotopic compositions of the lead targets used in the present work. Values quoted were those obtained from the suppliers (Oak Ridge Separated Isotopes Division)

Isotope	Target			
	204	206 A	206 B	208
204	99.73 ± .02	< 0.03	< 0.01	< 0.05
206	0.17 ± .01	98.39 ± .05	99.8 ± .02	0.17 ± 0.05
207	0.05 ± .01	0.82 ± .05	0.2 ± .02	0.69 ± 0.05
208	0.06 ± .01	0.77 ± .05	< 0.03	99.14 ± 0.10

Note:- In the ^{206}Pb experiment, target material A was used to obtain the ^{16}O data at 60, 61, 62, and 63 MeV. Target material B was used to obtain all other data.

which could give rise to elastic peaks unresolved from the Pb inelastic peaks are listed in table 3.4. Although relatively large amounts of contaminants (say up to 0.5% by weight) can be tolerated for the Pb elastic peak, the Pb inelastic cross-section is much lower than that of the elastic peak, and only much smaller quantities of contaminants can be tolerated; these will be discussed later in this section. In

Table 3.4 Mass ranges of possible contaminants that could give rise to elastic peaks unresolved from Pb inelastic peaks. Elements associated with these mass ranges are also listed.

Beam	Target		
	^{204}Pb	^{206}Pb	^{208}Pb
^{4}He	103 - 120 Ru,Rh,Pd,Ag,Cd,In,Sn	109 - 125 Pd,Ag,Cd,In,Sn,Sb,Te	58, 59 Ni,Co
^{12}C	180 - 191 Hf,Ta,W,Re,Os,Ir	183 - 195 W,Re,Os,Ir,Pt	-
^{16}O	188 - 198 Os,Ir,Pt,Au,Hg	191 - 201 Os,Ir,Pt,Au,Hg	175 - 180 Yb,Lu,Hf

order to ensure high target purity, a number of precautions were taken:

a) Ultra-high purity hydrochloric acid was used to convert the lead nitrate to lead chloride.

b) High purity glucose was used as a release agent for target backings. Glucose is composed of H, C, and O, all of which have a low mass. On the other hand, detergents contain elements with higher masses, and since they often consist of mixtures of chemicals, their chemical composition is not readily known.

c) Evaporator surfaces were sandblasted and washed in alcohol. A copper shroud, cooled with liquid nitrogen, was placed between the evaporator and the vacuum system.

d) The crucible was made of spectrographic-grade carbon and prior to the evaporation was heated to white heat to drive off most contaminants. Because of the relatively low melting point of $PbCl_2$ ($501^{\circ}C$) it was only necessary to heat the crucible to a dull red heat during the evaporation.

e) Since mercury has a mass similar to lead, the problem of

possible mercury contamination arising from the mercury diffusion pumps on the EN-accelerator target chamber was avoided by replacing these with oil diffusion pumps. In addition to cold traps placed in the vacuum system, a cold shroud surrounded the target.

f) The vacuum system on the 14UD is built largely of stainless steel, and is pumped by ion pumps; no problems of target contamination from the vacuum system have been experienced.

3.3.1 The ^{4}He Data

The technique used to investigate the possible presence of contaminants in the targets consisted of bombarding the targets with ^{4}He ions (8 - 10 MeV), detecting the ^{4}He particles scattered near 180°, and identifying the elastic peaks in the spectrum. In order to obtain reliable estimates of the possible amount of contaminants in the target, the bombarding energy was chosen to be below the maximum safe bombarding energy (defined in section 5.1) for the possible contaminants. For contaminants in the mass range A = 103 - 125 (see table 3.4) the maximum safe bombarding energy is about 10 MeV, while for A = 58, 59 it is about 8 MeV.

The carbon backings initially used with the targets were found to contain appreciable amounts of tin (1.4×10^{-2}%) and iodine (1.0×10^{-2}%). Attempts to remove these contaminants by using nominally higher purity carbon and by using an evaporator with all stainless steel surfaces (the evaporator normally used was partly made of brass), proved unsuccessful. Aluminium backings showed no such contaminants when tested, and an upper limit of 2.8×10^{-3}% by weight, at the two standard deviation level of the

background, can be placed on the possible amount of contaminants in the mass range A = 100 - 130. It was therefore decided to use aluminium backings for targets used to acquire the ^{4}He data in the $^{204,206}Pb$ experiments. (As will be discussed below, carbon backings were used in the ^{208}Pb experiment.)

Further investigation of the aluminium backings showed that they produced a significant amount of pulse pile-up due to ^{4}He being elastically scattered from ^{27}Al and ^{16}O in the backings. As can be seen from fig. 4.9, the peak of this pile-up occurs between the Pb elastic and 2^{+} inelastic peaks so that the 2^{+} peak sits on top of a pile-up background. Although in the region of the 2^{+} peak, the pile-up background is smooth and does not present serious problems in the analysis (see subsection 4.3.3), it will tend to reduce the peak-to-valley ratio. The aluminium backings were therefore made as thin as possible (20 - 30 $\mu g/cm^{2}$). Excitation functions were taken for ^{4}He elastic scattering from ^{27}Al and ^{16}O at bombarding energies between 13.5 MeV and 16.5 MeV. These excitation functions are shown in figs. 3.2 and 3.3 and are in good agreement with previous experiments (Ij64, Hu67, Iv69, Jo69, Ha73, OR72). With this information, it was possible to reduce the pile-up by collecting data at bombarding energies where the product of the ^{27}Al (^{4}He, ^{4}He) ^{27}Al and ^{16}O(^{4}He, ^{4}He) ^{16}O elastic cross-sections (fig. 3.4) was a minimum.

In addition to tests on the target backings, the complete $^{204,206}PbCl_{2}$ targets were also tested by bombarding with 10 MeV ^{4}He ions. At this bombarding energy, the elastic peaks from masses A = 100 - 130 are higher in energy relative to the Pb 2^{+} inelastic peak than at energies used for reorientation measurements. The spectra obtained are shown in figs. 3.5 and 3.6 for ^{204}Pb and ^{206}Pb

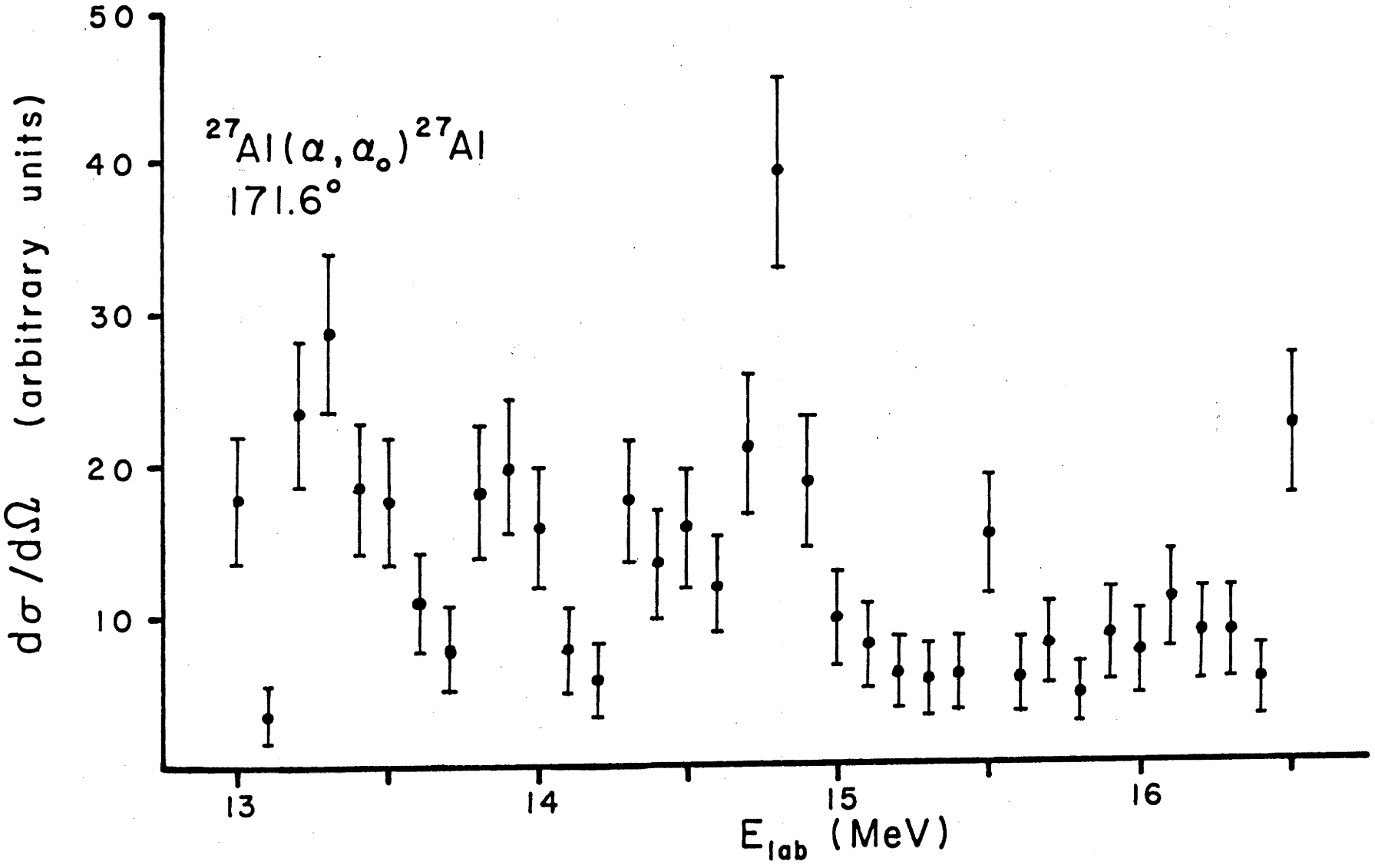

Fig. 3.2 Excitation function for the reaction $^{27}Al(\alpha,\alpha_0)^{27}Al$.

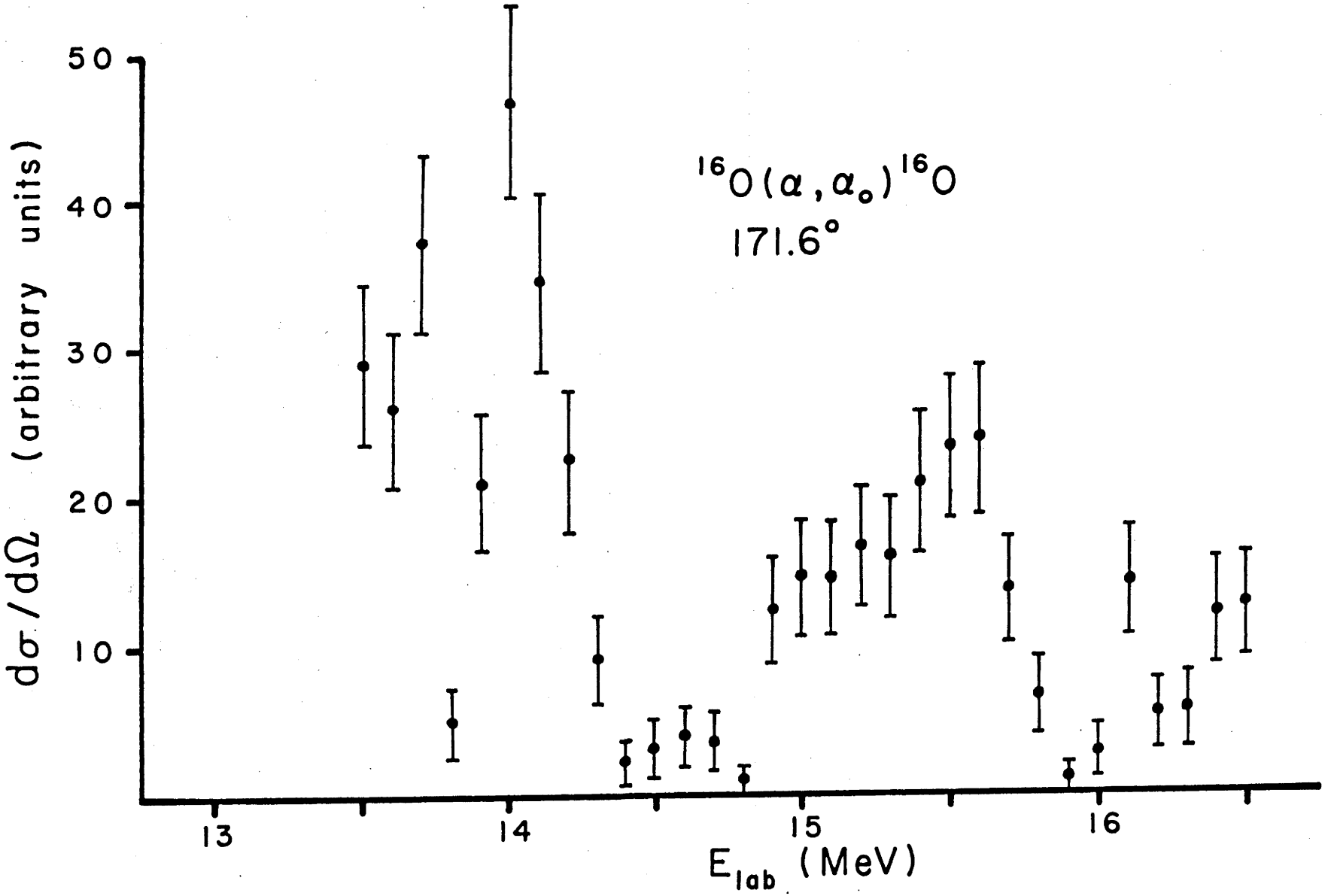

Fig. 3.3 Excitation function for the reaction $^{16}O(\alpha,\alpha_0)^{16}O$.

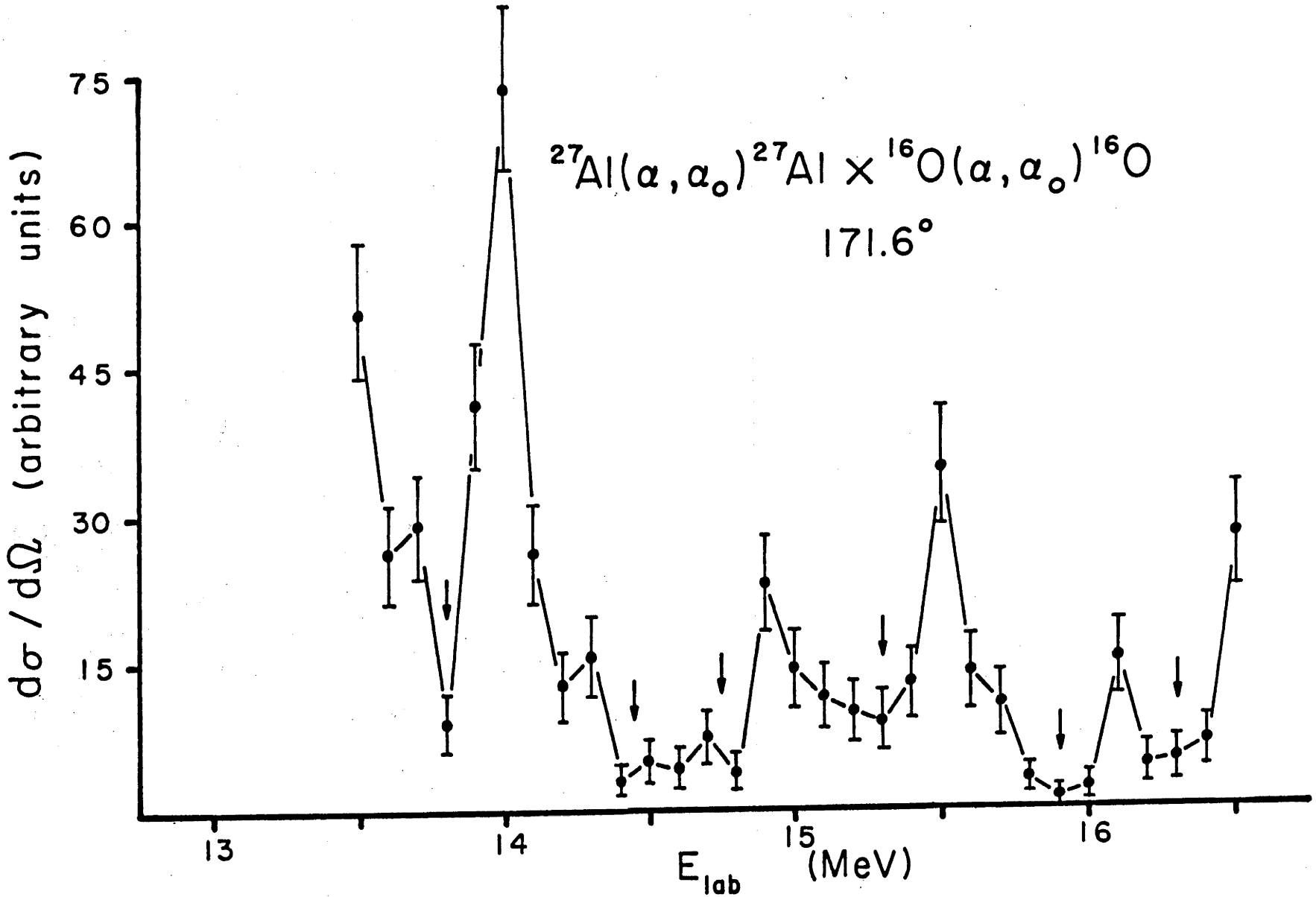

Fig. 3.4 Product of the $^{27}Al(\alpha,\alpha_0)^{27}Al$ and $^{16}O(\alpha,\alpha_0)^{16}O$ cross sections. Unlabelled arrows indicate energies at which Coulomb excitation data were obtained.

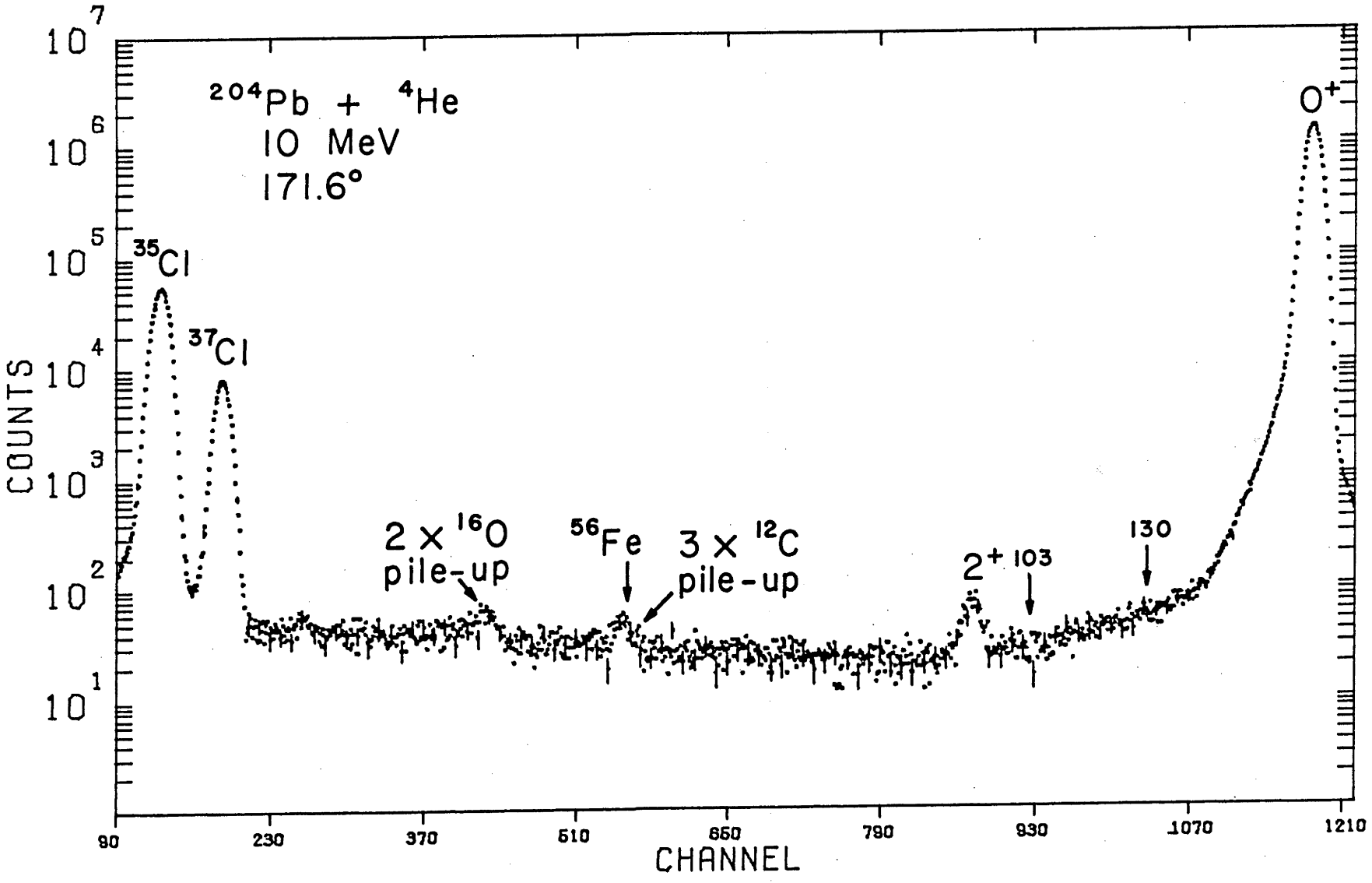

Fig. 3.5 Spectrum of 10 MeV ^{4}He projectiles backscattered from a $^{204}PbCl_2$ target.

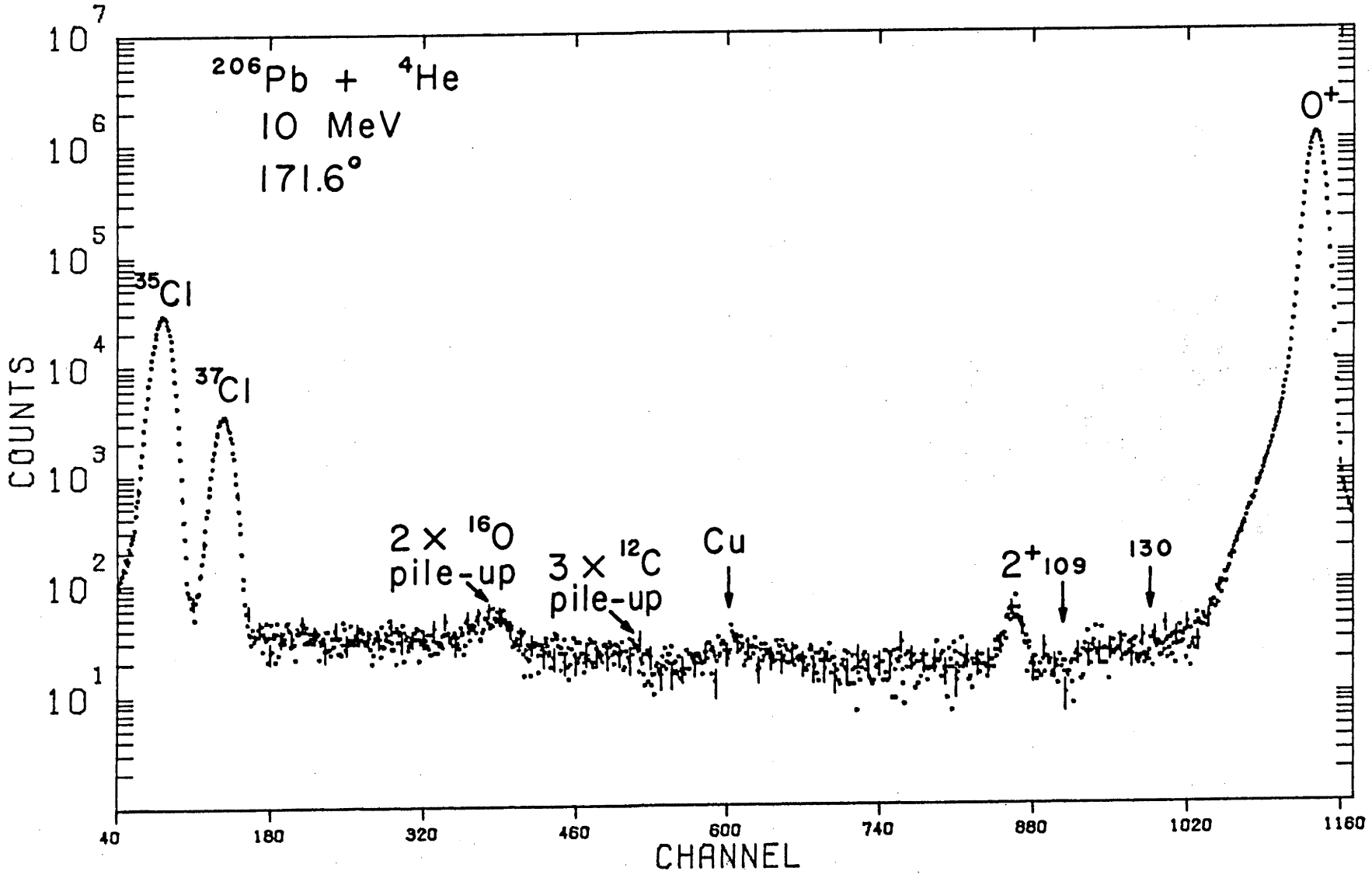

Fig. 3.6 Spectrum of 10 MeV ^4He projectiles backscattered from a $^{206}PbCl_2$ target.

respectively. At the level of two standard deviations of the background, upper limits of 5.3×10^{-4}% and 4.6×10^{-4}% by weight can be placed on the amount of A = 100 - 130 contaminants in the ^{204}Pb and ^{206}Pb targets respectively. If one assumes that the elastic scattering cross section for these contaminants in the energy range between 13.8 MeV and 15.3 MeV is equal to the Rutherford value, then it can be concluded that these contaminants could contribute at most 0.85% to the ^{204}Pb 2^+ peak at 13.8 MeV and 0.38% at 15.3 MeV. For ^{206}Pb, the maximum contribution of contaminants to the 2^+ peak is 0.95% at 13.8 MeV and 0.44% at 15.3 MeV. However, since the elastic scattering cross section for these contaminants is expected, at these energies, to be less than the Rutherford value, the above values can be regarded as absolute upper limits. In the case of the even-mass cadmium isotopes in the mass range A = 106 - 116, the elastic scattering cross section at 17.5 MeV is between 8.4% and 5.6% (respectively) of the Rutherford value (Sp77); for ^{114}Cd at 13.5 MeV it is 60% (Es76). No information is available on the elastic cross sections, at these energies, for other nuclei in the mass range A = 103 - 120.

In the ^{208}Pb experiment, only elastic peaks from ^{58}Ni and ^{59}Co could lie underneath the 3^- inelastic peak. Since no evidence of ^{58}Ni or ^{59}Co was observed in the carbon backings (an upper limit of 6×10^{-4}% can be placed at the two standard deviation level) and because of the need to obtain the best possible peak-to-valley ratios (in view of the very low excitation probabilities), carbon backings were chosen in preference to aluminium which gives rise to substantial pile-up. The targets were tested by bombarding with 8 MeV ^{4}He ions, and at the two standard deviation level an upper limit of 5.6×10^{-4}%

can be placed on the presence of ^{58}Ni or ^{59}Co in the target. Taking the elastic scattering cross section for ^{58}Ni and ^{59}Co at 15 MeV to be 15% (Se73) of the Rutherford value, the total contribution from these contaminants would be less than 3% of the 3^- peak area; this upper limit is tolerable in view of the uncertainties of 5 - 8% in extracting the 3^- peak areas (see subsection 4.4.2).

3.3.2 The ^{12}C and ^{16}O Data

It can be seen from table 3.4 that for the ^{12}C and ^{16}O data, the contaminants that would be located beneath the 2^+ peak in $^{204,206}Pb$ are within the mass range A = 180 - 201. Both tungsten and tantalum are included in this mass range and although these materials are often used for crucibles in target manufacture, in the present work a carbon crucible was used. Mercury contamination, which could affect the ^{16}O data, is not expected to be a problem since the targets were never exposed to a vacuum system employing mercury diffusion pumps. The only other contaminants which could affect the data are Pt, Au, and some rare earths; it is unlikely that any of these would be present in the targets in view of the precautions which were taken to ensure high target purity. (These precautions are discussed at the beginning of this section.)

A $^{208}PbCl_2$ target was tested with 120 MeV ^{32}S ions, and an upper limit of 9×10^{-3}%, at the two standard deviation level of the background, can be placed on the possible amount of contaminants in the mass range A = 180 - 196. Since all $PbCl_2$ targets were made in the same way (note that carbon backings were used), a similar upper limit on these contaminants can be placed for the ^{204}Pb and ^{206}Pb targets. Using the above upper limit, and assuming that the elastic

scattering cross section for these contaminants is equal to the Rutherford value, it is deduced that, for 60 MeV ^{16}O, the area of the 2^+ peak would be affected by at most 1.0% for ^{204}Pb and 1.4% for ^{206}Pb. (For 65 MeV ^{16}O, the effect of these contaminants is reduced by 33%.) In the case of 45 MeV ^{12}C, the 2^+ peak area would be affected by at most 1.5% for ^{204}Pb and 2.0% for ^{206}Pb. Since the elastic cross section is expected to be less than the Rutherford value, the above values can be regarded as absolute upper limits.

In the ^{208}Pb experiment, contaminants in the mass range $A = 175 - 180$ would lie underneath the 3^- peak. Of the elements with isotopes between $A = 175$ and $A = 180$, all except Hf and Lu have isotopes outside this range which would have been detected. An upper limit of 5×10^{-4}%, at the two standard deviation level, can be placed on the intensities of elastic peaks due to heavy contaminants with $A < 175$, or $180 < A < 186$. It is unlikely that the amount of contaminants with masses $A = 175 - 180$ is more than this, and consequently an upper limit of 3% can be placed on contributions of possible contaminants to the 3^- peak area.

3.4 Energy Calibration

Since Coulomb excitation probabilities are a strong function of the bombarding energy of the projectile, it is important, in reorientation experiments, to determine beam energies precisely. The effect of changes in the bombarding energy on the excitation probability is shown in table 3.5, which shows that beam energies must be known to better than 0.1%. The energy calibration of the EN tandem had been previously measured (Es76) for $^4He^{++}$ energies

up to ~ 15.93 MeV; during the course of this experiment the calibration was periodically checked as described below. The newly installed 14UD Pelletron accelerator was calibrated for the first time in the course of this work; the results are discussed in detail by Spear et al. (Sp76). In both cases, the energy calibration consisted of determining the magnet constant K, defined in the relativistic relationship (Ov69),

$$E = K B^2 (Z^2/M) \left[1 + \frac{E}{2Mc^2}\right]^{-1} \text{ MeV} \qquad (3.5)$$

where Z is the effective charge of the particle (in units of electronic charge), M is its mass (in nuclidic mass units), B is the magnetic field (in T), and $E/2Mc^2$ is half the ratio of kinetic energy to rest mass energy. The magnet constant K is in units of $MeV.u/T^2$.

Table 3.5 Percentage change in excitation probability for a 0.1% change in bombarding energy

Projectile	E_b (MeV)	Target Nucleus		
		^{204}Pb	^{206}Pb	^{208}Pb
^{4}He	15.3	0.55	0.52	1.56
^{12}C	46	0.54	0.51	-
^{16}O	60	0.56	0.52	1.47

3.4.1 Calibration of the 14UD Pelletron

The energy calibration of the analysing magnet on the 14UD Pelletron consisted of determining the magnet constant K at magnetic

fields of 0.43, 0.60, and 0.90T (the highest field used in the present reorientation experiments was 0.73 T for 56 MeV $^{12}C^{4+}$). As the differential hysteresis of the magnet could produce energy shifts of about 0.2% (Sp76) it was necessary to set the magnetic field by a known and reproducible method (i.e. to recycle the magnet) before making measurements. The usual procedure (for the EN tandem) of increasing the magnet current from zero to 200A three times in succession, and then approaching the desired field in the direction of increasing field, was found to be adequate. Before taking data, the energy defining slits were set with a narrow (0.76 mm) gap in the dispersive plane. Calibration points were taken in November 1975 and in July 1976; the ^{204,206}Pb data were taken within this period, and the ^{208}Pb data was taken in September 1976. Each calibration point made use of a different reaction (see table 3.6) and these are described below.

a) Calibration at B = 0.43 T.

The resonance in $^{12}C + p$ corresponding to the lowest T = 3/2 state in ^{13}N is at 14.23075 ± 0.00020 MeV (Hu73, Go75) and the two exit channels $^{12}C(p,p_0)^{12}C$ and $^{12}C(p,\alpha_0)^{4}B$ were studied. In the first case, the protons were detected at a mean laboratory angle of 172.6° in a 1000 μm thick annular detector; in the second reaction, a 40 μm surface barrier detector detected alpha-particles at a laboratory scattering angle of 40° where the resonance has an approximately Breit-Wigner shape (deMe73). Results obtained are shown in fig. 3.7 and fig. 3.8.

b) Calibration at B = 0.65 T.

The method here involved matching the energy of ^{4}He ions

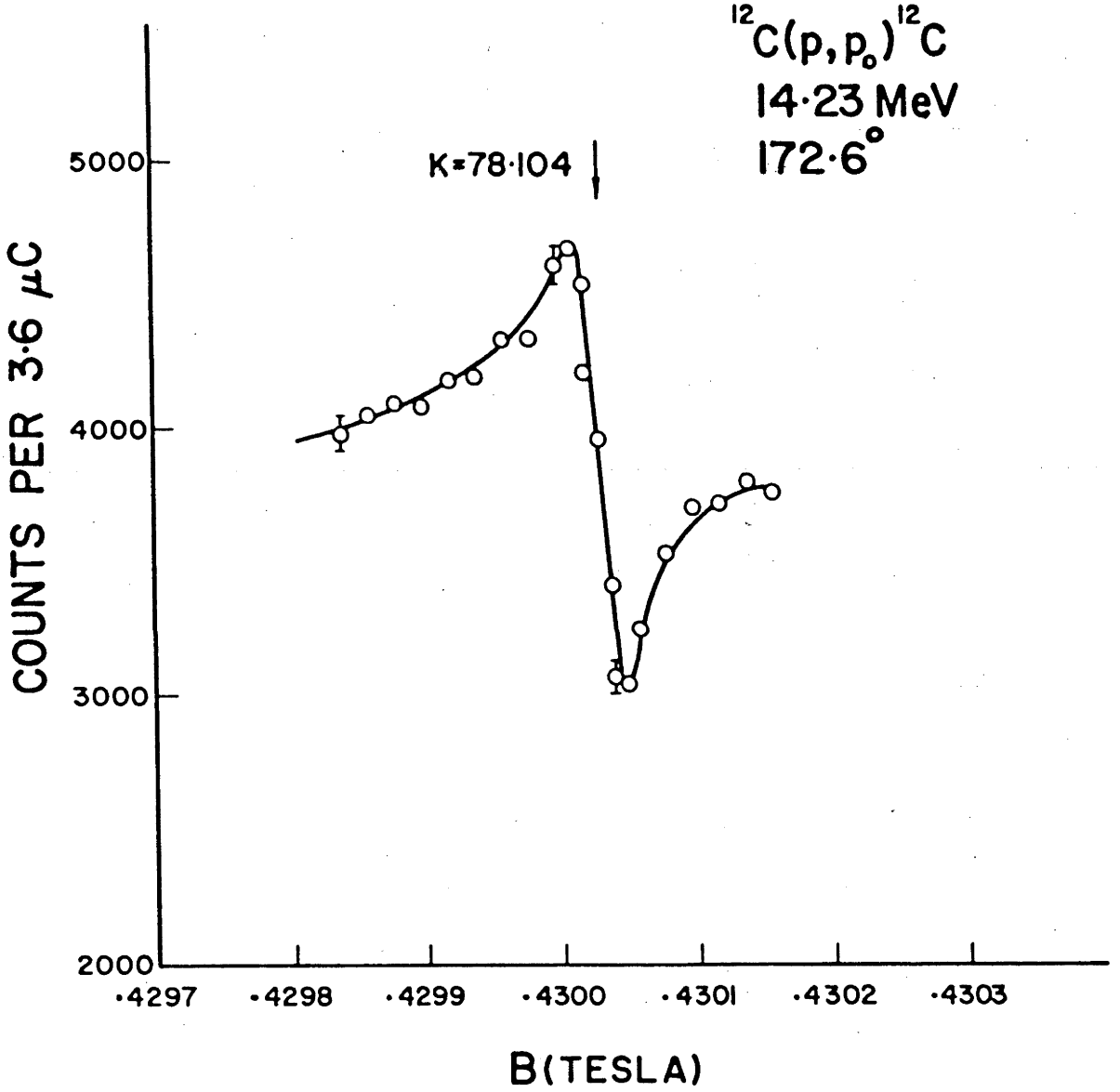

Fig. 3.7 Resonance in $^{12}C(p,p_0)$ ^{12}C at 14.231 MeV. The full curve is merely a guide to the eye. (Data were taken in November 1975.)

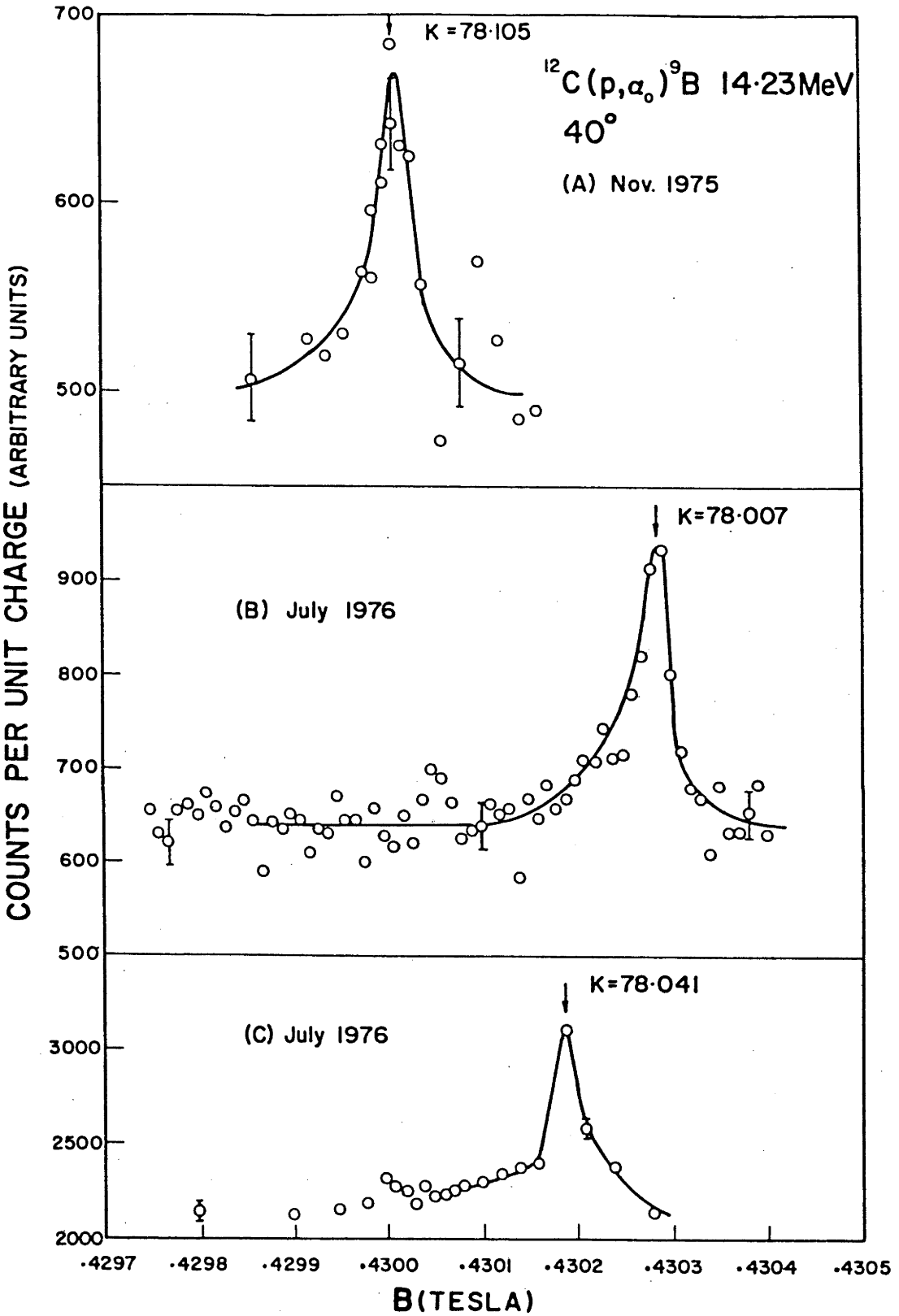

Fig. 3.8 Resonance in $^{12}C(p,\alpha_0)^{9}B$ at 14.231 MeV. The full curves are merely guides to the eye.

inelastically scattered from a thin carbon foil with the known energy of alpha-particles emitted from a thin ^{212}Pb ("radiothorium") radioactive source; this source emits alpha-particles with energies (Wa64) 8.7850 ± 0.0008 MeV (from Po^{212}), 6.0496 ± 0.0007 Mev ($Bi^{212}(\alpha_1)$), and 6.0889 ± 0.0007 MeV ($Bi^{212}(\alpha_0)$). The doublet could not be fully resolved, and from the intensity ratio $\alpha_0/\alpha_1 = 2.57 \pm 0.01$ (Ry51) the energy centroid is calculated to be 6.0606 ± 0.0007 MeV. For this calibration point, the $^4He^{++}$ bombarding energy was 32.86 MeV, so that after populating the 4.439 MeV state in ^{12}C, ^4He projectiles detected at 172.6^o in an annular counter had an energy near that of the doublet (see fig. 3.9). An advantage of this method is that since the ^4He ion energy is very close to the alpha-particle energy, any non-linearities in the detector and the electronics are negligible. Also, since the same type of particle is being detected in both cases, there is virtually no difference in pulse height defect when these are detected. Detection at backward angles also means that the scattering angle does not have to be known to a high accuracy and, because of the axial symmetry of the detector about the beam direction, movements of the beam spot on the target do not change the mean scattering angle. The method is therefore quick and simple. To take account of gain drifts in the electronics, a number of source spectra and scattered-particle spectra were taken alternatively. The beam intensity was kept small to avoid gain changes due to count rate effects and gains were monitored with a precision pulser. The energy dispersion was determined in the source spectra from the 2.7244 ± 0.0010 MeV energy separation of the two groups.

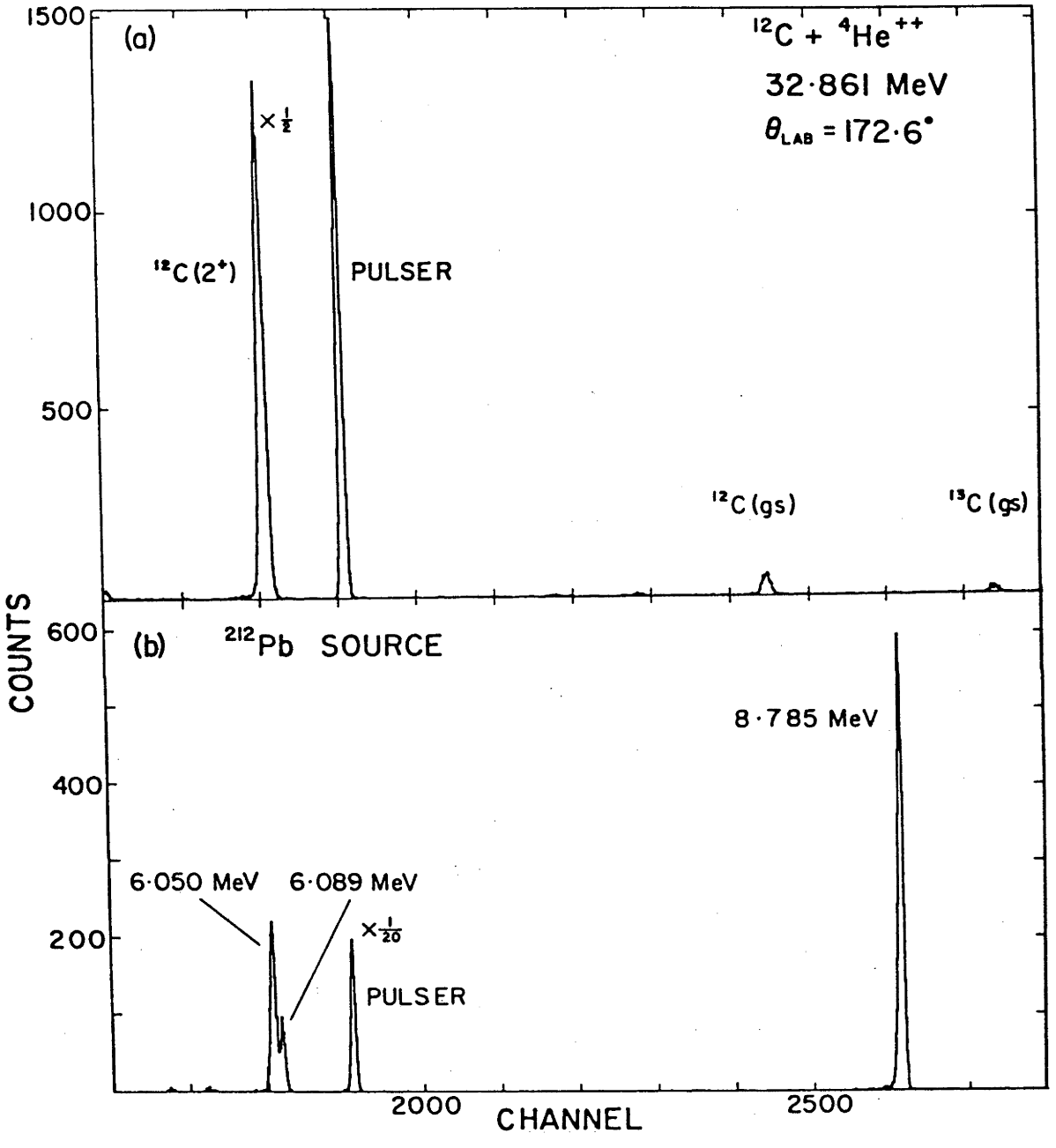

Fig. 3.9 (a) Spectrum of ^{4}He particles backscattered from a thin carbon target.

(b) Spectrum of ^{4}He particles from a ^{212}Pb radioactive source, at the same gain as spectrum (a).

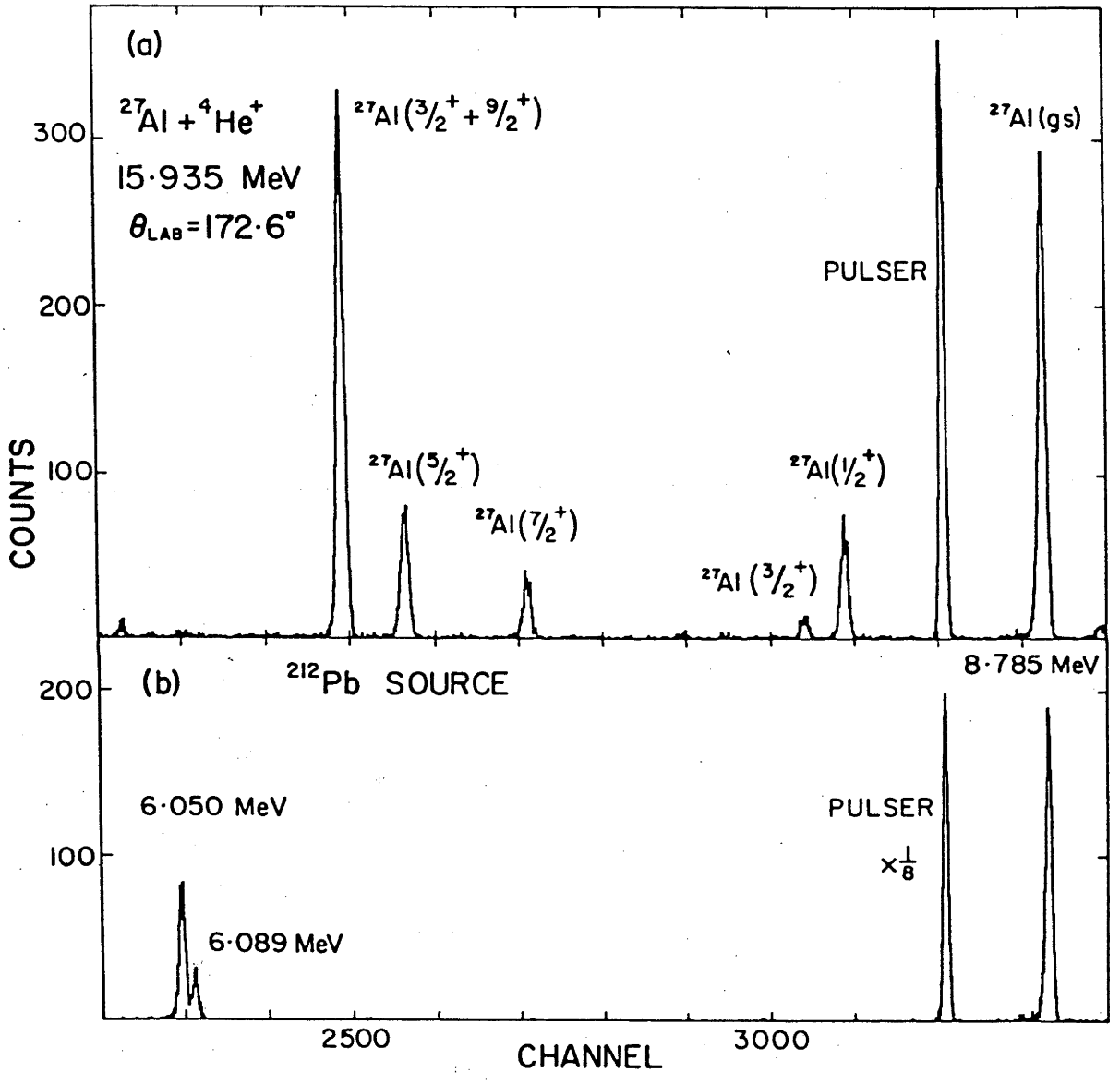

Fig. 3.10 (a) Spectrum of ^{4}He particles backscattered from a thin aluminium target.

(b) Spectrum of ^{4}He particles from a ^{212}Pb radioactive source, at the same gain as spectrum (a).

c) Calibration at B = 0.90 T.

The method used here was similar to that of calibration b). In this case, $^{4}He^{+}$ ions were elastically scattered from an Al target, and for a bombarding energy of ~ 15.9 MeV the elastic peak was compared to the 8.785 MeV group in the source spectra (see fig. 3.10). To obtain singly-charged ^{4}He ions, gas stripping was used instead of foil stripping.

In each case, the thickness of the target was measured. The carbon targets (~ 15 μg cm^{-2}) had a thin layer of gold (~ 1 μg cm^{-2}) evaporated on one surface (Ni was used for the Al targets because of its low diffusion coeffient). These targets were bombarded by ~ 42.5 MeV ^{16}O ions and the target thickness was determined from the shift in the Au (or Ni) elastic peak when the thin layer faced upstream or downstream. The energy calibration results are summarised in table 3.6 and fig. 3.11. (The values quoted take target thickness into account.) It can be seen that there is no significant variation in K as a function of magnetic field up to 0.9 T or as a function of time, and the value adopted was k = 78.07 ± 0.04. This determined beam energies to better than 0.1%.

Table 3.6 Summary of 14UD Pelletron energy calibration

Reaction	E_{bomb} (MeV)	B(T)	K (MeV.u/T^2)	
			Nov. 75	Jul. 76
$^{12}C(p,p_0)\ ^{12}C$	14.233	0.4303	78.104 ± 0.004	
$^{12}C(p,\alpha_0)\ ^{9}B$	14.233	0.4303	78.105 ± 0.030	78.007 ± 0.030 78.041 ± 0.030
$^{12}C(\alpha,\alpha_1)\ C$	32.861	0.6502	78.062 ± 0.010	78.093 ± 0.009
$^{27}Al(\alpha,\alpha_0)^{27}Al$	15.935	0.9046		78.097 ± 0.008

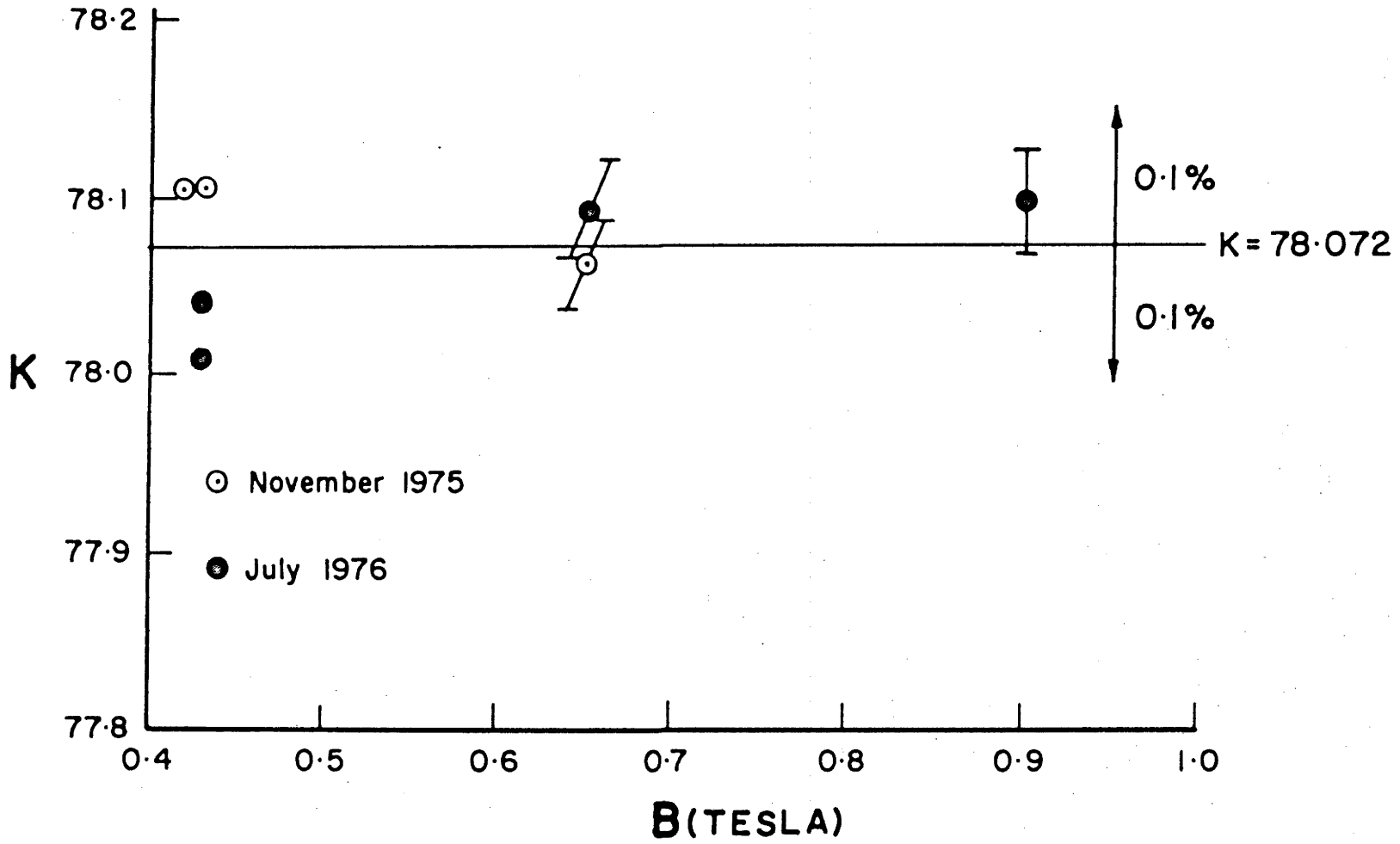

Fig. 3.11 Summary of magnetic constant determinations.

3.4.2 Calibration of the EN accelerator

The beam from the EN tandem was analysed by a 86 cm radius double-focussing magnet with a mass energy product (ME/q^2) of 52, and a maximum field of 1.2 T. This magnet had been precisely calibrated previously through (p,n) reaction threshold measurements (Mo69) and by using the $^{2}H(^{16}O,n)^{17}F$ reaction threshold (Es76). In addition, the calibration had been periodically monitored by comparing the energy of back-scattered ^{4}He beams with α-particle groups from a thin ^{212}Pb source (Es76). This practice was continued during the period of the current series of experiments particularly as the analysing magnet had been moved during the course of accelerator upgrading work.

The method used was similar to that described in part b) of subsection 3.4.1 for the 14UD Pelletron accelerator. Although earlier measurements (Mo66) showed that for this magnet differential hysteresis effect were negligible, as a precautionary measure the magnet was always recycled according to the procedure described for the 14UD. The object and image slits were set at 0.127 cm full aperture. A low energy calibration point was obtained with $\sim$ 9.53 MeV $^{4}He^{++}$ scattered from Au and detected at a mean laboratory angle of 171.6° in an annular counter. The elastic peak position (channel number) was compared with the position of the 6.0606 MeV doublet from the ^{212}Pb source. The target consisted of a thin ($\sim$ 5 μg cm^{-2}) layer of Au on a carbon backing; the Au thickness was measured from the shift in the ^{12}C elastic peak when the target was rotated 180°. A high energy calibration point was obtained with $\sim$ 15.93 MeV $^{4}He^{++}$ scattered from ^{27}Al, with the elastic peak corresponding in energy to the 6.0606 MeV doublet. The target

consisted of a carbon backing, half of which was coated with Al; the Al thickness was measured from the shift in the ^{12}C elastic peak as the coated and uncoated regions of the target were bombarded. The mean value obtained for the magnet constant was 19.967 ± 0.005 keV.u/MHz^2 and did not vary significantly between the data taken in February and March 1976.

CHAPTER 4

DATA REDUCTION AND EXCITATION PROBABILITIES

Data reduction consisted of extracting the areas of the elastic and inelastic peaks from the data so that experimental excitation probabilities defined by

$$R_{exp} = \left(\frac{d\sigma}{d\Omega}\right)^{lab}_{inel} \Big/ \left[\left(\frac{d\sigma}{d\Omega}\right)^{lab}_{el} + \left(\frac{d\sigma}{d\Omega}\right)^{lab}_{inel}\right] \qquad (4.1)$$

could be obtained. Since R_{exp} is a ratio, it was not necessary to measure absolute cross sections and the areas of the elastic and inelastic peaks could be substituted for $(d\sigma/d\Omega)^{lab}_{el}$ and $(d\sigma/d\Omega)^{lab}_{inel}$ respectively. In this chapter, sections 4.1 and 4.2 discuss the general methods employed in the extraction of peak areas. Subsequent sections consider the specific cases of each target and projectile. Data reduction in the ^{208}Pb experiment is treated separately from that for the ^{204,206}Pb experiments, because the lower excitation probabiliities raised problems specific to ^{208}Pb. The measured excitation probabilities are also discussed for each particular case, and the results are listed in tables 4.4, 4.5 and 4.6.

The accuracy of R_{exp} is determined entirely by the uncertainties in the measured peak areas. The statistical uncertainty in the peak areas is given by

$$\sigma_a = (A + B)^{\frac{1}{2}} \qquad (4.2)$$

where A is the net area of the peak, and B is the total background under the peak. However, eq. (4.2) assumes that one can obtain a very precise independent estimate of the background B. In practice, that is not usually possible and an additional contribution α_b must be included to take account of the uncertainty in the estimate of

the background used in calculating A. The total uncertainty in the peak area is then taken as

$$\sigma = \left(\sigma_a^2 + \sigma_b^2\right)^{\frac{1}{2}} \quad . \tag{4.3}$$

The uncertainties in the measured peak areas will be discussed for each particular situation later in this chapter.

4.1 Lineshape Analysis

Peak lineshape analysis was made necessary by the need to unfold the inelastic peak from the elastic peak tail. Although the same peak lineshapes were eventually used for all projectiles (^{4}He, ^{12}C, and ^{16}O), lineshapes were initially developed for the ^{16}O data since, for this data, tailing was the strongest. As a result, the present section will lay particular emphasis on the ^{16}O data.

Examples of ^{16}O spectra obtained for ^{204}Pb and ^{206}Pb are shown in figs. 4.1 and 4.2 respectively. Although the situation is emphasized by the logarithmic plots, the need to unfold the inelastic peak from the elastic peak tail can clearly be seen. The area of the elastic tail under the inelastic peak was typically 6.5% of the inelastic peak area for ^{206}Pb, and 1.4% for ^{204}Pb. The improvement for ^{204}Pb is reflected in the P/V ratios of about 30:1 (compared to 10:1 for ^{206}Pb) and is ascribed to the increased B(E2) value and, more importantly, to the higher excitation energy. To determine inelastic peak areas to 1% precision, it was necessary for the worst case (^{206}Pb) to evaluate the elastic tail area underneath the inelastic peak with an error no greater than 15%, and for this reason peak lineshapes were investigated.

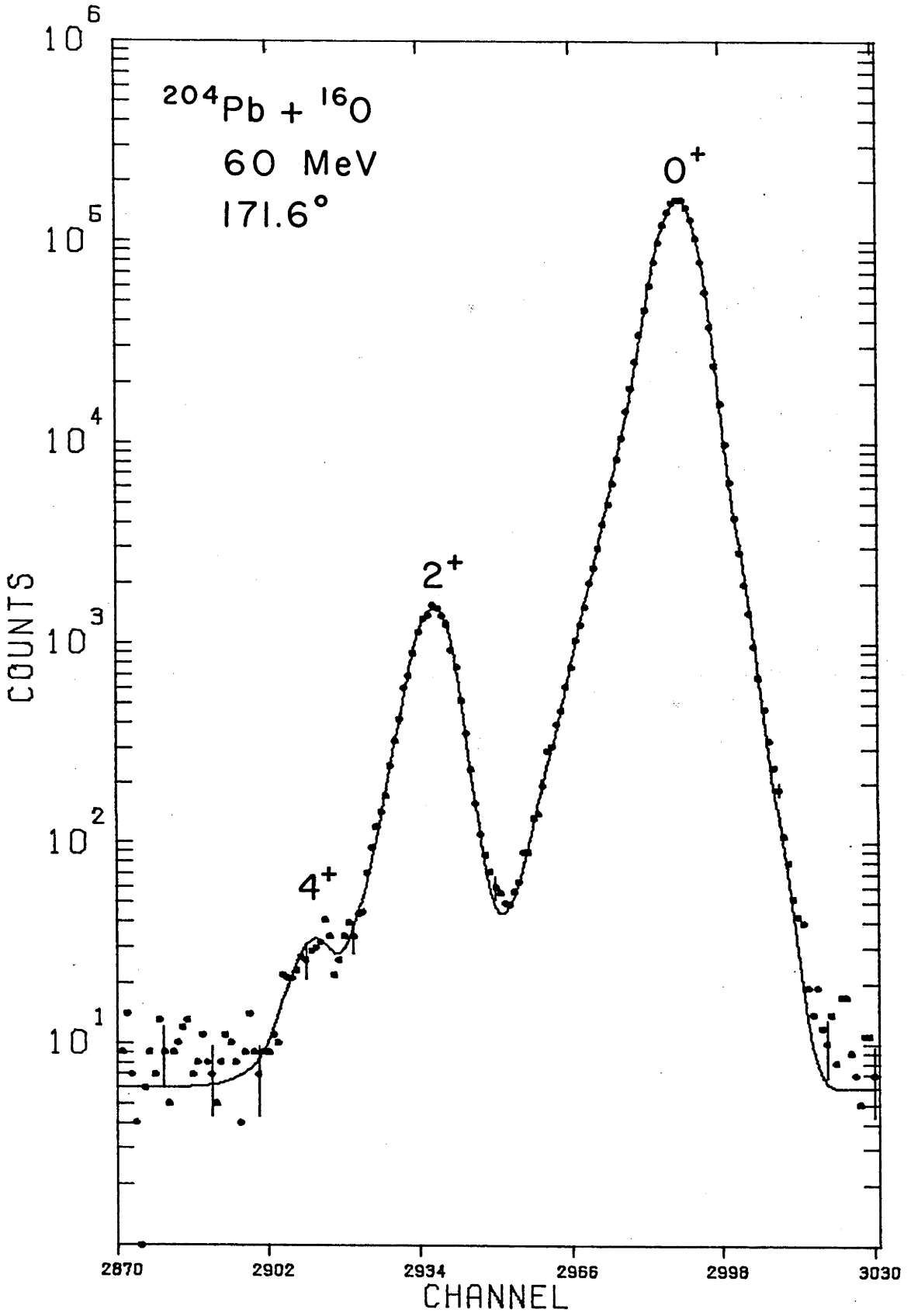

Fig. 4.1 Spectrum of 60 MeV ^{16}O projectiles backscattered from ^{204}Pb. The solid line represents a fit to the spectrum.

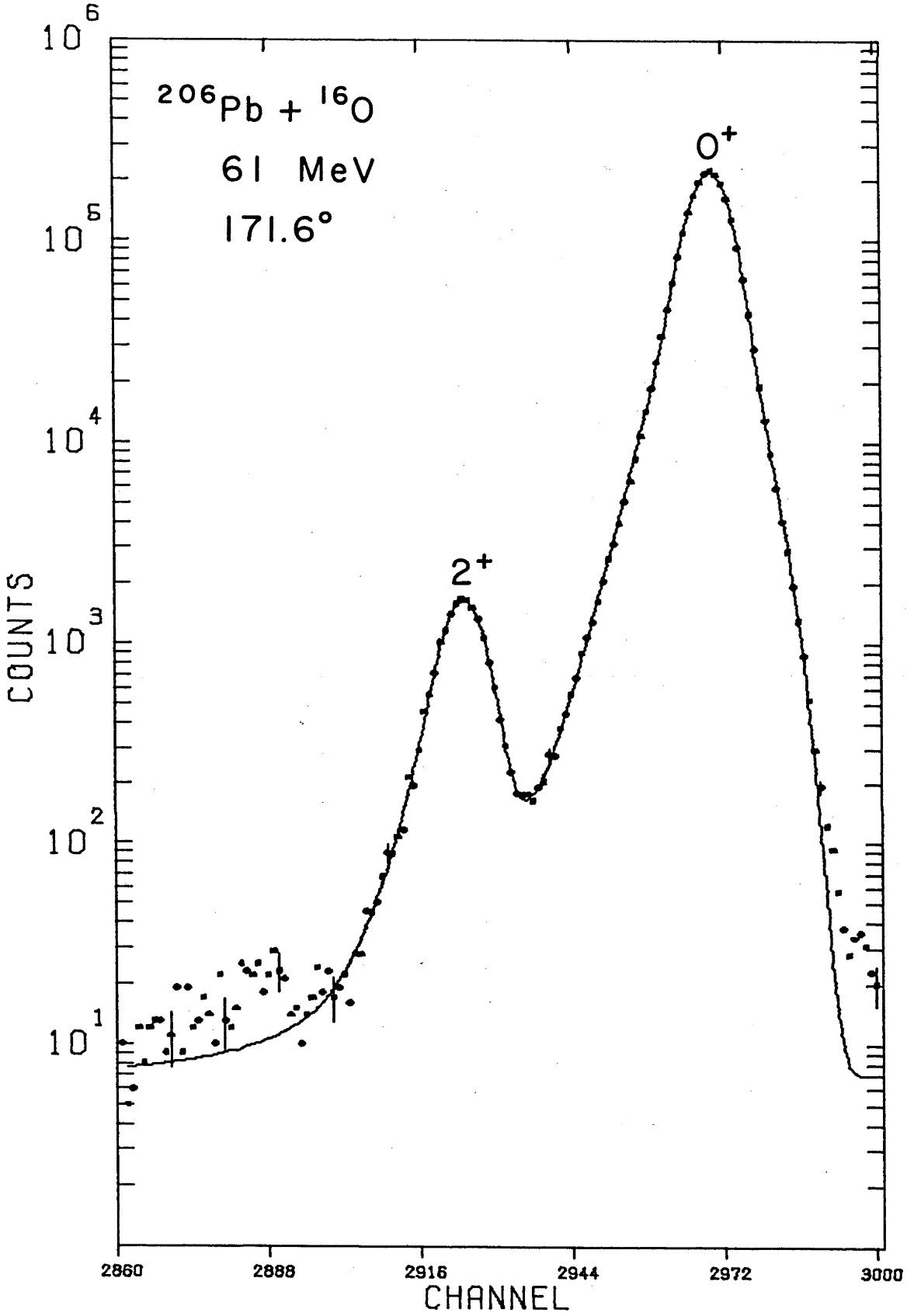

Fig. 4.2 Spectrum of 61 MeV ^{16}O projectiles backscattered from ^{206}Pb. The solid line represents a fit to the spectrum.

The lineshape in all spectra was found to be non-symmetric. The peak shape down to the 10% level of the maximum peak height could be reproduced closely by a Gaussian function expressed in the form

$$HT.\exp(-z^2/2\sigma^2) \tag{4.4}$$

where

$$\sigma = FWHM.(2\ln 2)^{-\frac{1}{2}} \tag{4.5}$$

and

HT = peak height
FWHM = the full width at half maximum of the peak
z = x - POS
x = channel number
POS = peak position.

Better fits were obtained by using a skewed Gaussian where different values for FWHM were used to fit the high energy side (FWHM1) and low energy side (FWHM2) of the peak. (These then give rise to different values σ_1 and σ_2.)

Below the level of 10% of the maximum peak height, a tail was observed to extend on the low energy side of peaks and this shape could no longer be adequately represented by the Gaussian function above. The shape of the elastic tail was determined by studying ^{208}Pb spectra (see fig. 4.12) since the peak corresponding to the first excited state at 2.615 MeV is well separated from the elastic peak. The elastic tail was found to be linear on a logarithmic plot and could be fitted well with the expression

$$A_1.[1 - \exp(-z^2/2\sigma^2G_1^2)].\exp(-C_1.|z|) \tag{4.6}$$

where parameters C_1 and G_1 determine the decay rate of the tail and parameter A_1 its height. The term in square brackets makes the tail contribution very small in the region near the top of the peak which is well described by the Gaussian function.

Below the 0.1% level of the maximum peak height, a shallow "long range" tail was observed on the low energy side and this tail was also fitted with expression (4.6) where a different set of parameters A_2, C_2, and G_2 were allowed to vary. This tail was particularly of relevance in the ^{4}He data, and in the ^{208}Pb experiment where the inelastic peak was further away from the elastic peak.

During computer fitting, a small"lump"(barely visible in the region of channel 2980 in fig. 4.2) was always apparent on the high energy side of the elastic peak in the ^{16}O and ^{12}C data. It was found that this"lump"could be accounted for analytically by including an extra term

$$\text{HT. F. } \exp(-(z-P)^2/2\sigma^2) \ , \qquad (4.7)$$

which is a Gaussian function similar to eq. (4.4). In eq. (4.7), P is the position of the"lump"relative to the peak position, and F is the fractional height of the "lump" relative to the peak height. In the ^{16}O data, investigations of ^{204}Pb, ^{206}Pb, and ^{208}Pb spectra showed that the position of the "lump" relative to the peak position was approximately constant and its height remained between 1% and 2% of the elastic peak height, the average being 1.6%. (In the ^{12}C data the average height of the "lump" was 0.8%.) In the ^{204}Pb and ^{206}Pb spectra obtained with ^{16}O projectiles, the "lump" could correspond to elastic peaks from contaminants with masses A = 206 and A = 208 respectively. However, in the ^{208}Pb spectra the "lump" would correspond to a contaminant with mass A = 210; this was not only not observed in the ^{204}Pb and ^{206}Pb spectra, but the longest-lived nucleus of this mass is ^{210}Pb (half life of 22 years) and its presence in the target is most unlikely. One can only conclude that this"lump"was due purely to a detector effect.

In all spectra, a background was usually observed above the elastic peak and below the inelastic peak. The height of this background was usually very low (in the worst case the background height was 0.45% of the inelastic peak height) but to improve the fit to the data a flat background, whose height was determined by the parameter BGND, was included in the analytic expression for the spectrum.

As a result of the previous discussion, the analytic function used to fit the data had the explicit form

$$f(z) = HT.\exp(-z^2/2\sigma_1^2) + HT.F.\exp(-(z-P)^2/2\sigma_1^2) + BGND \quad \text{for } z \geq 0 \qquad (4.8a)$$

$$f(z) = HT.\exp(-z^2/2\sigma_2^2) + HT.A_1.[1 - \exp(-z^2/2\sigma_2^2G_1^2)].\exp(-C_1|z|) + HT.A_2.[1 - \exp(-z^2/2\sigma_2^2G_2^2)].\exp(-C_2|z|) + BGND \quad \text{for } z < 0 \; . \qquad (4.8b)$$

Fits to the data are shown in figs. 4.1 and 4.2.

A computer program was used to fit the above function to the data. Provision was made to fit up to 4 peaks each with the same shape (a good assumption for a surface barrier detector when detecting identical projectiles with similar energies) but with heights and positions that could be varied. Using the method of least squares, the goodness of the fit was estimated by calculating the weighted sum of squares of deviations of the data from the fitted curve, i.e.

$$\chi^2 = \Sigma \; [(y_i - f(z_i))^2/y_i] \qquad (4.9)$$

where y_i = number of counts in channel x_i.

The value of χ^2 was minimised using the subroutine FITTEM, written by Hay (Ha69a), to optimise up to 19 parameters (POS_{1-4}, HT_{1-4}, FWHM1, FWHM2, F, P, $A_{1,2}$, $G_{1,2}$, $C_{1,2}$ and BGND). The advantage of this subroutine is that the algorithm employed does not require the partial derivatives of function (4.8) with respect to each variable parameter; this meant that during the course of program development modifications to function (4.8) could be tested quickly.

The validity of the analytical function (4.8) and of the fitting procedure was verified by fitting ^{204}Pb and ^{206}Pb spectra with a lineshape obtained from ^{208}Pb data; only peak heights and positions were allowed to be adjusted. The result of this test is illustrated in fig. 4.3 for the same spectrum as in fig. 4.2, and it can be seen that a reasonable fit is obtained. Although the shape of the elastic peak tail is well reproduced, this tail is too high by about 25% (this is ascribed to the ^{208}Pb target being thicker by a factor of 2). Even so, there is only a 2% decrease in the inelastic peak area, and this is only twice the statistical error.

4.2 Peak Area Determination

The computer program described previously was used to calculate peak areas by integrating function (4.8) channel by channel; this will be referred to as the "full fit" method. In addition, a "Gaussian area" was calculated for each peak from

$$A = (2\pi)^{\frac{1}{2}}.\sigma.HT \qquad (4.10)$$

where in this case $\sigma = (\sigma_1 + \sigma_2)/2$. While there is no reason to suppose that the peaks in the spectra should be perfectly Gaussian, comparing the "Gaussian area" with the "full fit area" provided a measure of the importance of tailing. It was found that, in general,

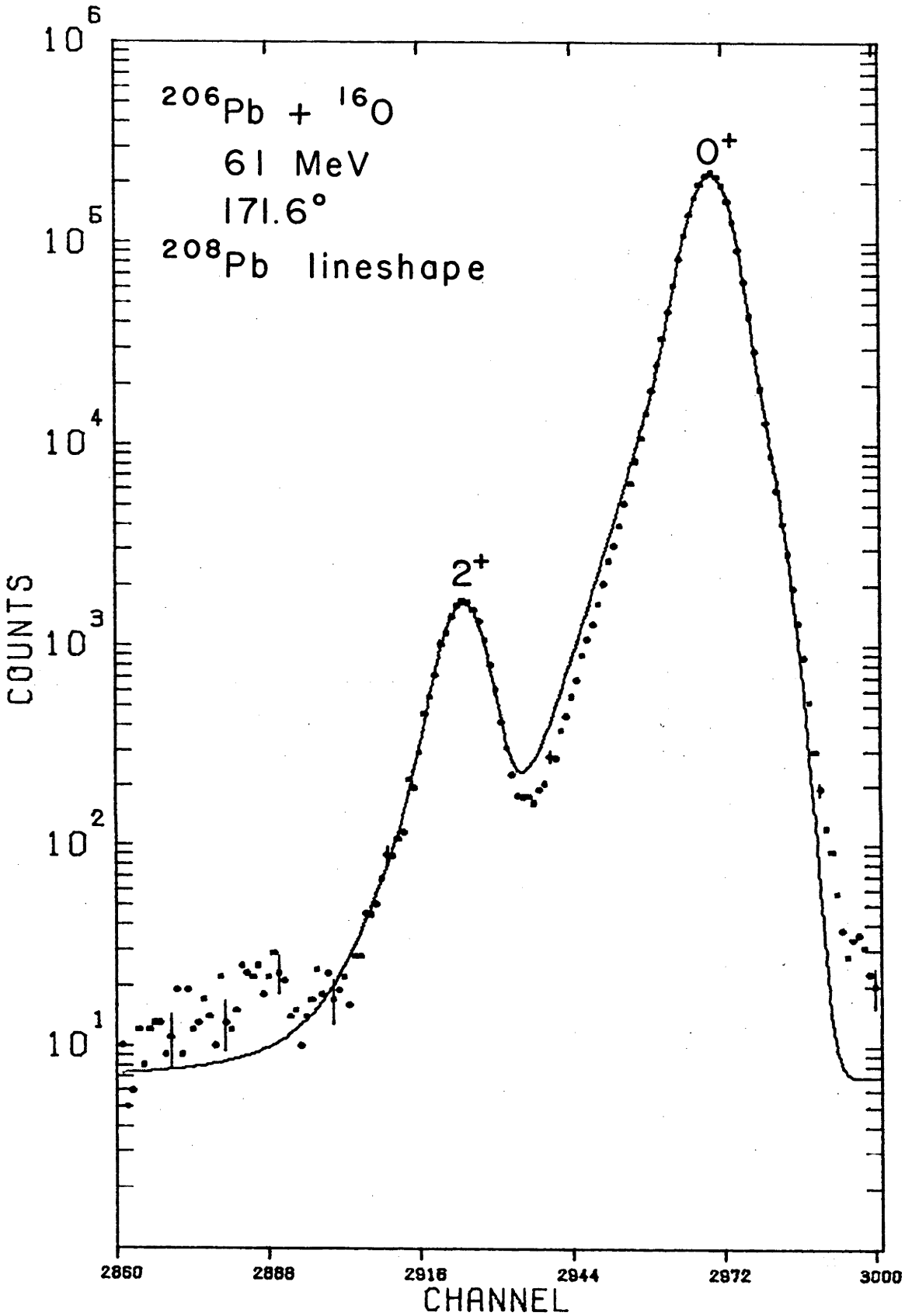

Fig. 4.3 The same spectrum as in fig. 4.2. The full curve represents a fit to the spectrum using the lineshape obtained from a ^{208}Pb target; only peak positions and heights were allowed to vary in the fitting procedure.

tails accounted for about 14% of the total peak area for ^{16}O, 12% for ^{12}C, and only 5% for ^{4}He.

A second method - the "partial fit" method - was also employed to determine peak areas. The inelastic peak area was determined by summing the data over a range of channels and then subtracting the computed elastic peak tail as obtained from the computer fit. The upper and lower channels defining the range of summation for the inelastic peak were chosen to be those where the number of counts in the channel first showed a significant difference from the computed elastic peak tail; the level of significance being $\chi^2 \geq 10$. While the range of summation might visually appear too restrictive, it was found that areas obtained by this method were at least 99% of those obtained directly from the computer program. Moreover, the measured excitation probabilities were not affected since they were determined from area ratios.

The elastic peak area was obtained by summing the data over a corresponding range of channels, these being deduc ed from knowledge of the peak positions (obtained from the computer fit). Although this procedure gave rise to summation limits expressed in fractions of a channel, for simplicity only integral channels were summed. The resulting uncertainty was less than 0.1% of the elastic peak area and was therefore negligible.

The excitation probabilities calculated using the areas obtained from the "full fit" and "partial fit" methods were found to be in good agreement. The average difference, for all spectra, between the two methods was about 0.6%, with 1.9% for the worst case. Although the results from the two methods agreed well, the

"partial fit" method was considered preferable for the following reasons:

a) The computer fit was essentially used only to estimate the background under the inelastic peak; errors arising from poor fits to other parts of the spectrum were therefore eliminated.

b) It has been shown (Be69) that if the data follows a Poisson distribution (as for a counting experiment) the method of least squares consistently underestimates the area under a peak by an amount approximately equal to χ^2_{min} (where χ^2_{min} is the minimum value of χ^2 obtained from eq. (4.9) after the computer fit), i.e.

$$\chi^2_{min} \approx \text{area (data)} - \text{area (fit)} . \qquad (4.11)$$

(In the computer fits the value of χ^2_{min} for a spectrum, divided by the number of channels, ranged from 1 to 7.) Taking this effect into account reduced the average difference between the "full fit" and "partial fit" methods to about 0.4%.

c) By summing only over channels which significantly contribute to the peak area, the error in the peak area, arising from the need to estimate the background was reduced.

d) The restricted range of summation meant that fewer elastic contaminant peaks might be included. Therefore, fewer impurities that might affect the data needed to be considered.

For these reasons, all excitation probabilities were calculated using peak areas obtained with the "partial fit" method.

4.3 The ^{204}Pb and ^{206}Pb Experiments

Although the excitation probabilities for ^{204}Pb were about 40% greater than for ^{206}Pb, the two experiments were very similar and they have been treated together in this section. Compared to ^{204}Pb, the lower excitation probabilities and the lower excitation energy of the 2^+ state in ^{206}Pb, gave rise to lower peak-to-valley ratios and consequently larger uncertainties in the measured excitation probabilities; this will be pointed out where appropriate in this section.

4.3.1 The ^{16}O Data

The analysis of the ^{16}O data has already been discussed, in part, in section 4.1 and examples of fits to the data are shown in figs. 4.1 and 4.2. The errors in the inelastic peak areas were calculated from eq. (4.3). The contribution σ_b arising from the uncertainty in the height of the elastic tail was estimated by observing the effect that raising or lowering the tail had on the quality of the fit. Fig. 4.4 shows the result when the elastic peak tail in fig. 4.2 is raised or lowered by 20%; the quality of the fit is clearly worse. Therefore, the uncertainty in the elastic tail area was conservatively estimated at between 15% and 25%, and for most of the spectra 20%. When this uncertainty was combined with statistical uncertainties (σ_a) the errors in the measured excitation probabilities (listed in tables 4.4a and 4.5a) were, on the average, 1.0% for ^{204}Pb and 1.6% for ^{206}Pb.

Fig. 4.5 shows a spectrum for ^{206}Pb taken with 72 MeV ^{16}O; a very similar spectrum was obtained for ^{204}Pb. A number of prominent peaks from the ^{206}Pb(^{16}O,^{17}O)^{205}Pb, ^{206}Pb(^{16}O,^{15}N)^{207}Bi, and

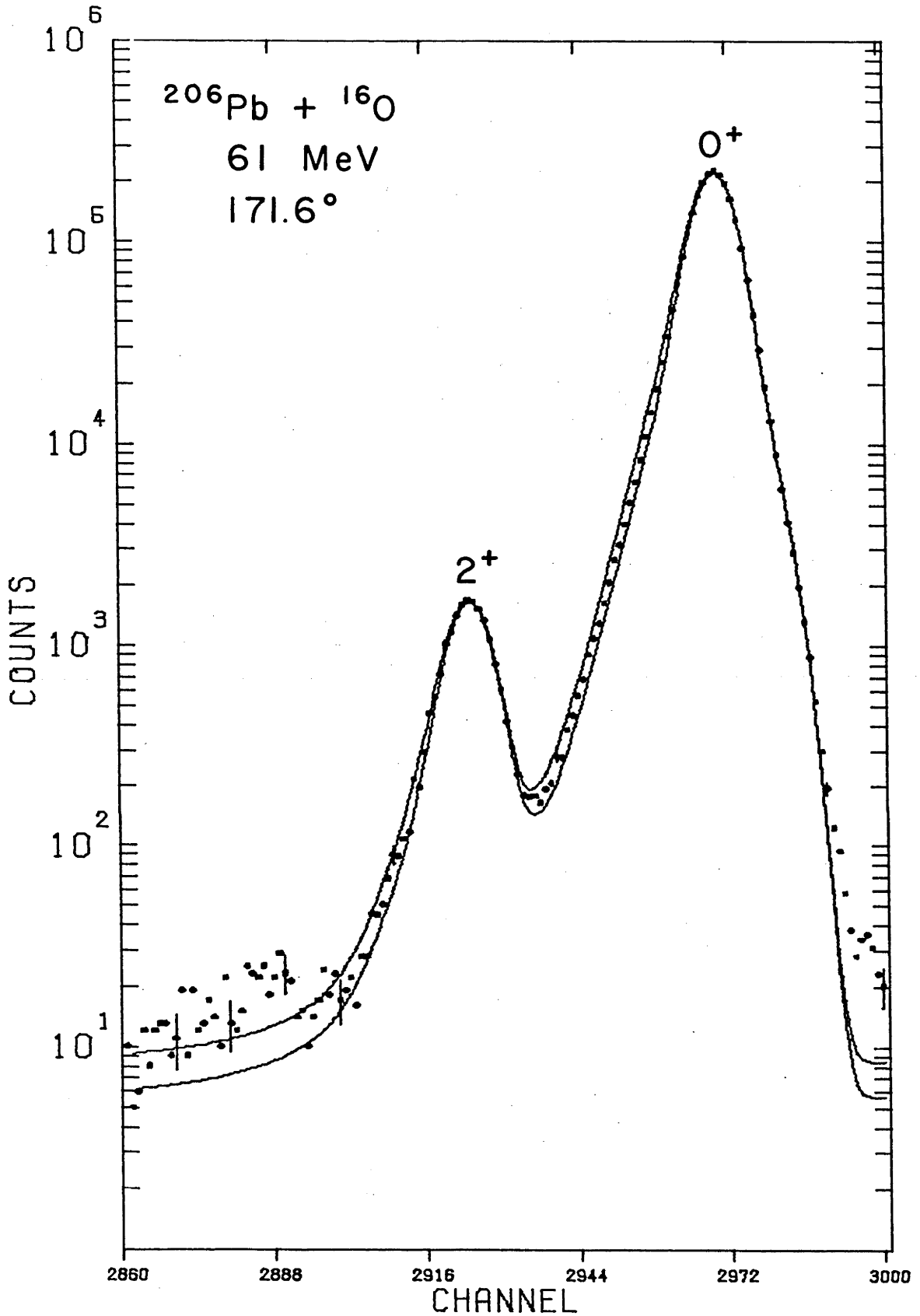

Fig. 4.4 The same spectrum as in fig. 4.2. The full curves show the effect of raising or lowering the elastic peak tail by 20%.

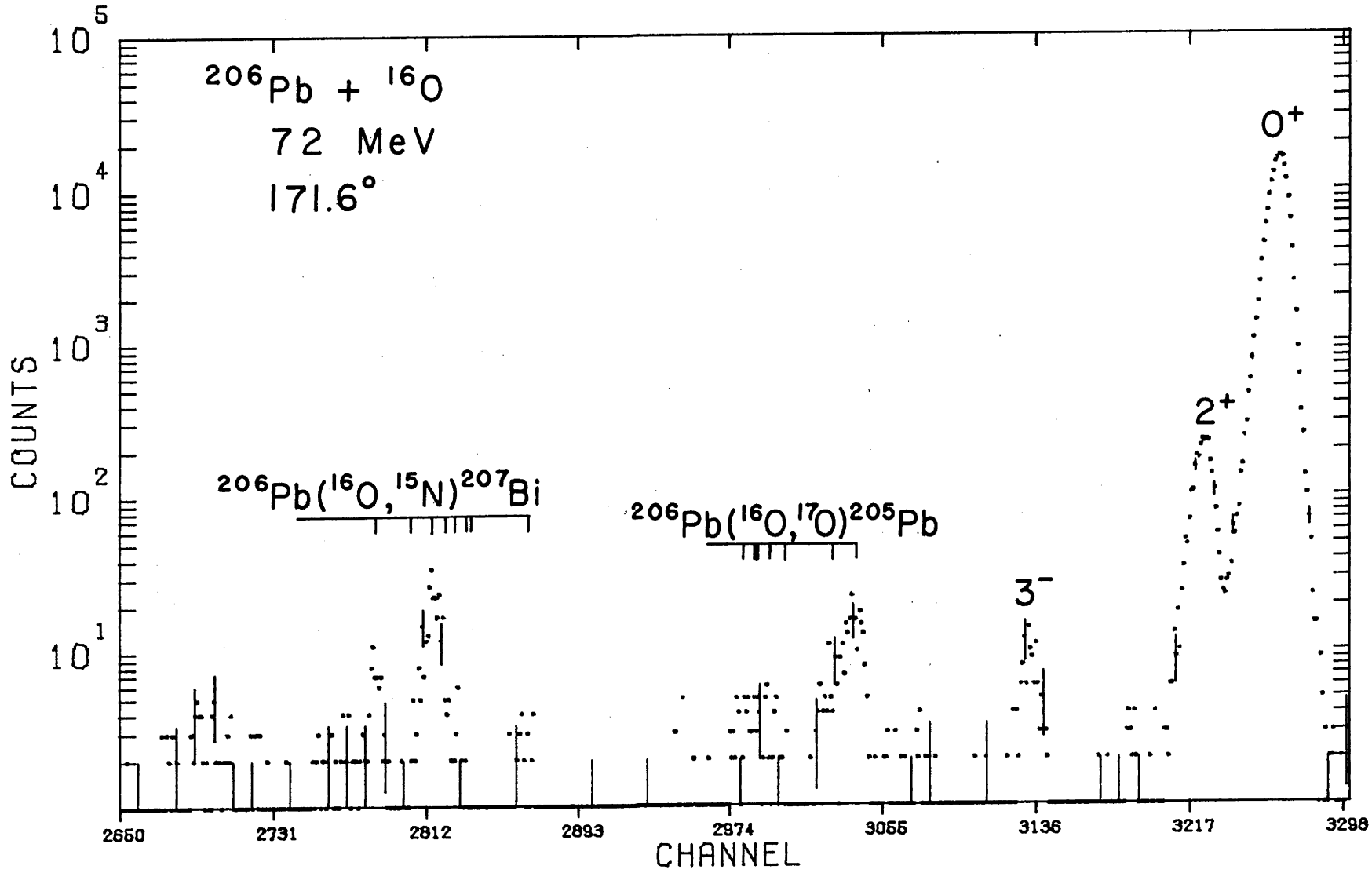

Fig. 4.5 Spectrum of 72 MeV ^{16}O projectiles backscattered from ^{206}Pb. Single nucleon transfer peaks are clearly visible.

$^{206}Pb(^{16}O,^{15}O)^{207}Pb$ single nucleon transfer reactions can be observed, but these are well below the 2^+ and 3^- inelastic peaks and do not interfere with the extraction of inelastic peak areas. The intensity of the single nucleon transfer peaks was observed to decrease rapidly as the bombarding energy was decreased. With the exception of the 1.274 MeV 4^+ state in ^{204}Pb, the 3^- state near 2.6 MeV in ^{204}Pb and ^{206}Pb was the only excited state observed to be populated in addition to the first 2^+ state. The excitation probabilities for the 3^- state were measured for bombarding energies from 59 MeV to 75 MeV, and these are listed in tables 4.4a and 4.5a; the large uncertainties (6-20%) are due to the small number of counts in these peaks.

4.3.2 The ^{12}C Data

Typical ^{12}C spectra, including fits to the data, are shown in figs. 4.6 and 4.7 for ^{204}Pb and ^{206}Pb respectively. A prominent feature of these data is a small shoulder located between the elastic and inelastic peaks (at about channel 3280 and 3020 in figs. 4.6 and 4.7 respectively). This shoulder was studied by treating it as a peak in the lineshape fitting program, and it was found that, in both the ^{204}Pb and ^{206}Pb data, its height was constantly 0.05% of the elastic peak height and its position remained 477 keV below the elastic peak. When $^{208}Pb\,S$ targets (rather than $^{204,206}Pb\,Cl_2$) were bombarded with ^{12}C ions, and later with ^{18}O ions, the shoulder was again observed. The possibility of a contaminant in the target producing an elastic peak is considered unlikely since in each case (^{12}C on $^{204}PbCl_2$, $^{206}PbCl_2$, and ^{208}PbS, and ^{18}O on ^{208}PbS) the shoulder would correspond to a different contaminant. It is therefore considered likely that the shoulder was produced by a detector effect, and this was later confirmed by its disappearance when the detector was replaced

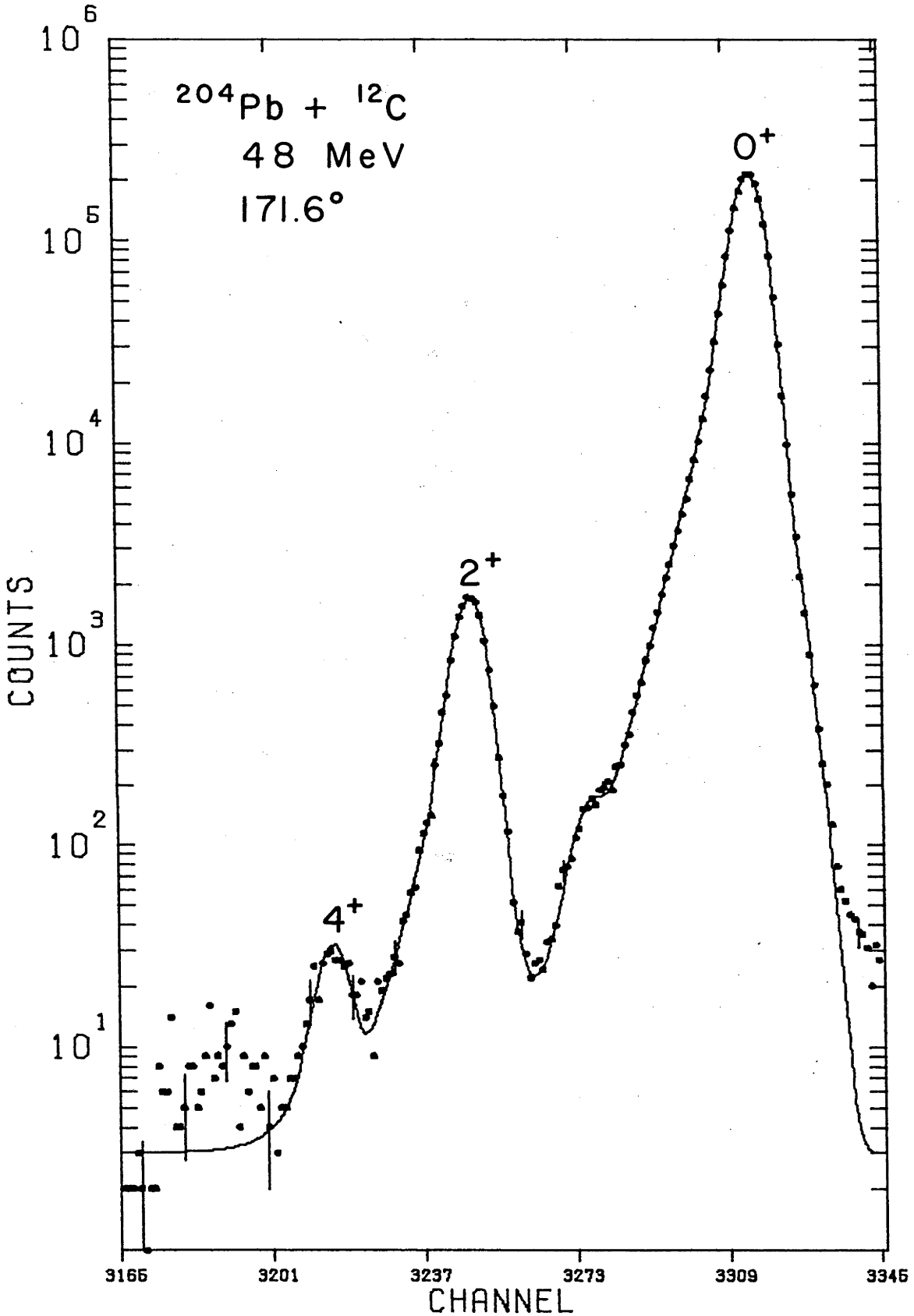

Fig. 4.6 Spectrum of 48 MeV ^{12}C projectiles backscattered from ^{204}Pb. The solid line represents a fit to the spectrum.

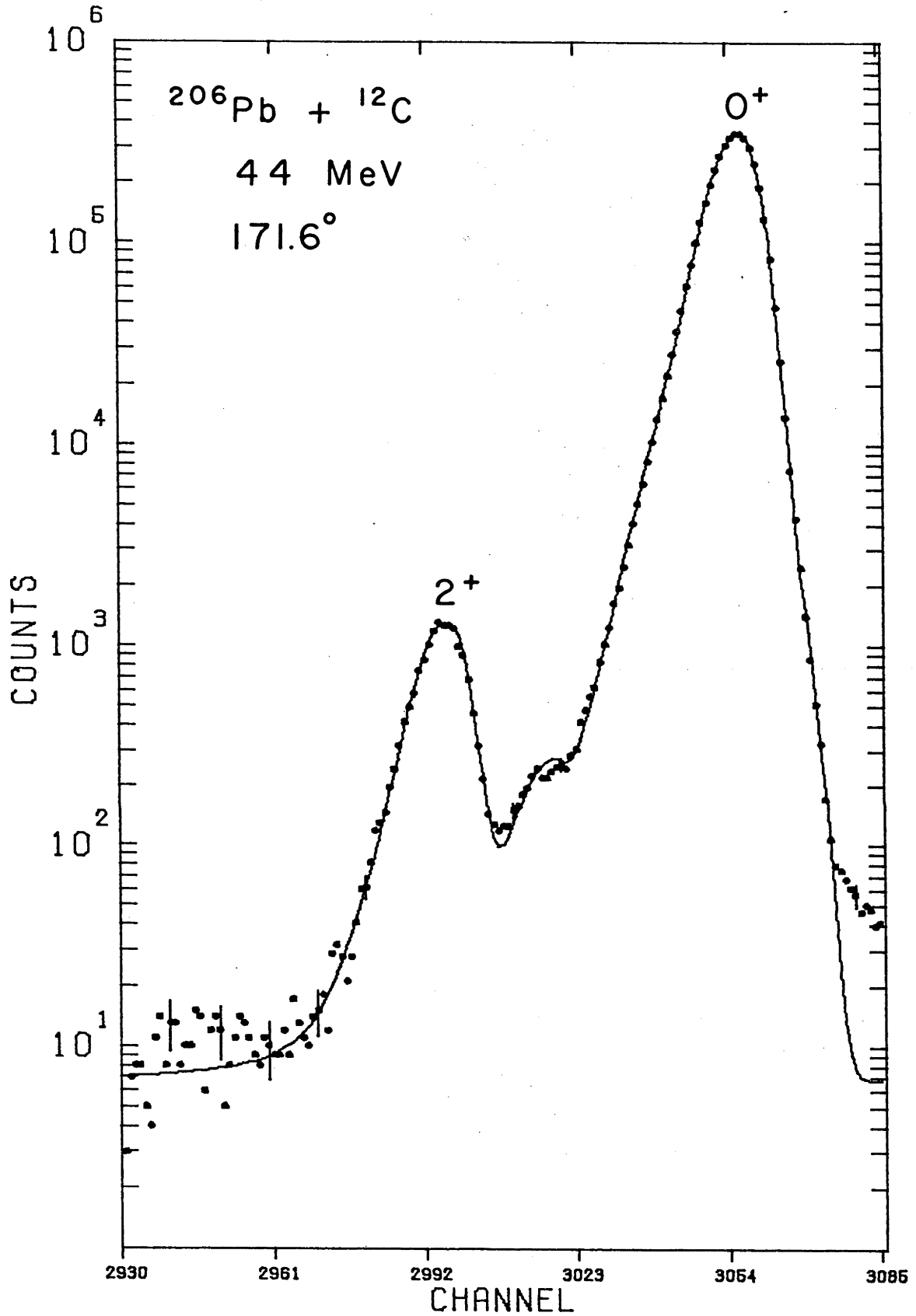

Fig. 4.7 Spectrum of 44 MeV ^{12}C projectiles backscattered from ^{206}Pb. The solid line represents a fit to the spectrum.

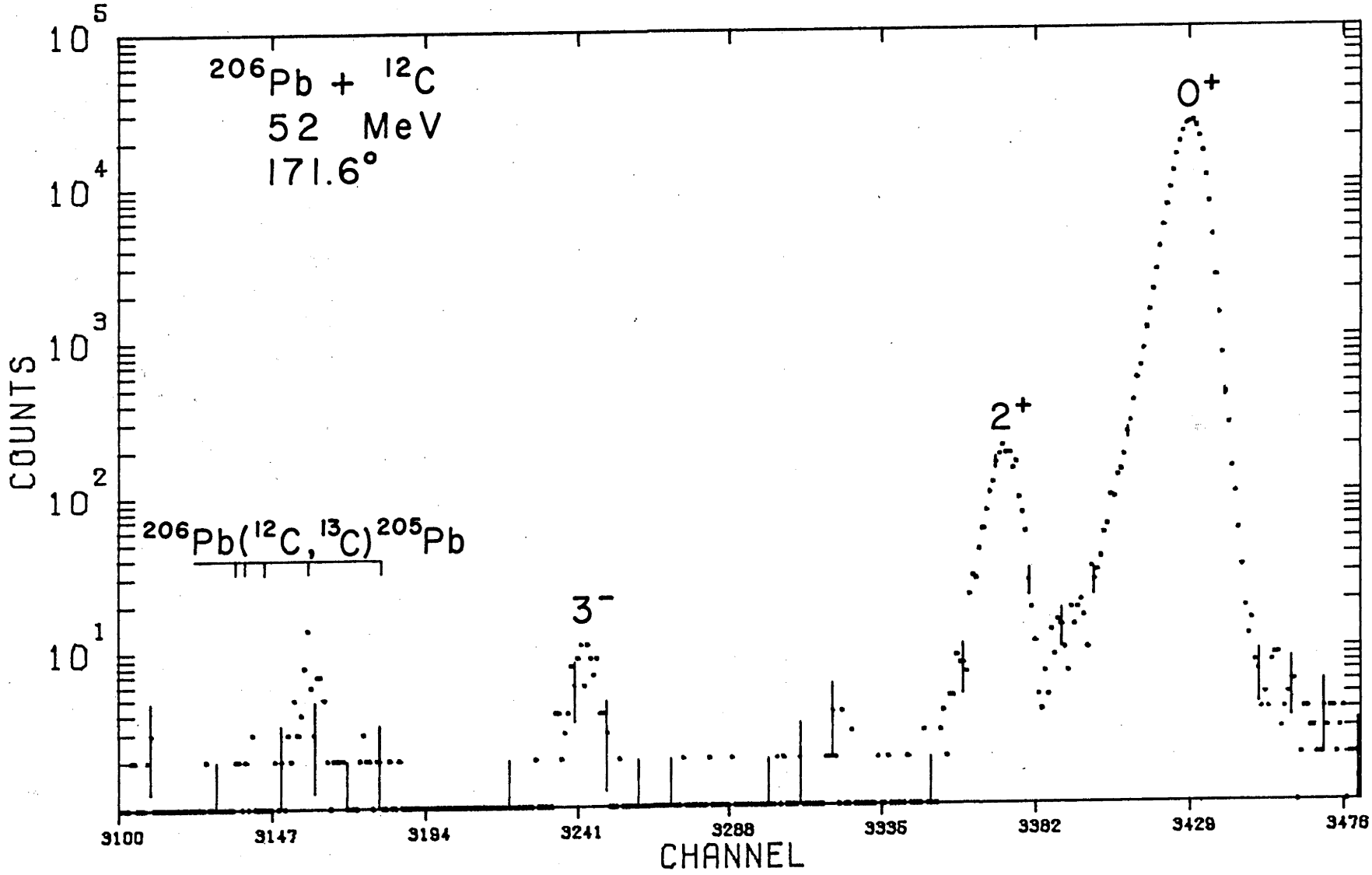

Fig. 4.8 Spectrum of 52 MeV ^{12}C projectiles backscattered from ^{206}Pb. Single nucleon transfer peaks are indicated.

by another.

Although the presence of this shoulder reduces the visual quality of the data, its effect on excitation probabilities was small. It seemed unnecessary to repeat the lengthy ^{12}C measurements with another detector merely for the sake of appearances. Despite this shoulder the ^{12}C spectra were of better quality than those using ^{16}O. With ^{12}C ions there was a marked decrease in the elastic peak tail and an improvement in energy resolution. Peak-to-valley ratios for the spectra shown are 74:1 and 13:1 for ^{204}Pb and ^{206}Pb respectively. The elastic tail under the inelastic peak is, on average, only 0.75% of the inelastic peak area for ^{204}Pb and 2.3% for ^{206}Pb; consequently the uncertainty σ_b (typically 20%) in the tail area, obtained from the lineshape fitting program, contributes much less to the error in the measured excitation probabilities than in the ^{16}O data. Results are listed in tables 4.4b and 4.5b.

For both ^{204}Pb and ^{206}Pb, the 3^- state near 2.6 MeV and single nucleon transfer peaks from the reaction $^{206}Pb(^{12}C,^{13}C)^{205}Pb$ were observed; an example is shown in fig. 4.8. Excitation probabilities for the 3^- state were measured to 7-20% accuracy and these are listed in tables 4.4b and 4.5b.

4.3.3 The ^4He Data

Representative ^4He spectra are shown in figs. 4.9 and 4.10 for ^{204}Pb and ^{206}Pb respectively. As can be seen, the spectra show evidence of pulse pile-up giving rise to a tail on the high energy side of the elastic peak. This pile-up, which is the result of the high count rates in the Pb elastic peak and in other elastic scattering

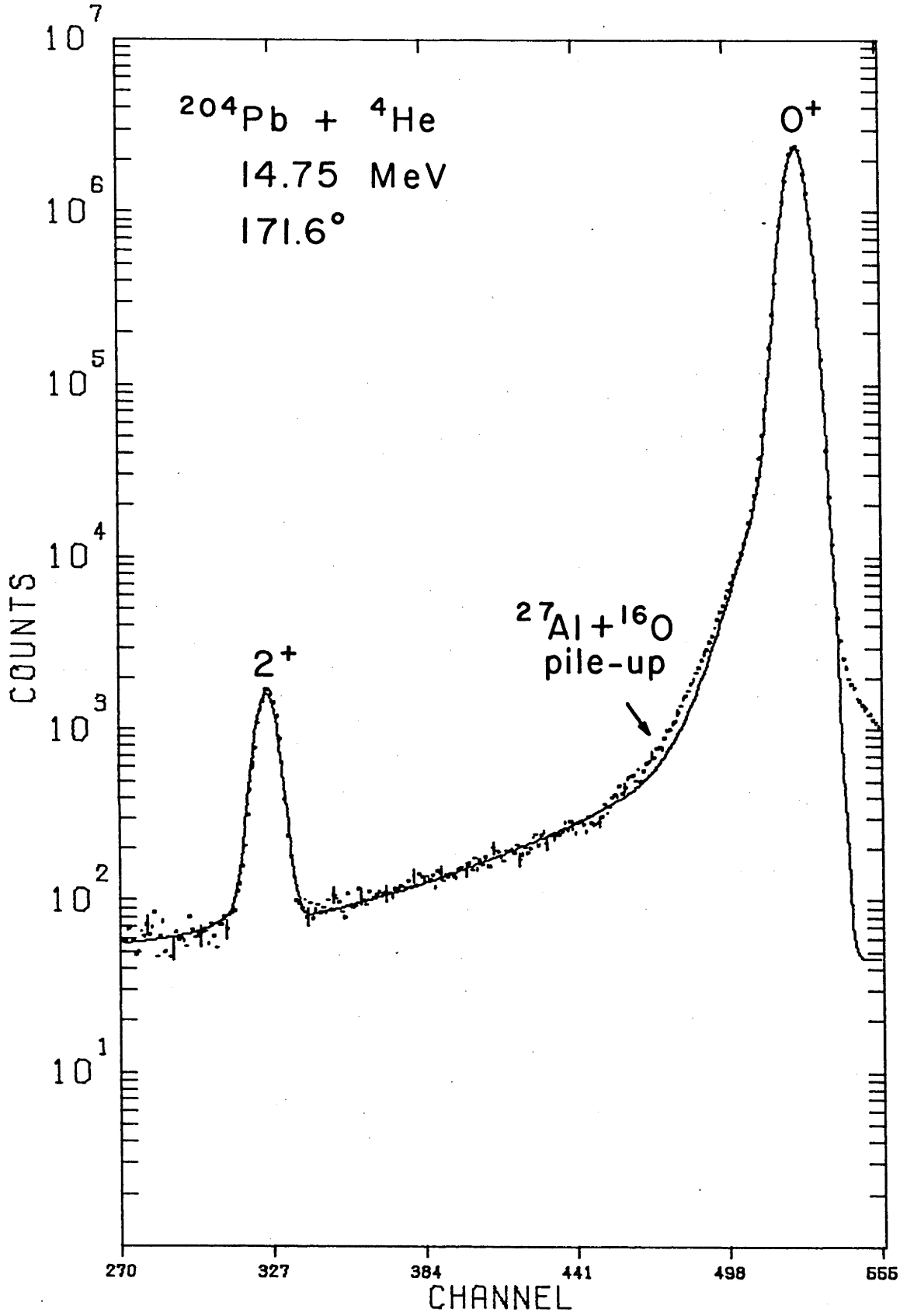

Fig. 4.9 Spectrum of 14.75 MeV ^{4}He projectiles backscattered from ^{204}Pb. The solid line represents a fit to the spectrum.

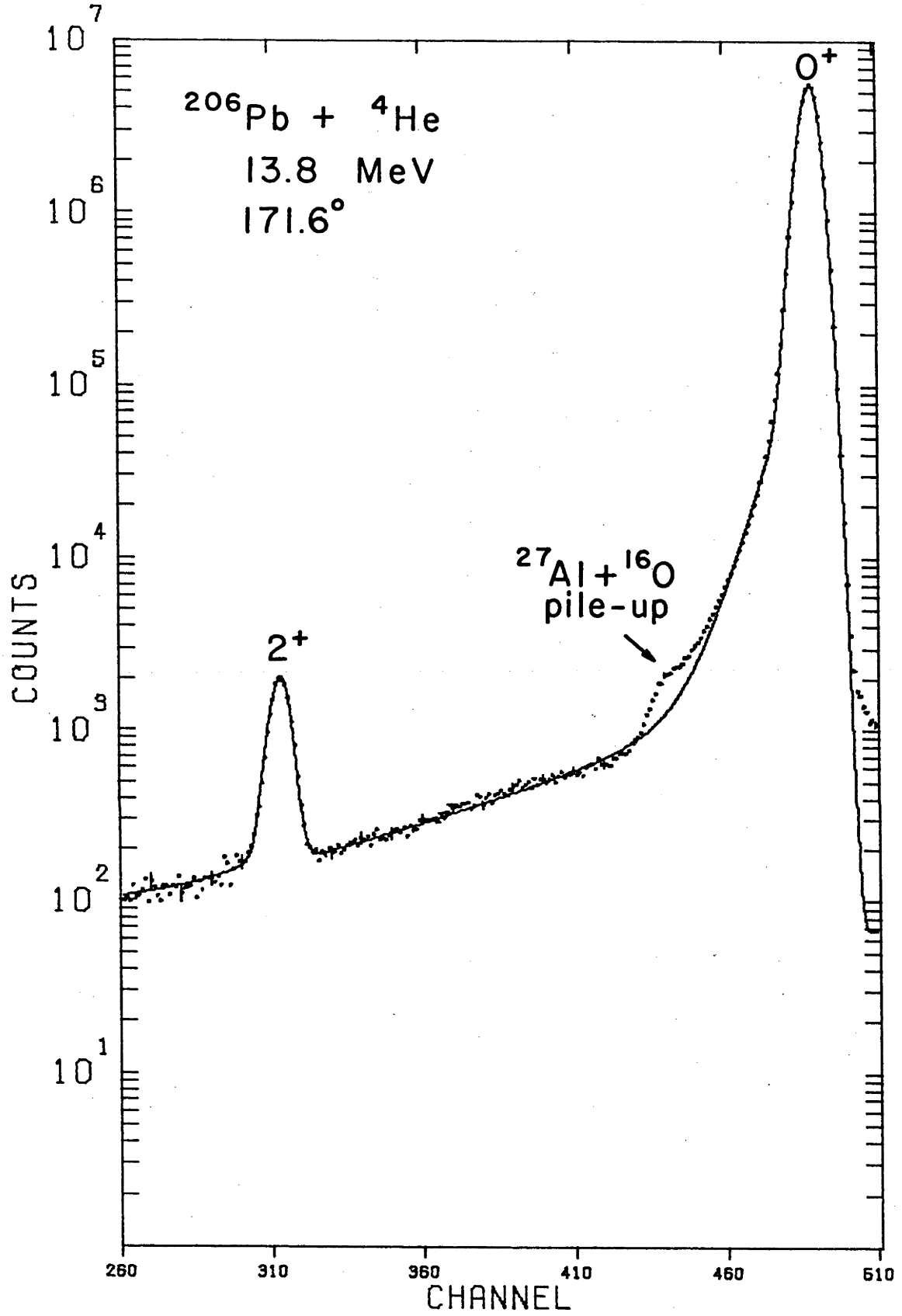

Fig. 4.10 Spectrum of 13.8 MeV ^{4}He projectiles backscattered from ^{206}Pb. The solid line represents a fit to the spectrum.

peaks (for example ^{16}O, ^{27}Al and ^{35}Cl) in the spectra, is more prominent in the ^{4}He data than in the ^{12}C and ^{16}O data because of the need to use thicker targets and larger beam currents (particle nanoamps), in view of the lower excitation probabilities. This pile-up is estimated to have a negligible (< 0.1%) effect on the measured elastic peak areas.

An additional feature of the ^{4}He data for $^{204,206}Pb$ is that the background in the region of the inelastic peak is produced, in the main, by pulse pile-up arising from projectiles elastically scattered from ^{27}Al and ^{16}O in the target (see subsection 3.3.1). The peak of this pile-up (due to particles scattered from ^{27}Al and ^{16}O arriving simultaneously at the detector) can be observed merged with the low energy tail of the elastic peak (as indicated in figs. 4.9 and 4.10), but by virtue of the "partial fit" method, described in section 4.2, it is excluded from the summation range used for the elastic peak and has no effect on the measured area. However, the pile-up tail in the region of the 2^{+} peak contributes to the reduction of the peak-to-valley ratios; these are 21:1 and 11:1 for figs. 4.9 and 4.10 respectively.

On a logarithmic scale, the background near the inelastic peak is seen to be sloping approximately linearly, and this suggests that the best fit may be obtained with an exponential function. This was accomplished by using the lineshape fitting program described in section 4.1 since when sufficiently far below the elastic peak, eq. (4.8b)reduces to

$$f(z) = HT.A_2.\exp(-C_2|z|) + BGND \quad z >> 1 \ . \tag{4.12}$$

The uncertainty σ_b in the height of the background f(z) was estimated,

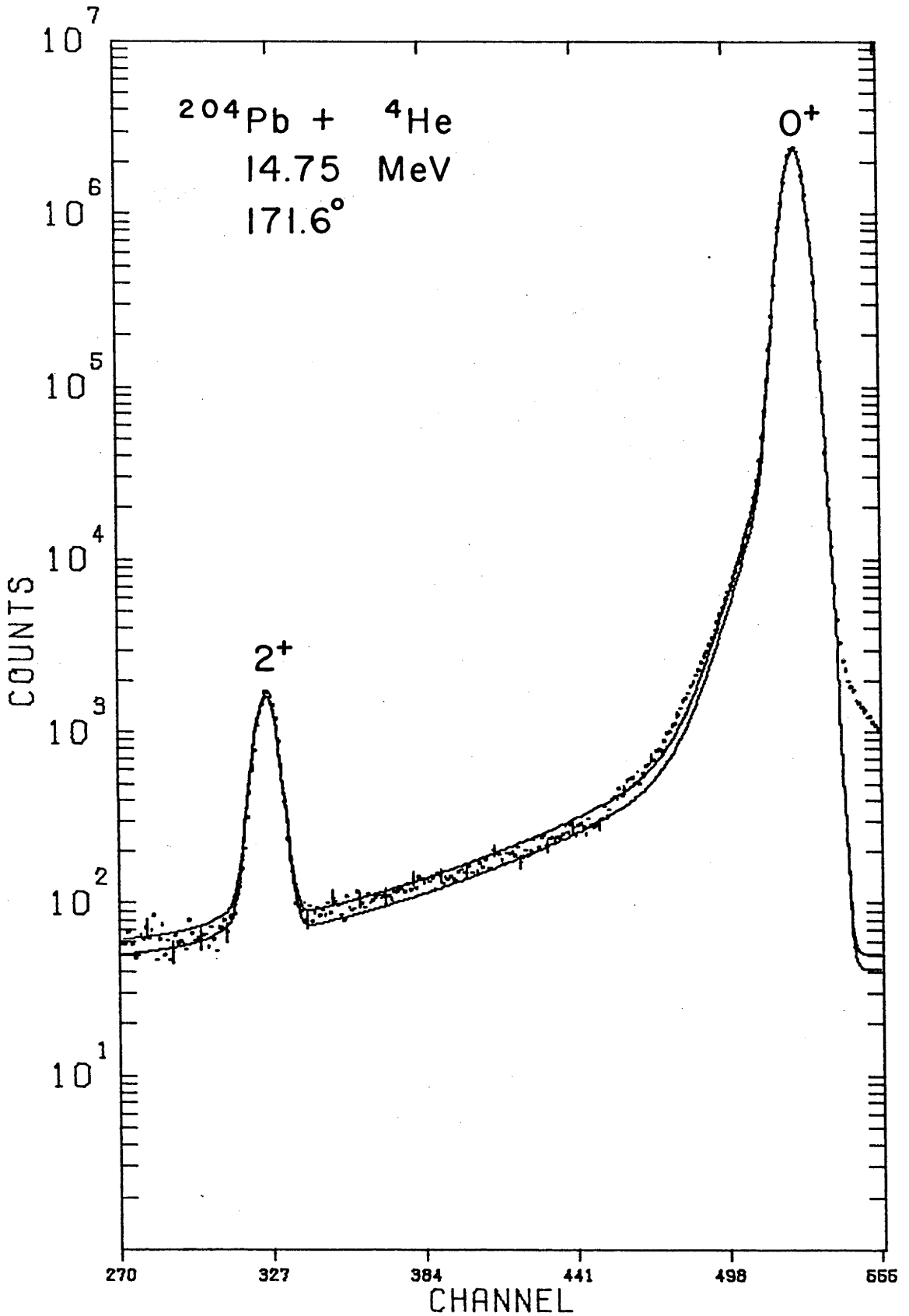

Fig. 4.11 The same spectrum as in fig. 4.9. The full curves show the effect of raising or lowering the elastic peak tail and background by 10%.

as before, by raising and lowering the background until the fit was clearly worse. An example of this procedure is shown in fig. 4.11 for the same spectrum as in fig. 4.9. Uncertainties obtained in this way range from 5% to 15% with 10% being the more usual value. Since on a linear scale the background does not depart greatly from linearity, the background under the inelastic peak was estimated by also performing a linear least squares fit to the data above and below the peak. This method provided an additional check for the exponential fit and the background obtained with the two methods agreed within 5-20%. When statistical uncertainties σ_a are also taken into account, the excitation probabilities, listed in tables 4.4c and 4.5c, are determined with accuracies between 1% and 2%.

In the ^{4}He data, the 3^- state in ^{204}Pb and ^{206}Pb was weakly excited and excitation probabilities for this state have been determined to 7-30% (see tables 4.4c and 4.5c).

4.3.4 Corrections for Isotopic Impurities

Since the elastic peaks of the different lead isotopes present in the targets are not resolved, a correction was applied to the elastic peak area. This correction was based on the abundances quoted by the supplier (these are listed in table 3.3). The reliability of the supplier's assay was checked for ^{204}Pb and ^{206}Pb isotopic impurities; by observing the region of the respective inelastic peaks it was possible to place (at the two standard deviation level) upper limits of 0.4% ^{204}Pb in the target material enriched in ^{206}Pb, and 0.6% ^{206}Pb in the target material enriched in ^{204}Pb. Although the presence of other isotopes could not be checked with the same accuracy, the high degree of enrichment means that the supplier's

assay (specified to an accuracy of better than 0.1%) would need to be in considerable error (say 1%) to affect the results of the present work.

The inelastic peak areas were also corrected for inelastic peaks arising from the other isotopes. Subtraction of inelastic peaks arising from ^{204}Pb or ^{206}Pb contaminants could easily be done from the already measured excitation probabilities (tables 4.4 and 4.5) and from the isotopic abundances (table 3.3). For ^{207}Pb, the only state which can affect the data is the 0.898 MeV $J^{\pi} = 3/2^-$ state which is excited from the $1/2^-$ ground state by an E2 transition. For this level the reduced transition probability has been measured to be $B(E2; 1/2^- \rightarrow 3/2^-) = 0.0121 \pm 0.0005\ e^2b^2$ (Ha72, see also Gr71). Overall, the corrections applied to inelastic peak areas were very small and these are listed in table 4.2.

Table 4.2 Corrections applied to inelastic peak areas due to isotopic impurities. The numbers quoted are percentages of peak area subtracted.

Beam	Target		
	204	206A	206B
^4He	0.004	-	0.0
^{12}C	0.03	-	0.03
^{16}O	0.06	0.12	0.03

Note:- Targets 206A and 206B are explained in table 3.3.

4.3.5 Corrections for Target Thickness and Carbon Layer Thickness

The bombarding energy was corrected for energy loss of incident projectiles in the target and in the thin carbon layer evaporated on the surface of some targets (to prevent evaporation of $PbCl_2$; see subsection 3.2.4). Target thicknesses were obtained by measuring the Pb elastic yield at bombarding energies where Rutherford scattering applies. The chemical form of the target was assumed to be $PbCl_2$, and stopping powers for $PbCl_2$ were obtained from Northcliffe and Schilling (No70). Target thickness corrections applied to the bombarding energies are listed in table 4.3. The possibility of decomposition of the target under bombardment must also be taken into account; if the $PbCl_2$ had completely decomposed to Pb then the target thickness corrections in table 4.3 would need to be reduced by 43% but the resulting effect on excitation probabilities (for ^4He, ^{12}C, and ^{16}O beams) would be at most only 0.08%.

Since only one half of the surface of the target was covered with a thin carbon layer, the thickness of the layer was easily determined by observing the shift in the Pb elastic peak when the covered and uncovered parts of the target were bombarded. The thickness of this layer was typically $2\mu g/cm^2$ and the corresponding bombarding energy corrections are listed in table 4.3.

Table 4.3 Corrections applied to bombarding energy (typical values)

Beam	Target thickness correction (keV)	Carbon thickness correction (keV)	Total (keV)
15 MeV ^4He	4	0	4
46 MeV ^{12}C	15	6	21
60 MeV ^{16}O	20	14	34

Table 4.4 Measured excitation probabilities R_{2+} and R_{3-} for the ^{204}Pb 0.899 MeV 2^+ and 2.634 MeV 3^- states respectively

(a) ^{16}O ions

Bombarding Energy (MeV)	$R_{2+} \times 10^3$	$R_{3-} \times 10^4$
58.955	8.39 ± 0.08	1.26 ± 0.23
59.971	9.20 ± 0.09	1.71 ± 0.19
60.971	10.16 ± 0.10	2.08 ± 0.19
61.956	11.07 ± 0.10	2.48 ± 0.22
61.971	10.91 ± 0.10	2.42 ± 0.22
62.957	11.84 ± 0.13	2.95 ± 0.32
62.957	11.85 ± 0.17	3.33 ± 0.37
62.971	11.61 ± 0.15	3.25 ± 0.36
63.957	12.60 ± 0.11	3.69 ± 0.30
64.958	13.82 ± 0.11	4.00 ± 0.32
66.958	15.58 ± 0.16	5.78 ± 0.52
69.959	18.13 ± 0.15	6.76 ± 0.54
71.960	19.84 ± 0.18	8.01 ± 0.56
74.961	18.79 ± 0.20	4.05 ± 0.53
76.956	14.84 ± 0.67	
76.961	14.79 ± 0.22	
78.968	16.22 ± 0.57	
79.968	32.04 ± 1.35	
84.970	136.6 ± 15.4	

(b) ^{12}C ions

Bombarding Energy (MeV)	$R_{2+} \times 10^3$	$R_{3-} \times 10^4$
44.978	5.49 ± 0.13	1.35 ± 0.22
45.978	6.17 ± 0.15	1.32 ± 0.24
46.979	7.09 ± 0.16	1.35 ± 0.24
47.979	7.64 ± 0.18	2.53 ± 0.33
47.979	7.96 ± 0.07	2.13 ± 0.17
48.979	8.79 ± 0.20	3.53 ± 0.46
49.979	9.87 ± 0.21	3.50 ± 0.46
49.979	9.57 ± 0.08	3.35 ± 0.24
50.980	10.42 ± 0.24	4.33 ± 0.56
51.980	11.40 ± 0.26	5.82 ± 0.70
53.981	12.59 ± 0.28	5.20 ± 0.68
55.981	13.17 ± 0.30	12.3 ± 1.2
59.982	13.37 ± 0.35	

(c) ^{4}He ions

Bombarding Energy (MeV)	$R_{2+} \times 10^4$	$R_{3-} \times 10^5$
13.796	4.24 ± 0.09	
14.447	5.66 ± 0.08	
14.747	6.39 ± 0.10	
15.297	7.72 ± 0.10	1.10 ± 0.20
15.897	9.76 ± 0.16	1.59 ± 0.45
15.897	9.77 ± 0.13	1.71 ± 0.26
16.297	10.71 ± 0.13	2.92 ± 0.29
16.797	12.53 ± 0.14	4.09 ± 0.29
17.497	14.98 ± 0.18	6.71 ± 0.47
17.997	16.52 ± 0.21	7.17 ± 0.50
18.497	18.18 ± 0.28	10.85 ± 0.65

Table 4.5 Measured excitation probabilities R_{2+} and R_{3-} for the ^{206}Pb 0.803 MeV 2^+ and 2.648 MeV 3^- states respectively

(a) ^{16}O ions

Bombarding Energy (MeV)	$R_{2+} \times 10^3$	$R_{3-} \times 10^4$
59.978	6.62 ± 0.09	1.63 ± 0.22
60.979	7.27 ± 0.11	2.01 ± 0.25
61.965	8.09 ± 0.15	2.50 ± 0.18
61.979	7.86 ± 0.17	2.71 ± 0.30
62.965	8.76 ± 0.13	2.70 ± 0.14
62.979	8.37 ± 0.11	2.74 ± 0.27
63.968	9.26 ± 0.09	3.24 ± 0.18
63.968	9.26 ± 0.13	4.05 ± 0.54
64.965	10.17 ± 0.12	3.75 ± 0.21
66.965	11.21 ± 0.19	6.36 ± 0.41
69.967	13.07 ± 0.21	6.45 ± 0.51
71.967	13.86 ± 0.29	6.43 ± 0.59
74.968	11.85 ± 0.27	
76.968	9.54 ± 0.21	
79.969	28.74 ± 0.63	

(b) ^{12}C ions

Bombarding Energy (Mev)	$R_{2+} \times 10^3$	$R_{3-} \times 10^4$
43.978	3.59 ± 0.05	0.79 ± 0.06
45.979	4.61 ± 0.04	1.21 ± 0.10
47.979	5.42 ± 0.13	2.08 ± 0.29
49.979	6.56 ± 0.16	3.50 ± 0.39
51.980	7.53 ± 0.18	3.95 ± 0.47
59.982	10.44 ± 0.43	

(c) ^{4}He ions

Bombarding Energy (MeV)	$R_{2+} \times 10^{4}$	$R_{3-} \times 10^{5}$
13.795	3.32 ± 0.04	
14.445	4.29 ± 0.05	
14.745	4.73 ± 0.05	
15.295	5.78 ± 0.09	0.99 ± 0.22
15.895	6.60 ± 0.09	1.62 ± 0.16
15.896	6.84 ± 0.07	1.68 ± 0.21
16.296	7.69 ± 0.11	1.81 ± 0.35
16.796	8.56 ± 0.15	3.48 ± 0.47
17.496	9.87 ± 0.15	5.65 ± 0.67
17.996	12.07 ± 0.21	10.39 ± 1.12
18.496	11.10 ± 0.17	7.33 ± 1.08

4.4 The ^{208}Pb Experiment

Data reduction in the ^{208}Pb experiment was similar to that for ^{204}Pb and ^{206}Pb. However because of the higher excitation energy of the 3^- state, the higher multipolarity of the transition, and the lower safe energies (see chapter 5), the excitation probabilities were much lower and this gave rise to difficulties not encountered in the ^{204}Pb and ^{206}Pb experiments. On the other hand, the higher excitation energy of the 3^- state (compared to ^{204,206}Pb) increased the size of the reorientation effect to 20% per beam (see eq. (2.23)).

4.4.1 The ^{16}O Data

An example of data obtained with a 60 MeV ^{16}O beam is shown in fig. 4.12. It can be seen that the single nucleon transfer peaks from the reactions ^{208}Pb(^{16}O,^{17}O)^{207}Pb and ^{208}Pb(^{16}O,^{15}N)^{209}Bi are well below the 3^- inelastic peak and so do not present a problem for the extraction of the 3^- peak area. Although the 3^- peak is well separated from the elastic peak, the excitation probability is so low that the elastic peak tail is still very significant (peak-to-valley ratios were 4:1 at 59 MeV and 8:1 at 60 MeV and at 61 MeV). The lineshape fitting program described in section 4.1 was used to estimate the elastic tail area underneath the 3^- peak, and the peak areas were determined according to the procedure outlined in section 4.2. The systematic uncertainty σ_b in the elastic peak tail height was estimated, as before (section 4.3.1), by observing the effect of raising and lowering the elastic tail, and ranges between 6% and 15%; the resulting uncertainty in the inelastic peak area is about 3.5%. When statistical uncertainties in the elastic and 3^- peaks are

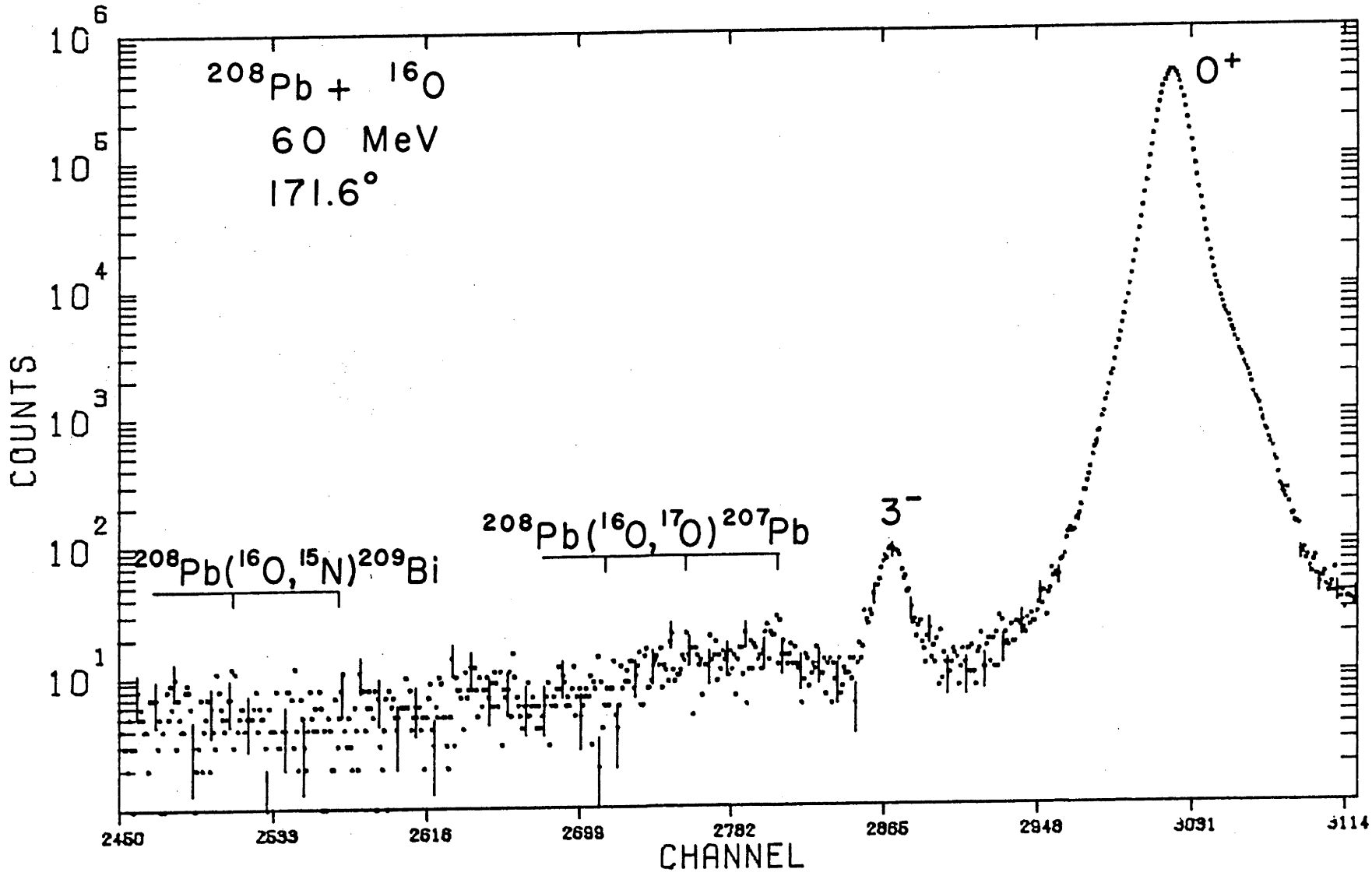

Fig. 4.12 Spectrum of 60 MeV ^{16}O projectiles backscattered from ^{208}Pb. Single nucleon transfer peaks are indicated.

included, the accuracy of the measured excitation probabilities is about 4.5%; this relatively large value is in spite of the long data accumulation times involved (56 hrs for the worst case). In the case of data taken above 61 MeV, data accumulation times were much shorter but the uncertainties in the excitation probabilities are about 10%.

Isotopic impurities in the target are listed in table 3.3 and these were subtracted from the elastic peak. The area of the inelastic peak was corrected for peaks, arising from the 2.624 MeV $5/2^+$ and 2.662 MeV $7/2^+$ states in ^{207}Pb and from the 2.648 MeV 3^- state in ^{206}Pb, located underneath. The corrections for the ^{207}Pb inelastic peaks were applied using the B(E3) values measured by Häusser et al. (Hä72) and corrections for ^{206}Pb used the B(E3) measured in the present work (Table 5.1). The total effect of these corrections was to reduce the 3^- peak area by 0.6%. The inelastic peak from the 2.634 MeV 3^- level in ^{204}Pb was located outside the summation range for the ^{208}Pb 3^- peak and no correction for it was applied.

The target thickness ($PbCl_2$) was measured (as described in subsection 4.3.5) as 18 $\mu g/cm^2$, and the carbon layer thickness was 0.2 $\mu g/cm^2$. The total correction to the bombarding energy, due to target thickness, was 22 keV; if the $PbCl_2$ target had completely decomposed to Pb (see subsection 4.3.5) this correction would need to be reduced by 43% and the resulting effect on the excitation probability would be 0.23%. The measured excitation probabilities are listed in table 4.6.

4.4.2 The ^{4}He Data

Excitation probabilities for this data are lower than in the ^{204}Pb and ^{206}Pb experiments by a factor of about 50. Data collection times were about 100 hrs and even then the 3^- peak contained only about 1600 counts. An example of data obtained at 15.3 MeV is shown in figs. 4.13 and 4.14. The peak labelled "^{28}Si" corresponds to ^{4}He ions elastically scattered from ^{208}Pb in the target then inducing the reaction ^{28}Si(^{4}He,^{4}He)^{28}Si*(1.78 MeV) in the detector silicon, with the de-excitation gamma-ray escaping from the detector (for a description of this effect see Kraushaar et al. (Kr67)). The unlabelled arrows indicate the position of similar peaks arising from ^{29}Si and ^{30}Si in the detector. In this data, the 3^- peak was sufficiently well separated from the elastic peak that the elastic tail no longer contributed to the background. However, a large fraction of the background in the region of the 3^- peak was produced by pulse pile-up. A peak, due to particles scattered from ^{12}C and ^{35}Cl in the target and arriving simultaneously at the detector, was clearly observed between the "^{28}Si" peak and the elastic peak, and this pile-up produced a tail which extended below the 3^- peak. A peak produced by triple pulse pile-up arising from elastic scattering from ^{12}C was observed just below the 3^- peak and this restricted the number of channels which could be used to estimate the background height on the low energy side of the 3^- peak. The cross-section at backward angles for elastic scattering of ^{4}He ions by ^{12}C appears to have a minimum near 15.2 MeV (Ca64) and this was confirmed by measuring an excitation function. In view of this, and because on the basis of the optical model calculations of Feng et al. (Fe76) the maximum

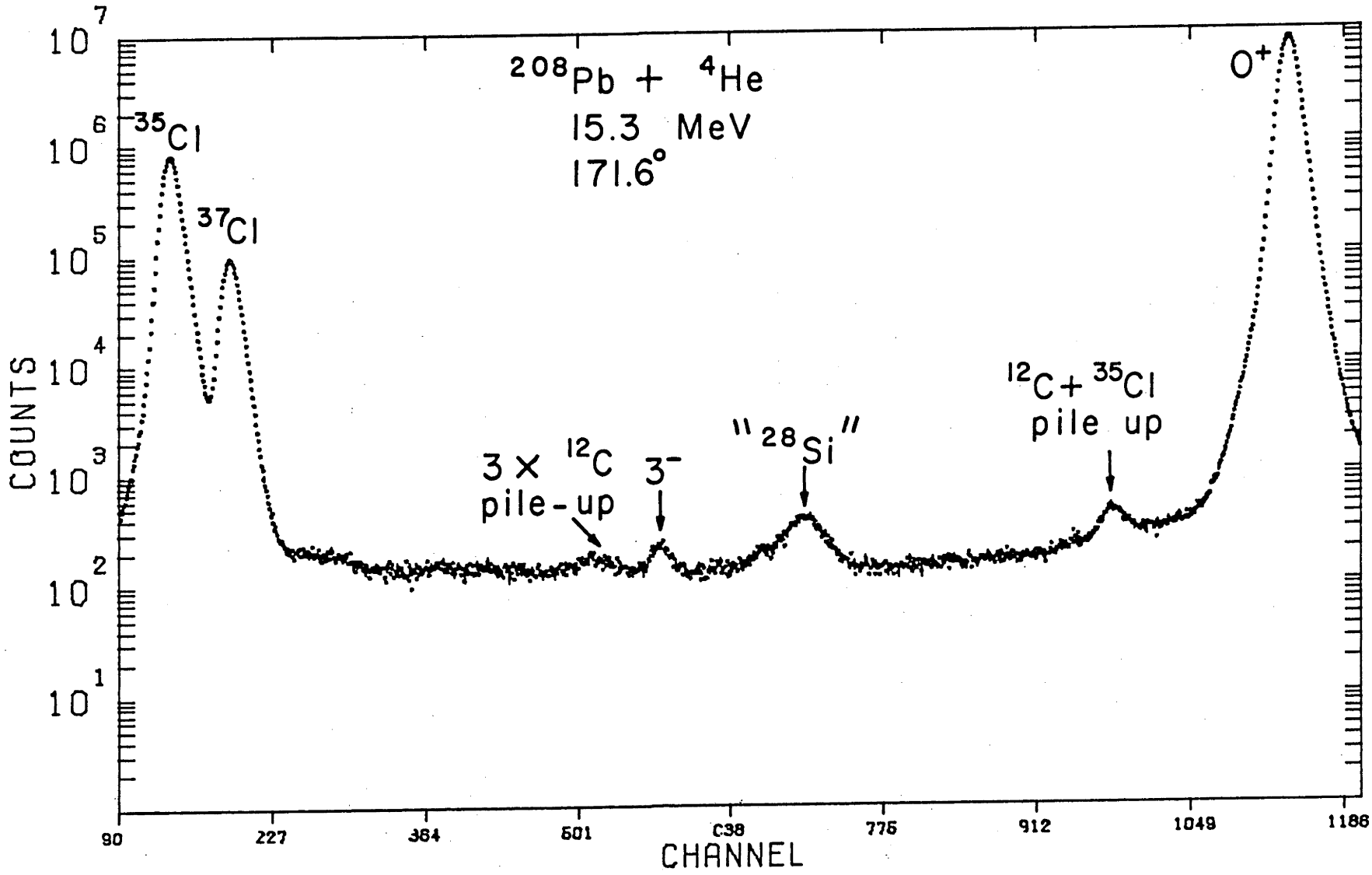

Fig. 4.13 Spectrum of 15.3 MeV ^{4}He projectiles backscattered from ^{208}Pb. Peaks due to pulse pile-up are indicated in addition to the "^{28}Si" peak and the 3^- inelastic peak.

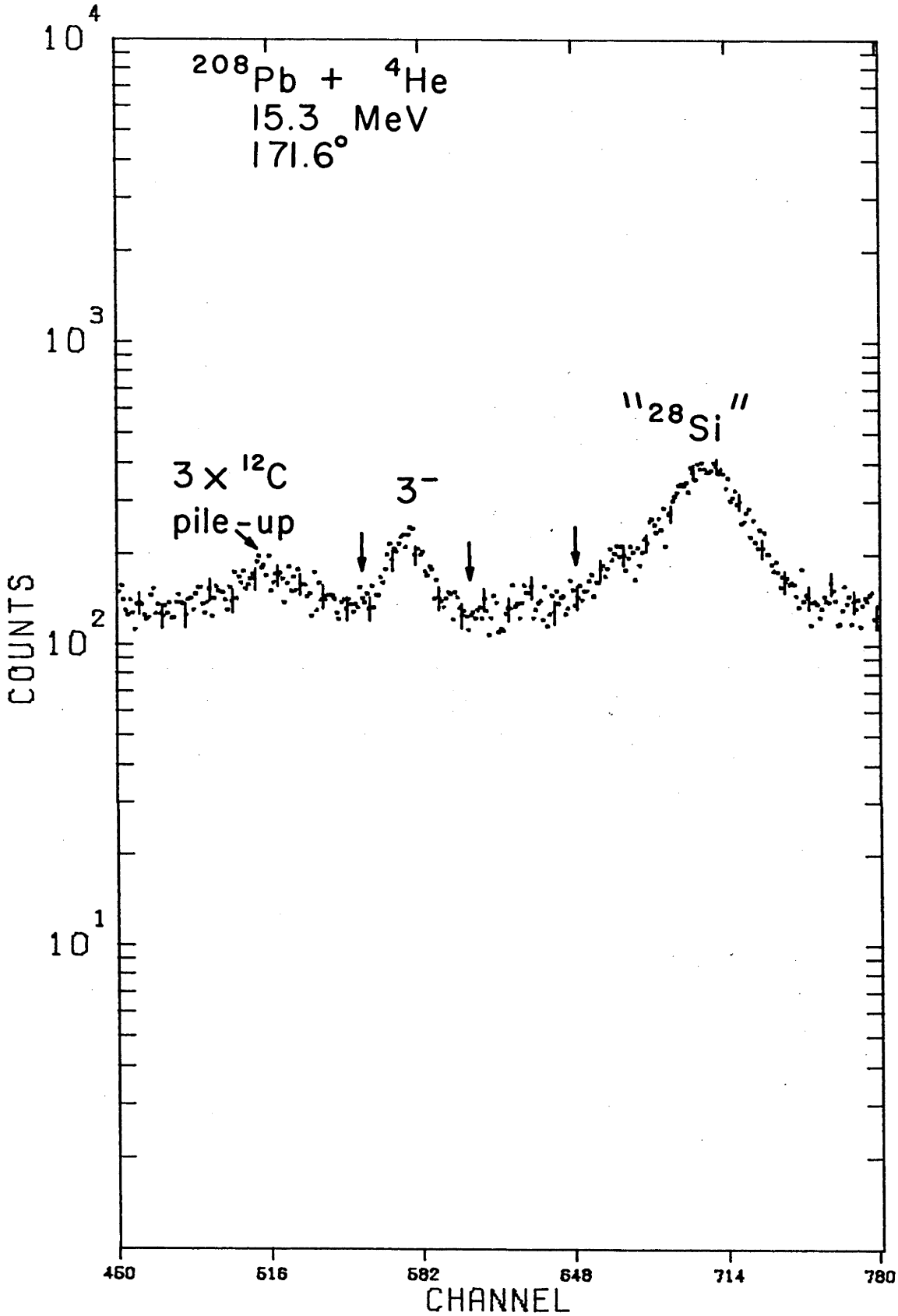

Fig. 4.14 Expanded view of the region near the 3^- inelastic peak for the same data as in fig. 4.13.

safe energy is expected to be near 15.3 MeV (this is discussed further in chapter 5), the data were collected at 15.1 MeV and 15.3 MeV. Pile-up rejection circuitry was employed and this effectively reduced the pile-up background, although the pile-up peaks themselves could not be removed. The carbon backings in the targets were made as thin as possible ($\approx$ 10 $\mu g/cm^2$). However, even with these precautions, the peak-to-valley ratios obtained were 1.4:1 at 15.1 MeV and 1.8:1 for the two spectra obtained at 15.3 MeV.

The area of the 3^- peak was obtained by interpolating a linear background underneath. The height of this background was determined by a least squares fit to the data on either side of the peak. Since the choice of data region used in calculating the background would affect the background height and hence the peak area obtained, least squares fits were made to several different data regions on either side of the peak. At the one standard deviation level, the 3^- peak areas obtained were within 2.5% of that obtained using what was judged to be the most reasonable background. The small size of the 3^- peak and the relatively high background combine to give larger uncertainties than in the ^{16}O data. The overall uncertainties in the measured excitation probabilities are 5.6% and 8.2% for the two 15.3 MeV spectra obtained, and 7.9% for the 15.1 MeV spectrum.

Corrections for isotopic impurities (abundances are listed in table 3.3) were applied to the elastic peak area. The inelastic peak area was corrected for inelastic peaks arising from the excited states in ^{206}Pb and ^{207}Pb mentioned in subsection 4.4.1. In this case, it was also necessary to correct for the inelastic peak due to the 2.634 MeV 3^- state in ^{204}Pb and the B(E3) measured in the present work (table 5.1) were used. The total of these corrections

was 0.6% of the 3^- peak area. Measured target thicknesses were found to be 97 $\mu g/cm^2$ and 121 $\mu g/cm^2$ and the carbon layer thickness was 1-2 $\mu g/cm^2$. The resulting corrections to the bombarding energies were 8 keV and 10 keV respectively; if the $PbCl_2$ targets had completely decomposed to Pb the thickness corrections would need to be reduced by 43% with a corresponding 0.40% effect on the excitation probability. The measured excitation probabilities are listed in table 4.6.

Table 4.6 Measured excitation probabilities R_{exp} for the 2.615 MeV 3^- state of ^{208}Pb

Beam	Bombarding Energy (MeV)	$R_{exp} \times 10^5$
^4He	15.092	1.028 ± 0.081
	15.290	1.270 ± 0.071
	15.290	1.147 ± 0.094
^{16}O	58.978	14.36 ± 0.62
	59.978	18.43 ± 0.88
	60.978	21.29 ± 0.90
	61.978	26.8 ± 3.7
	62.978	30.7 ± 3.0
	63.978	41.0 ± 3.8

CHAPTER 5

DATA ANALYSIS AND RESULTS

The measured excitation probabilities obtained in chapter 4 from the raw data, are analysed in the present chapter to obtain results for the reduced excitation probabilities $B(E\lambda)$ and quadrupole moments Q_{J^π}. As before, the ^{204}Pb and ^{206}Pb experiments are discussed together and the ^{208}Pb experiment, where in some cases the analysis had to be modified, is treated separately. The method used to obtain values of $B(E\lambda)$ and Q_{J^π} from the excitation probabilities is described in section 5.3. However, before the data are analysed assuming pure Coulomb excitation, it is important to show that the data used in the analysis are free from Coulomb-nuclear interference effects.

5.1 Safe Bombarding Energies

In order to analyse the results in terms of pure Coulomb excitation theory (chapter 2) it was essential to determine the maximum "safe" bombarding energy (or equivalently the minimum "safe" distance of separation of the nuclear surfaces) at which the effects of the nuclear force can be neglected.

The process of Coulomb-nuclear interference in inelastic scattering may be understood, in general, by considering the Coulomb and nuclear excitation amplitudes. Fig. 5.1 shows the variation of the Coulomb amplitude a_c and the real and imaginary nuclear amplitudes a_N^R and a_N^I as a function of the distance D between the centres of the two nuclei. The amplitudes a_c and a_N^R are of opposite sign because the Coulomb potential is repulsive while the nuclear potential is attractive (a_N^I has the same sign as a_N^R and is generally much smaller). The total excitation amplitude may be written as

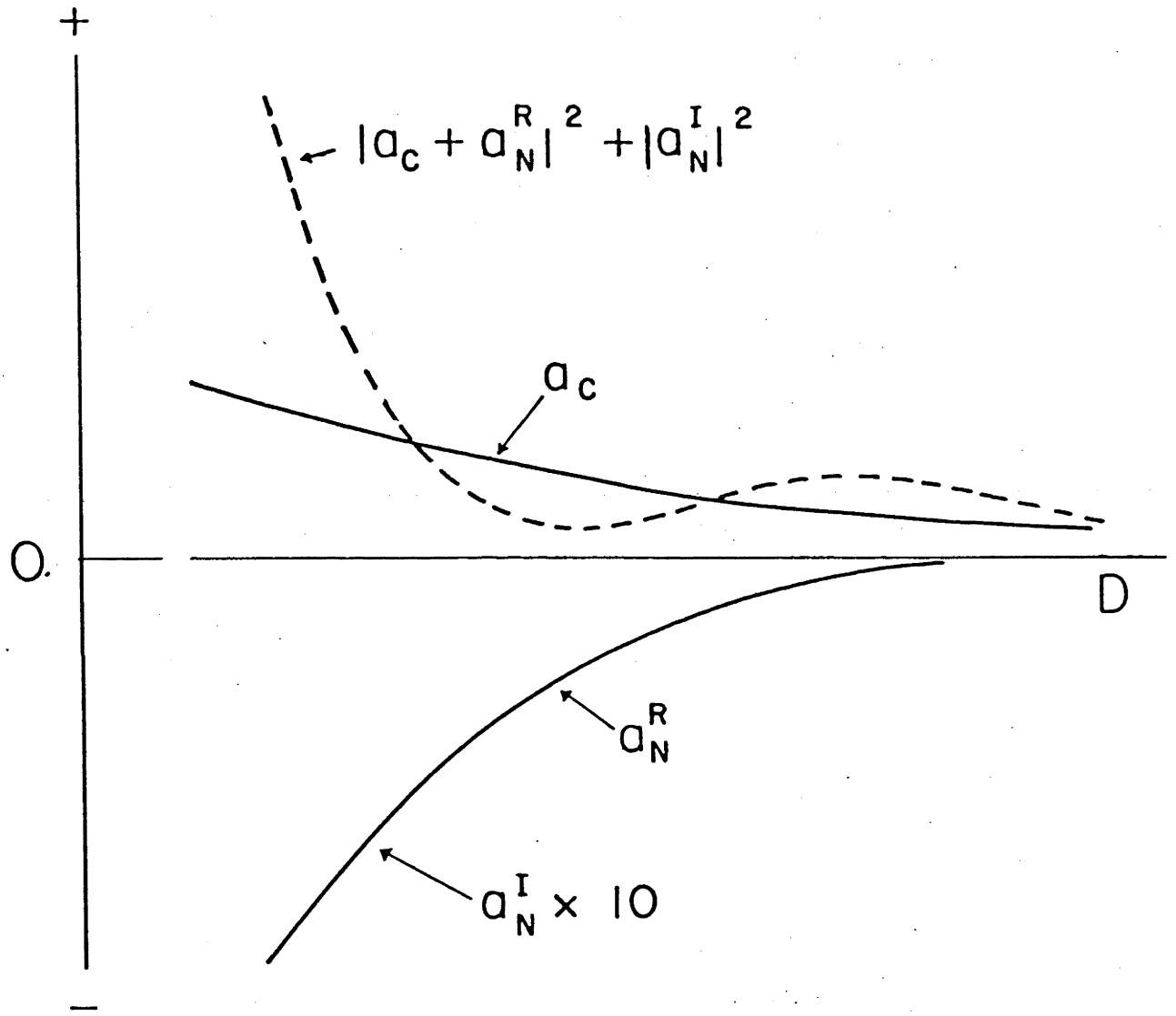

Fig. 5.1 Amplitudes a_c, a_N^R, a_N^I, and excitation probability eq. (5.2) as a function of the distance D between the centres of two nuclei (from Po76).

$$\left(a_c + a_N^R\right) + i\, a_N^I \,, \tag{5.1}$$

and the excitation probability (for a particular magnetic substate) is proportional to

$$\left|a_c + a_N^R\right|^2 + \left(a_N^I\right)^2 \,. \tag{5.2}$$

Since the Coulomb force is long range while the nuclear force is short range, at large distances D the Coulomb interaction dominates. As D decreases, a point is reached where a_c and a_N^R have similar magnitudes; they interfere destructively to give a minimum in the excitation probability. At yet smaller values of D, a_N^R dominates a_c. The observed excitation probability does not go through a sharp minimum because the excitation probabilities for different magnetic substates do not reach their minimum at the same D, and because of the contribution from $\left(a_N^I\right)^2$.

In the present work, safe energies were determined for both ^{204}Pb and ^{206}Pb and for each of the projectiles ^{4}He, ^{12}C, and ^{16}O, by observing for the 2^+ state the behaviour of the double ratio R_{exp}/R_{comp} as the bombarding energy was increased; here R_{comp} is the excitation probability of the 2^+ state assuming pure Coulomb excitation. Compared to looking for deviations from Rutherford scattering, studying R_{exp}/R_{comp} has the advantage of being independent of any normalisation (e.g. beam current integration, target thickness) and is more relevant to the present work since R_{exp} was used to determine $Q_{J\pi}$. Values obtained for R_{exp}/R_{comp} are plotted in figs. 5.2 and 5.3 as a function of the separation S between the two nuclear surfaces; S is defined by

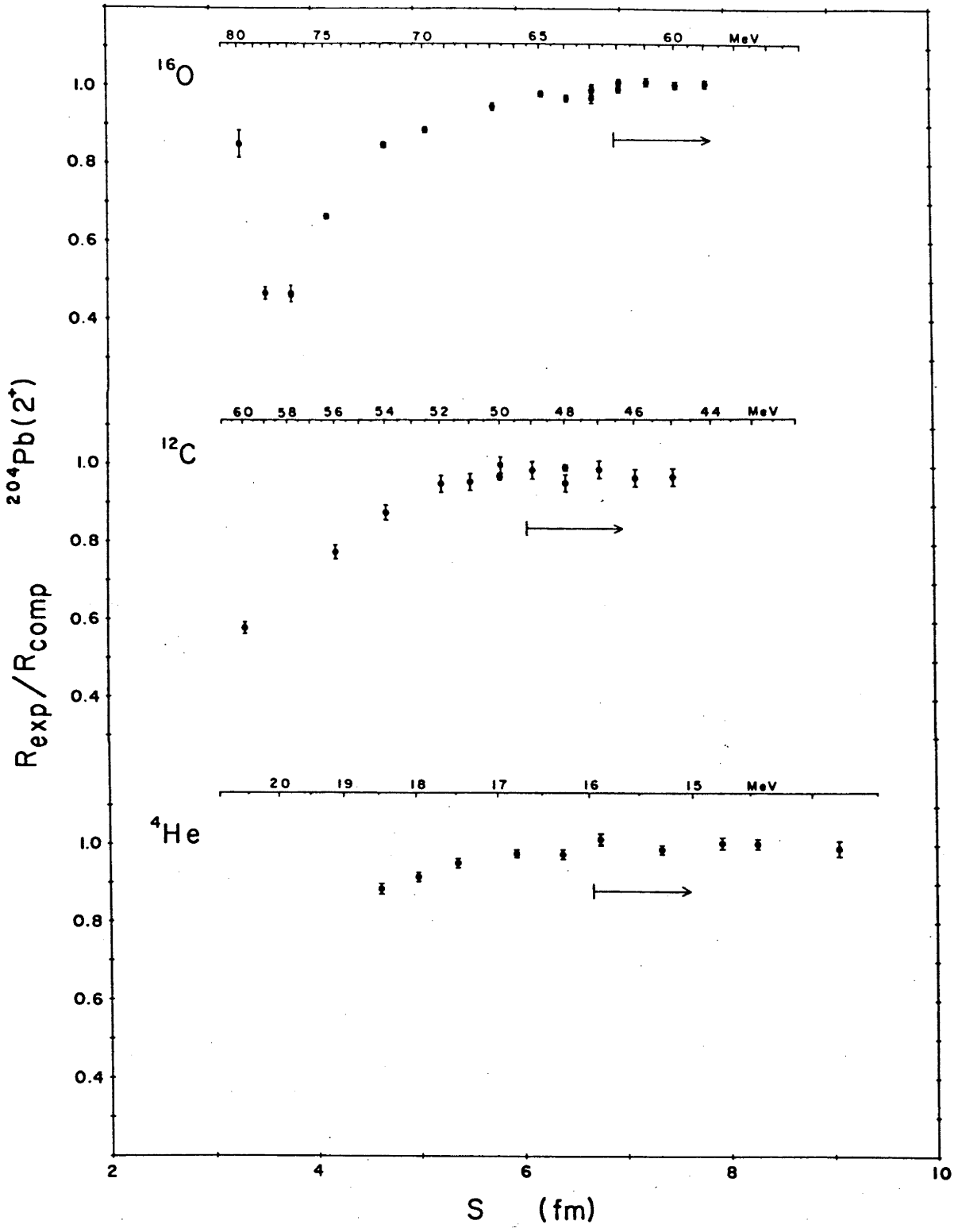

Fig. 5.2 The double ratio R_{exp}/R_{comp} for $^{204}Pb\ (2^+)$ as a function of the distance of separation S (eq. (5.3)). The unlabelled arrows indicate adopted safe energies.

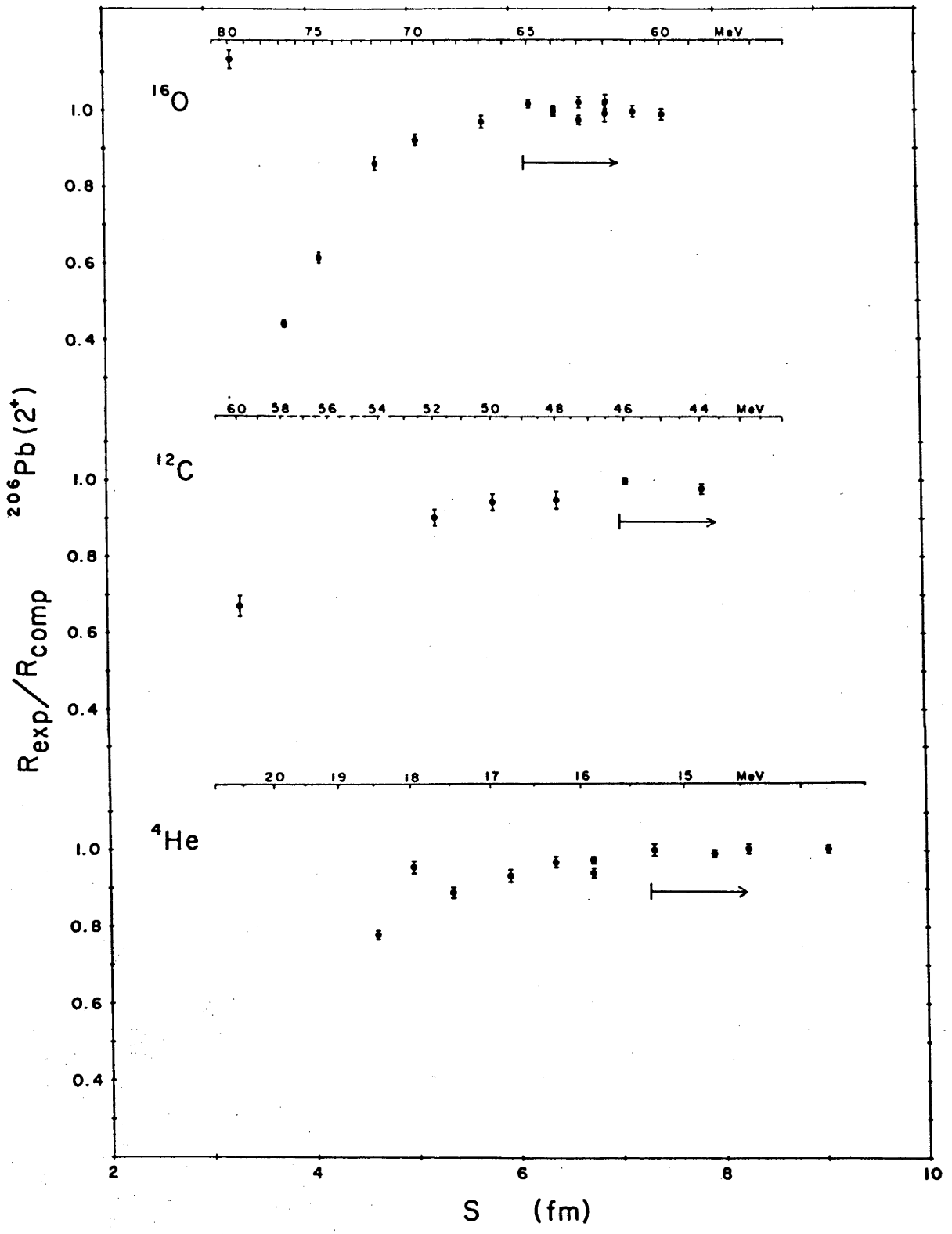

Fig. 5.3 The double ratio R_{exp}/R_{comp} for ^{206}Pb (2^{+}) as a function of the distance of separation S (eq. (5.3)). The unlabelled arrows indicate adopted safe energies.

$$S = 0.72 \frac{Z_1 Z_2 (A_1 + A_2)}{E_{lab} A_2} (1 + \mathrm{Cosec}(\theta/2)) - 1.128 \, (A_1^{1/3} + A_2^{1/3}) \text{ fm} \qquad (5.3)$$

where the subscripts 1 and 2 refer to the projectile and the target nucleus respectively, E_{lab} is in MeV, and θ is the scattering angle in the centre of mass. The equivalent sharp radius (ESR), equal to $1.128 A^{1/3}$ fm and described by Myers (My73), is used here (rather than the more common $1.25 A^{1/3}$ fm) so that comparison can be made with the results of Feng et al. (Fe76) who used the distorted-wave Born approximation (DWBA) method to calculate nuclear interference effects.

A striking feature of the data in figs. 5.2 and 5.3 is the pronounced depth of the Coulomb-nuclear interference minimum. It appears that the net effect of this strong interference is to lower the maximum safe energy. Since the excitation probabilities in the ^{204}Pb and ^{206}Pb experiments were determined to about 1%, the safe energies are taken to be those for which the excitation probability deviates by less than 1% from that for pure Coulomb excitation; in the ^{208}Pb experiment the uncertainties in the excitation probabilities were much larger (5.6 - 8.2% for ^{4}He, and 4.5% for ^{16}O) and these set the lower limit on the size of deviations, from pure Coulomb excitation, which could be detected. The different values between projectiles obtained for the safe distance (indicated in figs. 5.2 and 5.3) may be due in part to the conservative approach adopted in determining safe energies. There appears to be no consistent trend between the different projectiles and the two lead isotopes. The mean value of the safe distance for all projectile-target combinations is 6.7 fm. This result agrees with the value of 6.6 fm (or equivalently 5.5 fm taking the nuclear radius to be $1.25 A^{1/3}$ fm) obtained by Olin et al.

(0174) for ^{32}S scattering from $^{204,206}Pb$. The present result also compares well with the calculations of Feng et al. who, for ^{4}He inelastic scattering, predict a 1% deviation from the pure Coulomb cross section at 6.7 fm for ^{152}Sm and at 6.5 fm for ^{234}U.

5.2 The First 3^- State in ^{204}Pb and ^{206}Pb

The 3^- state near 2.6 MeV in $^{204,206}Pb$ has been observed in data obtained over a wide range of bombarding energies (see chapter 4). This state is of interest because from the excitation probabilities obtained at different bombarding energies, information may be gained regarding safe energies to be used in the ^{208}Pb experiment. (The excitation of the 3^- state in $^{204,206}Pb$ consists mainly of direct E3 excitation from the ground state; multiple excitations of the type $0^+ \rightarrow 2^+ \rightarrow 3^-$ are comparatively small. The assumption that the maximum safe energies for the 3^- state in $^{204,206,208}Pb$ are the same, is supported in part by the results for the 2^+ state in $^{204,206}Pb$.) As for the 2^+ state, the double ratio R_{exp}/R_{comp} is plotted as a function of bombarding energy (figs. 5.4 and 5.5). However, the large error bars on the data makes the identification of safe energies difficult. For ^{16}O, there is a definite decrease in R_{exp}/R_{comp} at energies above 63 MeV, and it appears that below 61 MeV R_{exp}/R_{comp} assumes a constant value; one may then take the maximum safe distance to be 7.2 fm. For ^{4}He, R_{exp}/R_{comp} appears to be slowly increasing even down to the lowest energy; no data is available below 15.3 MeV since at those energies the 3^- peak in the spectrum was indistinguishable from the background.

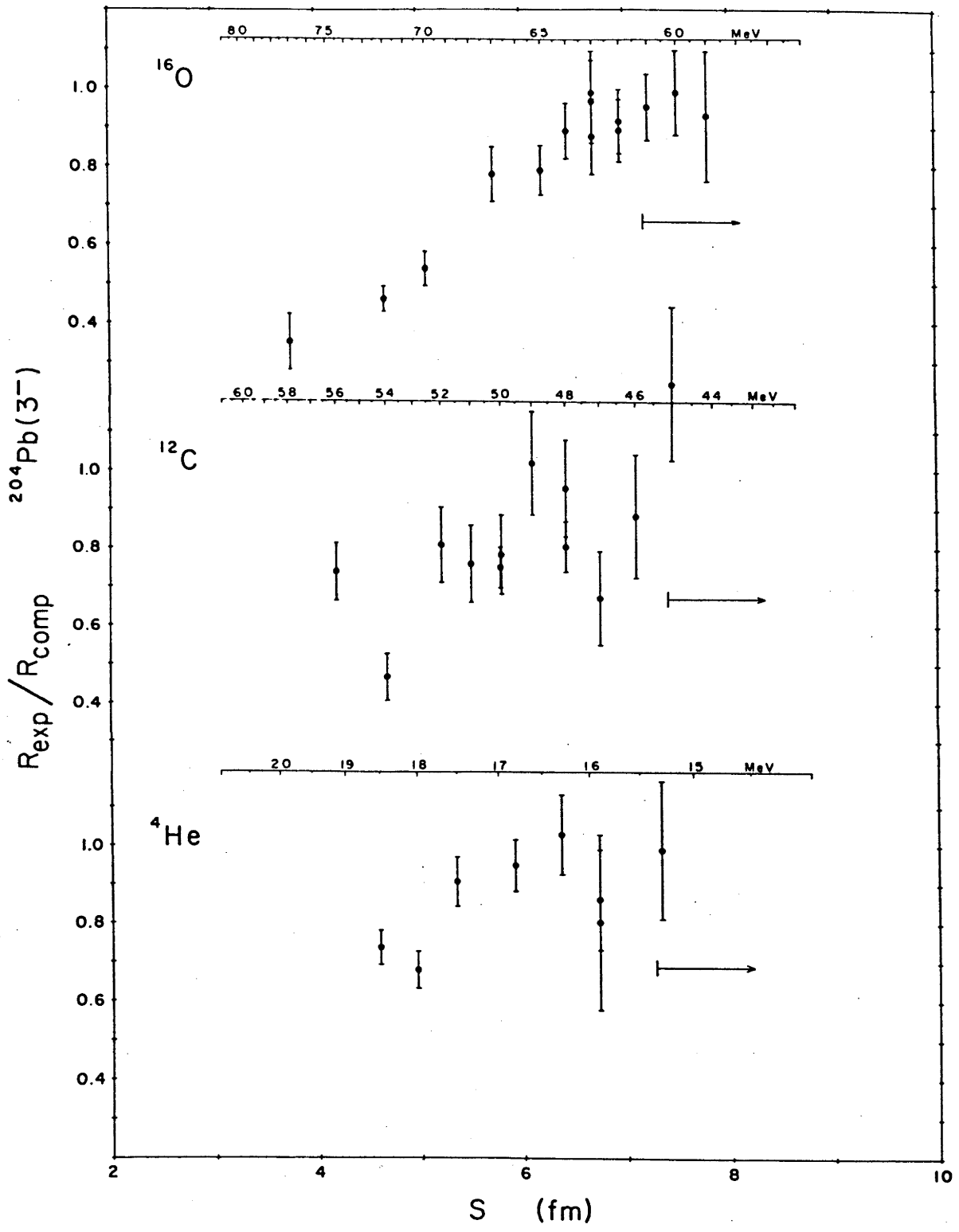

Fig. 5.4 The double ratio R_{exp}/R_{comp} for ^{204}Pb (3^-) as a function of the distance of separation S (eq. (5.3)). The unlabelled arrows indicate adopted safe energies.

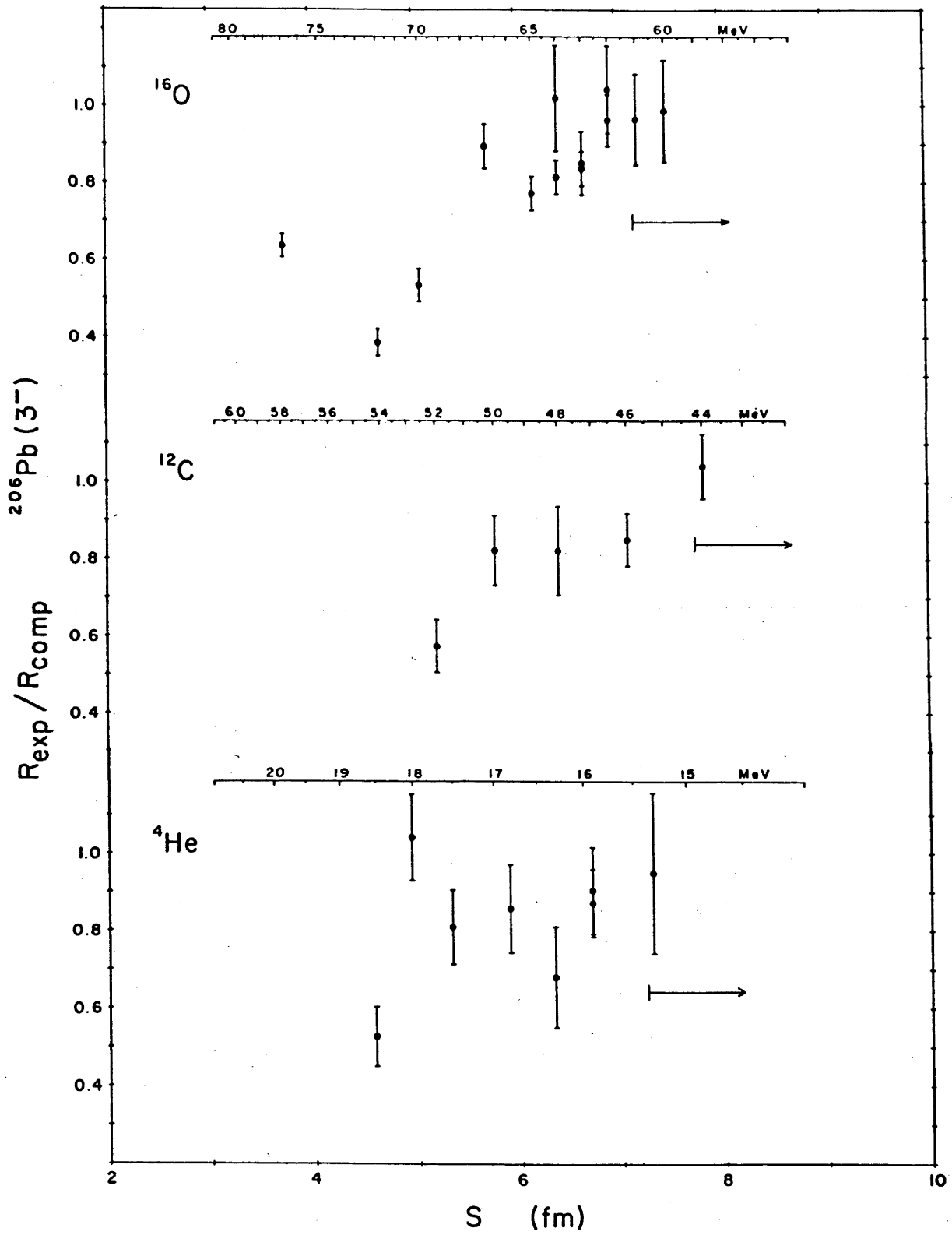

Fig. 5.5 The double ratio R_{exp}/R_{comp} for ^{206}Pb (3^-) as a function of the distance of separation S (eq. (5.3)). The unlabelled arrows indicate adopted safe energies.

One can only conclude that the maximum safe distance for ^{4}He is at least 7.3 fm, this being consistent with the value 7.4 fm calculated by Feng et al. for ^{208}Pb. Although the present data are insufficient to validate Feng's prediction that the safe distance should increase as the multipolarity of the excitation increases, they do indicate that the safe distances for E3 excitation are greater than those for E2 excitation.

The reduced transition probability $B(E3; 0^+ \rightarrow 3^-)$ can be obtained from (see eq. (2.16)),

$$B(E3; 0^+ \rightarrow 3^-) = R_{exp}/F(\theta,\xi) \qquad (5.4)$$

where R_{exp} refers to the excitation probabilities listed in tables 4.4 and 4.5, and $F(\theta,\xi)$ is obtained from the de Boer-Winther program (see section 2.3). The results obtained, using ^{4}He, ^{12}C, and ^{16}O data taken at safe energies (a safe distance of 7.3 fm was assumed for ^{12}C), are listed in table 5.1 and agree with values from other experiments. It must be noted that these results are calculated neglecting second

Table 5.1 Measured $B(E3; 0^+ \rightarrow 3^-)$ values for the 2.6 MeV 3^- state in ^{204}Pb and ^{206}Pb

Nucleus	$B(E3; 0^+ \rightarrow 3^-)$ (e^2b^3)	Method	Reference
^{204}Pb	0.609 ± 0.035		this work
	0.618 ± 0.097	(α,α') inelastic scattering	A167
^{206}Pb	0.605 ± 0.035		this work
	0.50 ± 0.03	Coulomb excitation, thick target yield	Ha72
	0.66 ± 0.07	Coulomb excitation, thick target yield	Gr71
	0.64 ± 0.04	(e,e')	Zi68
	0.722 ± 0.095	(α,α') inelastic scattering	A167

order effects; it is estimated that a quadrupole moment of -0.42 eb (as in ^{208}Pb) would increase the B(E3) (for both ^{204}Pb and ^{206}Pb), by about 0.044 e^2b^3, and the effect of multiple excitation via the 2^+ state (using matrix elements in section 5.4) would change the B(E3) by $\pm$ 0.001 e^2b^3 (depending on the sign of the interference).

5.3 Extraction of B(Eλ) and $Q_{J\pi}$ from the Data

In principle, the Coulomb excitation analysis can be carried out with the de Boer-Winther program by fitting the computed excitation probabilities R_{comp} to the experimental values R_{exp}, letting the B(Eλ) and $Q_{J\pi}$ vary as free parameters. However, the analysis can be made considerably simpler and faster by expressing the excitation probabilities, on the basis of eq. (2.24), as

$$R_{comp}(Q_{J\pi}) = F\ B(E\lambda)\ [1 + \rho\ Q_{J\pi}] \tag{5.5}$$

where F and ρ are functions whose values depend on the projectile and the bombarding energy (in the present work the scattering angle was kept constant). It is convenient to rearrange eq. (5.5) in the form

$$R_{comp}/F = B(E\lambda) + [B(E\lambda)Q_{J\pi}]\ \rho\ , \tag{5.6}$$

which is linear in ρ. If R_{comp}/F is plotted against ρ, then eq. (5.6) represents a straight line whose intercept on the vertical axis is equal to B(Eλ) and whose slope is equal to the product $B(E\lambda)Q_{J\pi}$. Experimental values of $Q_{J\pi}$ and B(Eλ) can therefore be determined by expressing the experimental excitation probabilities in the form R_{exp}/F and performing a linear least-squares fit.

The values of functions F and ρ are obtained from

$$F = R_{comp}(0)/B(E\lambda) \tag{5.7}$$

and

$$\rho = [R_{comp}(Q_{J\pi})/R_{comp}(0) - 1]/Q_{J\pi} \tag{5.8}$$

with $R_{comp}(0)$ and $R_{comp}(Q_{J\pi})$ computed, at each energy and for each projectile, with the de Boer-Winther program using estimated values of $B(E\lambda)$ and $Q_{J\pi}$. If the estimated $Q_{J\pi}$ and $B(E\lambda)$ values differed significantly from the ones obtained after a fit to the experimental data, F and ρ were recomputed using the values of $B(E\lambda)$ and $Q_{J\pi}$ obtained on the first iteration. It must be emphasized that although the parametrization in eq. (5.5) is similar to the perturbation expansion (eq. (2.24)),this does not imply that perturbation theory is being used, since both F and ρ can contain contributions from higher order processes.

The method of linear least squares, described in detail by Bevington (Be69), gives analytical expressions for direct evaluation of uncertainties in the intercept and the slope of the fitted line. The uncertainty in $B(E\lambda)$ is equal to the uncertainty in the intercept and the uncertainty in $Q_{J\pi}$ is calculated from

$$\Delta Q_{J\pi} = Q_{J\pi} \left[(\Delta\text{slope}/\text{slope})^2 + (\Delta B(E\lambda)/B(E\lambda))^2\right]^{\frac{1}{2}} . \tag{5.9}$$

In the present analysis, each data point was weighted by a factor $1/\sigma_i^2$, where σ_i is the statistical error in the i^{th} value of R_{exp}/F. The goodness of the fit was determined from the chi-square test by evaluating

$$\chi^2 = \frac{1}{N-2} \sum_i \left[\frac{y_i(\text{exp.}) - y_i(\text{fit})}{\sigma_i}\right]^2 \tag{5.10}$$

where $y = R/F$ and N is the number of data points. For a good fit $\chi^2 \approx 1$.

5.4 Results for Q_{2+} and B(E2) in ^{204}Pb and ^{206}Pb

Following the above procedure, and using experimental excitation probabilities (tables 4.4 and 4.5) at safe bombarding energies (indicated in figs. 5.2 and 5.3), the partially corrected results obtained are $B(E2; 0^+ \rightarrow 2^+) = 0.1665 \pm 0.0017\ e^2b^2$ and $Q_{2+} = +0.213 \pm 0.076$ eb for ^{204}Pb, and $B(E2; 0^+ \rightarrow 2^+) = 0.1030 \pm 0.0009\ e^2b^2$ and $Q_{2+} = +0.033 \pm 0.079$ eb for ^{206}Pb (uncertainties will be discussed in subsection 5.4.7). Fits to the data are shown in figs. 5.6 and 5.7 for ^{204}Pb and ^{206}Pb respectively. In the above results only two states (the ground state and the first 2^+ state) are considered in the de Boer-Winther program, but electron screening, vacuum polarization, and quantal corrections (see subsections 2.2.6 and 2.2.7) are included together with the effect of the giant dipole resonance. Processes affecting the results, including interference from higher states, are discussed separately below (with particular emphasis on their effect on Q_{2+}). A summary of these effects on the values of Q_{2+} and B(E2) is given in table 5.2.

5.4.1 Electron Screening and Vacuum Polarization Corrections

These corrections were treated by making small changes to the bombarding energy (see table 2.2). Since the signs of these corrections are opposite, the combined correction for electron screening and vacuum polarization is very small. Changes in the magnitude of Q_{2+} are $\Delta|Q_{2+}| = +0.003$ eb for ^{204}Pb and $\Delta|Q_{+}| = +0.004$ eb for ^{206}Pb.

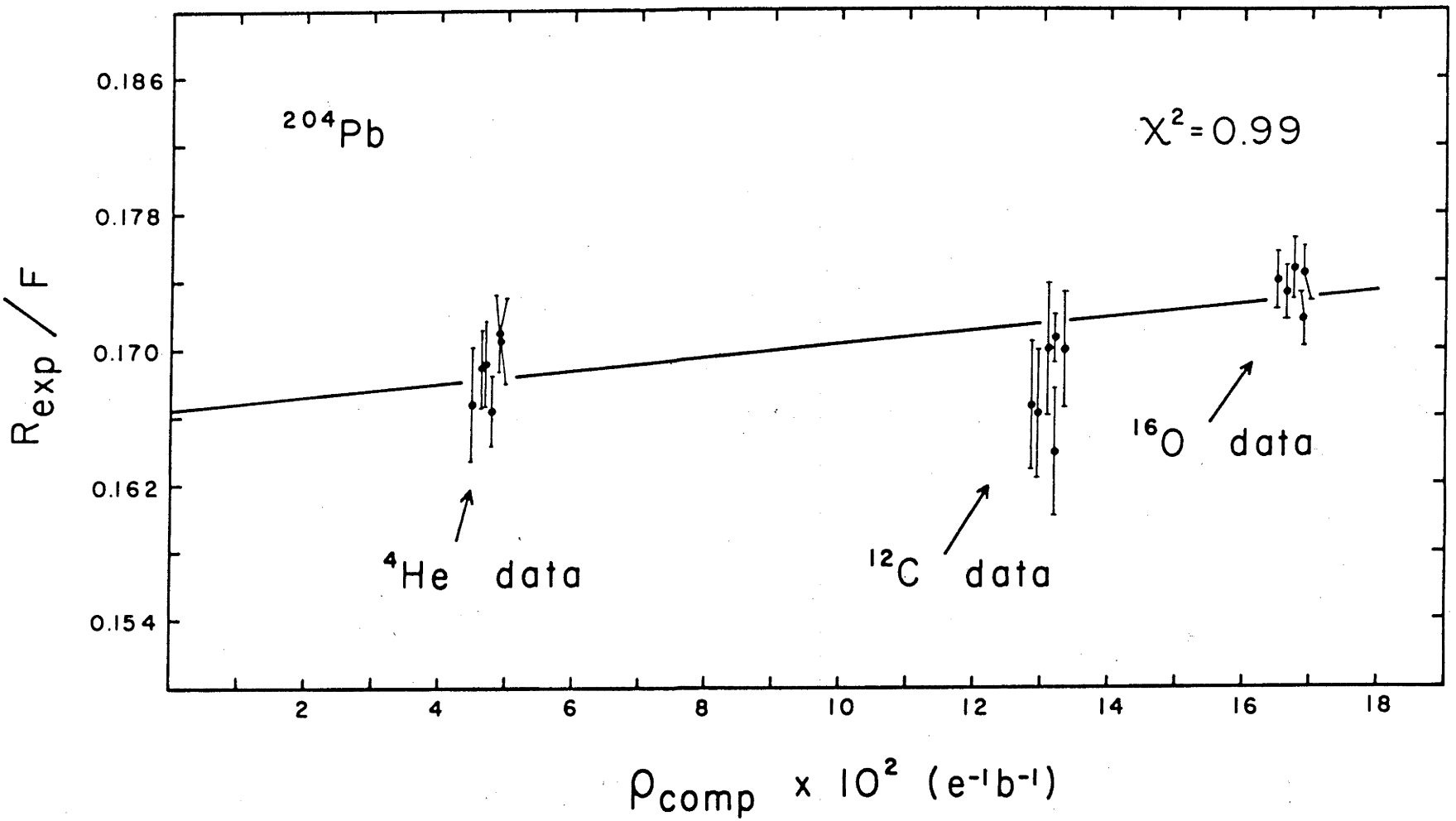

Fig. 5.6 The ratio R_{exp}/F for $^{204}Pb(2^+)$ as a function of the sensitivity parameter ρ_{comp}. The solid line represents a linear least squares fit to the data; the slope of this line is proportional to Q_{2+}.

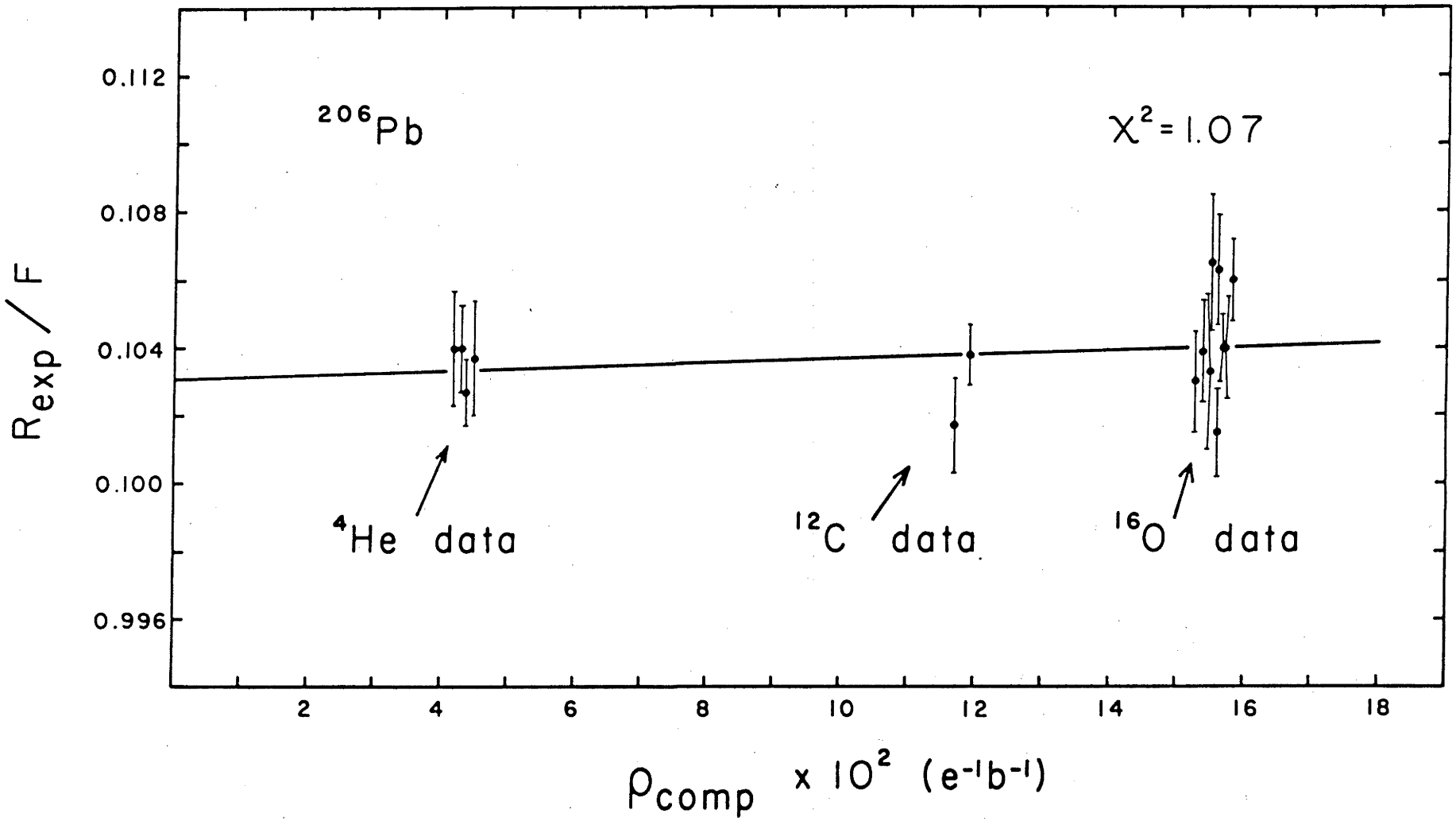

Fig. 5.7 The ratio R_{exp}/F for $^{206}Pb(2^+)$ as a function of the sensitivity parameter ρ_{comp}. The solid line represents a linear least squares fit to the data; the slope of this line is proportional to Q_{2+}.

5.4.2 Quantal Corrections

The quantal corrections discussed in chapter 2 were applied to the values of $F(\theta,\xi)$ and $\rho(\theta,\xi)$ obtained from the de Boer-Winther program. For both ^{204}Pb and ^{206}Pb the changes due to these corrections were $\Delta|Q_{2+}| = -0.019$ eb and $\Delta B(E2) = +0.0003\ e^2b^2$. The smaller fractional change in B(E2) is due to the correction to $F(\theta,\xi)$ being proportional to $1/\eta^2$, whereas that to $\rho(\theta,\xi)$ is proportional to $1/\eta$ (see table 2.1). The uncertainty introduced, in the value of Q_{2+}, by the application of the quantal corrections is estimated to be negligible since the only source of uncertainty is from second order terms ignored in the extrapolation used to calculate the corrections.

5.4.3 Effect of the Giant Dipole Resonance

The effect of the giant dipole resonance was included in the de Boer-Winther program as a modification to the Hamiltonian; this modification being proportional to the minus-two moment σ_{-2} of the photoabsorption cross section (see subsection 2.2.5). A number of measurements of σ_{-2} have been reported for ^{208}Pb (Mi62, Ha64, To68, Ve70, Bu72) and the mean of these is $\sigma_{-2} = 18.3 \pm 1.8$ mb/MeV, which corresponds to a value of $k = 0.72 \pm 0.07$ in eq. (2.29). Harvey et al. (Ha64) also obtained the values $\sigma_{-2} = 15.6 \pm 1.6$ mb/MeV ($k = 0.62 \pm 0.06$) for ^{206}Pb and $\sigma_{-2} = 14.5 \pm 1.5$ mb/Mev ($k = 0.57 \pm 0.06$) for ^{207}Pb. It therefore appears that the Levinger (Le57) estimate ($k = 1$) is consistently high for the Pb isot opes. Although σ_{-2} has not been measured for ^{204}Pb, its value is expected to be very similar to that of the other Pb isotopes, since k should be approximately constant (Le57). Using the same value $k = 0.62$ for

both ^{204}Pb and ^{206}Pb the change to the quadrupole moment obtained is $\Delta|Q_{2+}| = +0.038$ eb for ^{204}Pb and $\Delta|Q_{2+}| = +0.035$ eb for ^{206}Pb. If a value $k = 0.72$ is used, then the above changes are greater by 0.007 eb.

5.4.4 Effect of the 1.274 MeV 4^+ State in ^{204}Pb

In the case of ^{204}Pb, a peak corresponding to the 1.274 MeV 4^+ state was observed in both ^{12}C and ^{16}O spectra. Therefore, this state was included in the analysis. A value $B(E2; 4^+ \rightarrow 2^+) = (2.8 \pm 0.2) \times 10^{-5} e^2b^2$ (4×10^{-3} W.u.) was deduced from the partial half-life $T_{\frac{1}{2}} = 0.29 \pm 0.02$ μs which is the (unweighted) average of reported half-life measurements (Be60 ,Li67,Sa63). Signorini and Morinaga (Si72) have observed the $4^+ \rightarrow 0^+$ cross-over gamma-ray decay and from their measured branching ratio of (0.012 ± 0.002)% (somewhat larger than the previous upper limit of 0.005% (Ta62)) a value $B(E4; 4^+ \rightarrow 0^+) = (2.1 \pm 0.4) \times 10^{-3}\ e^2b^4$ is obtained. Using the above values, it was found that including the 4^+ state produced the changes $\Delta|Q_{2+}| = -0.0006$ eb for constructive interference ($P_4 = +1$) and $\Delta|Q_{2+}| = +0.0018$ eb for destructive interference ($P_4 = -1$). Clearly, interference from the 4^+ state has a very small effect on Q_{2+}.

5.4.5 Effect of the First 3^- State

As mentioned in chapter 4, the 3^- state near 2.6 MeV in both ^{204}Pb and ^{206}Pb is the most strongly excited state after the first 2^+ state. This octupole state is therefore expected to have a significant effect on the excitation probability of the 2^+ state,

particularly since the two states are connected by an El transition. For the 3^- state in ^{206}Pb, the mean lifetime for the transition to the first 2^+ state has been measured to be 0.125 ± 0.030 ps by Häusser et al. (Hä72), while Grosse et al. (Gr71) obtain a value of 0.4 ± 0.2 ps; taking Häusser's result (in view of the smaller error) one obtains a value $B(E1; 3^- \rightarrow 2^+) = (8.0 \pm 1.9) \times 10^{-6}\ e^2b$. Although no information is available regarding the strength of the $3^- \rightarrow 2^+$ transition in ^{204}Pb, this octupole state is of very similar nature to that in ^{206}Pb and therefore the same B(El) value as for ^{206}Pb was used in the analysis. The values used for $B(E3; 0^+ \rightarrow 3^-)$ were those measured in the present work (see table 5.1). The changes $\Delta|Q_{2+}|$ due to including the 3^- state are + 0.021 eb ($P_4 = -1$) and + 0.002 eb ($P_4 = +1$) for ^{204}Pb, and + 0.026 eb ($P_4 = -1$) and + 0.003 eb ($P_4 = +1$) for ^{206}Pb.

If the 3^- state is included in the analysis, together with the already mentioned corrections (including the 4^+ state), then the quadrupole moment obtained for ^{204}Pb is $Q_{2+} = +0.215 \pm 0.078$ eb for constructive interference ($P_4 = +1$) and $Q_{2+} = +0.236 \pm 0.078$ eb for destructive interference ($P_4 = -1$). For ^{206}Pb, the results are $Q_{2+} = +0.035 \pm 0.081$ eb ($P_4 = +1$) and $Q_{2+} = +0.059 \pm 0.081$ eb ($P_4 = -1$). The errors quoted above include an error ± 0.002 eb arising from uncertainties in the matrix elements connecting the 3^- state.

5.4.6 Effect of Higher 2^+ States

It has been found (St67) that, in general, interference from higher 2^+ states can have a significant effect on the excitation

probability of the first 2^+ state. Higher 2^+ states have been observed at 1.46 MeV and 1.75 MeV in ^{206}Pb (Se72), and at 1.93 MeV in ^{204}Pb (Ma71). Although no experimental information is available regarding the strength of the $2_2^+ \rightarrow 2_1^+$ and $2_2^+ \rightarrow 0_1^+$ transitions a number of theoretical calculations have been made for ^{206}Pb (but not for ^{204}Pb). Shell model calculations have been performed at Basel (Ha69, Gö70b) and the values $B(E2; 2_2^+ \rightarrow 2_1^+) = 4 \times 10^{-3}\ e^2b^2$, $B(E2; 2_2^+ \rightarrow 0_1^+) = 1.7 \times 10^{-2}\ e^2b^2$, and $B(E2; 2_1^+ \rightarrow 0_1^+) = 9 \times 10^{-3}\ e^2b^2$ were obtained. There appears to be a number of inconsistencies in these calculations:

a) The strength predicted for the $2_2^+ \rightarrow 0_1^+$ transition is about the same as that measured experimentally for the $2_1^+ \rightarrow 0_1^+$ transition. In a 60 MeV ^{16}O spectrum, such a 2^+ state at 1.75 MeV should give rise to a peak with an intensity 1/10 that of the 2_1^+ peak. In the present work, the 2_2^+ intensity was estimated to be less than 1/100 that of the 2_1^+ peak.

b) The predicted $2_1^+ \rightarrow 0_1^+$ strength is only half the experimental value.

c) In collective models one would expect that $B(E2; 2_2^+ \rightarrow 2_1^+) >> B(E2; 2_2^+ \rightarrow 0_1^+)$.

Sorensen (So70) has used the pairing-plus-quadrupole model to predict that for a 2_2^+ state near 2 MeV $B(E2; 2_2^+ \rightarrow 2_1^+) = 2 \times 10^{-2}\ e^2b^2$, and $B(E2; 0_1^+ \rightarrow 2_2^+) = 1 \times 10^{-3}\ e^2b^2$ (also $B(E2; 0_1^+ \rightarrow 2_1^+) = 0.12\ e^2b^2$). Since these values are more consistent with experiment, they have been adopted here (the same values are assumed for ^{204}Pb). The effect obtained by including the 1.93 MeV state in ^{204}Pb is to change the measured Q_{2+} by $\Delta|Q_{2+}| = \pm 0.02$ eb,

Table 5.2 Effect on $|Q_{2+}|$ and B(E2; $0^+ \rightarrow 2^+$) of corrections applied for various processes.

Process	^{204}Pb		^{206}Pb	
	$\Delta\|Q_{2+}\|$ (eb)	ΔB(E2) (e^2b^2)	$\Delta\|Q_{2+}\|$ (eb)	ΔB(E2) (e^2b^2)
electron screening plus vacuum polarization	+0.003	-0.0005	+0.004	-0.0003
quantal correction	-0.019	+0.0003	-0.019	+0.0003
giant dipole resonance	+0.038	+0.0003	+0.035	+0.0003
1.27 MeV 4^+ state $P_4 = +1$	-0.0006	-0.00004	-	-
$P_4 = -1$	+0.0018	-0.00005	-	-
2.6 MeV 3^- state $P_4 = +1$	+0.002	-0.00004	+0.003	-0.00005
$P_4 = -1$	+0.021	-0.00008	+0.026	-0.00012
2.0 Mev 2^+ state $P_4 = +1$	-0.022	+0.00006	-0.031	+0.00006
$P_4 = -1$	+0.020	-0.00004	+0.030	-0.00008

while the effect of the 1.75 MeV state in ^{206}Pb is $\Delta|Q_{2+}| = \pm 0.03$ eb (see table 5.2). If Sorensen's calculations refer to the 1.46 MeV state, in ^{206}Pb, instead of the 1.75 MeV state, then the above value of $\Delta|Q_{2+}|$ becomes about 15% larger.

5.4.7 Adopted Values

It can be concluded that the total correction to Q_{2+} arising from electron screening, vacuum polarization, the quantal approximation and the GDR is smaller than the error arising from the uncertainties in the intensity extraction. The higher states observed to be populated also have relatively little effect on the value of Q_{2+}.

Since the values of Q_{2+} obtained for the different signs of the interference (from the 4^+ and 3^- states) are very similar, the average of the two values can be adopted and the uncertainty as to the sign of the interference can be included in the total error. The adopted values are $Q_{2+} = + 0.23 \pm 0.09$ eb and $B(E2; 0^+ \rightarrow 2^+) = 0.166 \pm 0.002\ e^2b^2$ for ^{204}Pb, and $Q_{2+} = + 0.05 \pm 0.09$ eb and $B(E2; 0^+ \rightarrow 2^+) = 0.103 \pm 0.001\ e^2b^2$ for ^{206}Pb. The uncertainties in the above values take into account statistical and systematic errors in the extraction of peak areas (see chapter 4), target-thickness uncertainties, uncertainties in beam energy, and the uncertainty as to the sign of the interference from the 3^- (and 4^+ for ^{204}Pb) state; uncertainties arising from the possible presence of contaminants under elastic and inelastic peaks are not included. The results obtained in this section will be compared with those of previous measurements in chapter 6.

For ^{204}Pb it can be seen from figure 5.6 that the ^{12}C data points are consistently below the line representing the best fit to all the data. If only the ^4He and ^{12}C data are used to calculate Q a value of $Q_{2+} = +0.09 \pm 0.09$ e.b. is obtained, whereas if the ^4He and ^{16}O data are used Q becomes $Q_{2+} = +0.27 \pm 0.05$ e.b. (The errors quoted are purely statistical). It is clear that the errors quoted are too small indicating a possible systematic error. The error in the final value has been increased to accommodate this discrepancy and the results for ^{204}Pb become $Q_{2+} = +0.23 \pm 0.14$ eb and $B(E2;0^+\rightarrow2^+) = 0.166 \pm 0.002\ e^2b^2$.

exp comp

nevertheless appears to be a decrease at energies above 60 MeV. If a conservative approach is adopted, then the maximum safe energy is taken to be 60 MeV. This bombarding energy corresponds to a

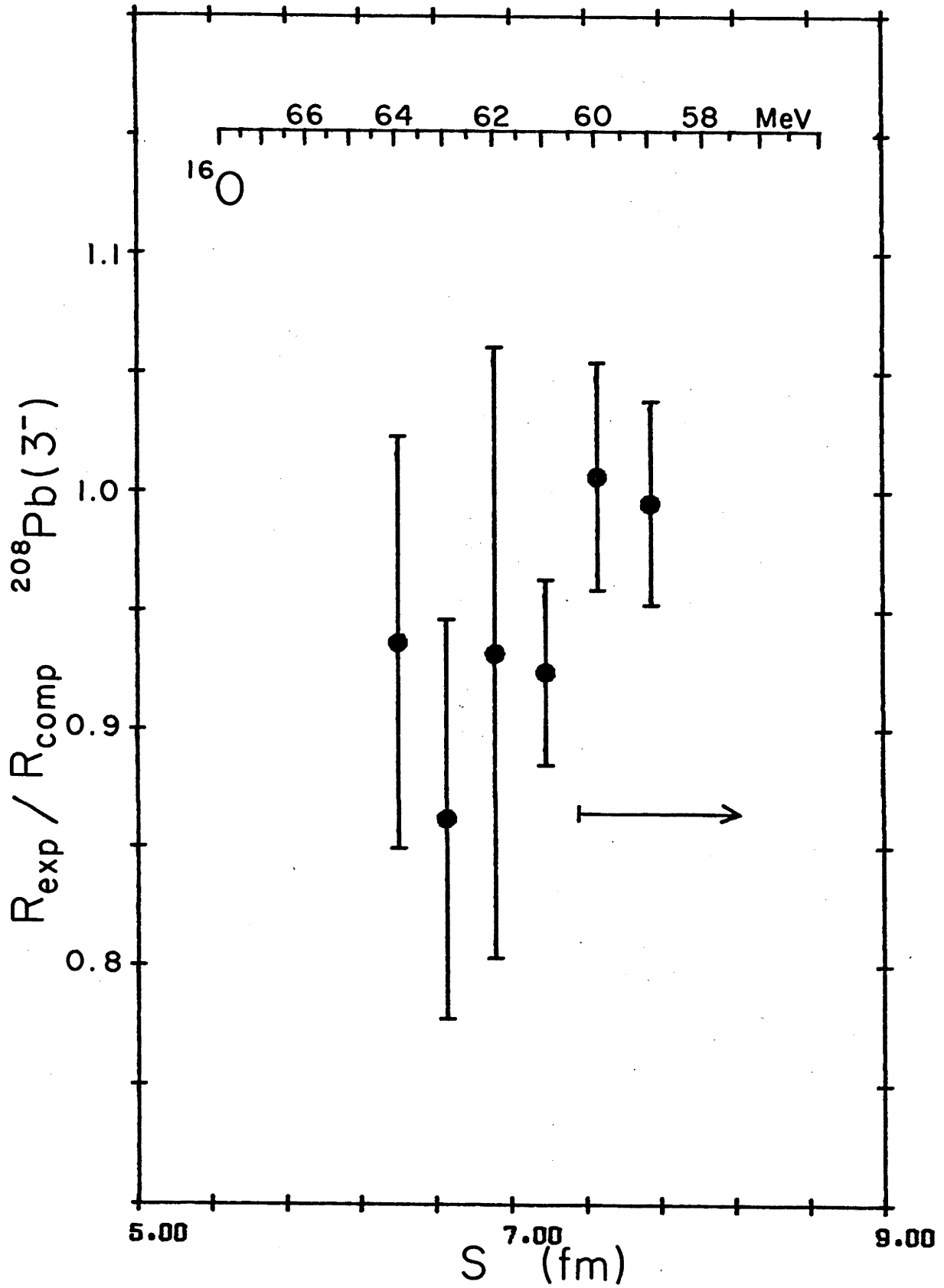

Fig. 5.8 The double ratio R_{exp}/R_{comp} for ^{208}Pb (3^-) and ^{16}O projectiles, as a function of the distance of separation S (eq. (5.3)). The unlabelled arrow indicates adopted safe energies.

separation of equivalent sharp radii (ESR) of about 7.5 fm and is consistent with the conclusions reached for the 3^- state in $^{204,206}Pb$ (section 5.2).

For ^4He, excitation probabilities were about 15 times smaller than for ^{16}O and it was not feasible to obtain an excitation function similar to that shown in fig. 5.8 for ^{16}O. It was therefore necessary to use the calculations of Feng et al. (Fe76), which predict a 1% deviation from pure Coulomb excitation at a separation distance of about 7.4 fm, and the ^4He data for the 3^- state in $^{204,206}Pb$ (section 5.2) as an indication of maximum safe energies. In view of the above considerations, the data were taken at bombarding energies of 15.1 MeV and 15.3 MeV; these energies correspond to separation distances of 7.5 fm and 7.3 fm respectively.

Values of B(E3) and Q_{3-} were determined from the experimental excitation probabilities (table 4.6) according to the procedure outlined in subsection 5.3. The fit to the data is shown in fig. 5.9 where $R_{exp}/F(\theta,\xi)$ is plotted against the sensitivity parameter $\rho(\theta,\xi)$. The results obtained are $B(E3;\ 0^+ \rightarrow 3^-) = 0.665 \pm 0.035\ e^2b^3$ and $Q_{3-} = -0.42 \pm 0.32$ eb. The uncertainties in these results take into account statistical and systematic errors in the extraction of peak areas, target-thickness uncertainties, and uncertainties in beam energy. However, uncertainties arising from the possible presence of contaminants under elastic and inelastic peaks are not included.

Only corrections for electron screening and vacuum polarization are included in the above results and their combined effect is to increase $|Q_{3-}|$ by 0.03 eb. Quantal corrections were not applied since no information is available regarding quantum mechanical calculations for E3 excitation. However, if quantal corrections

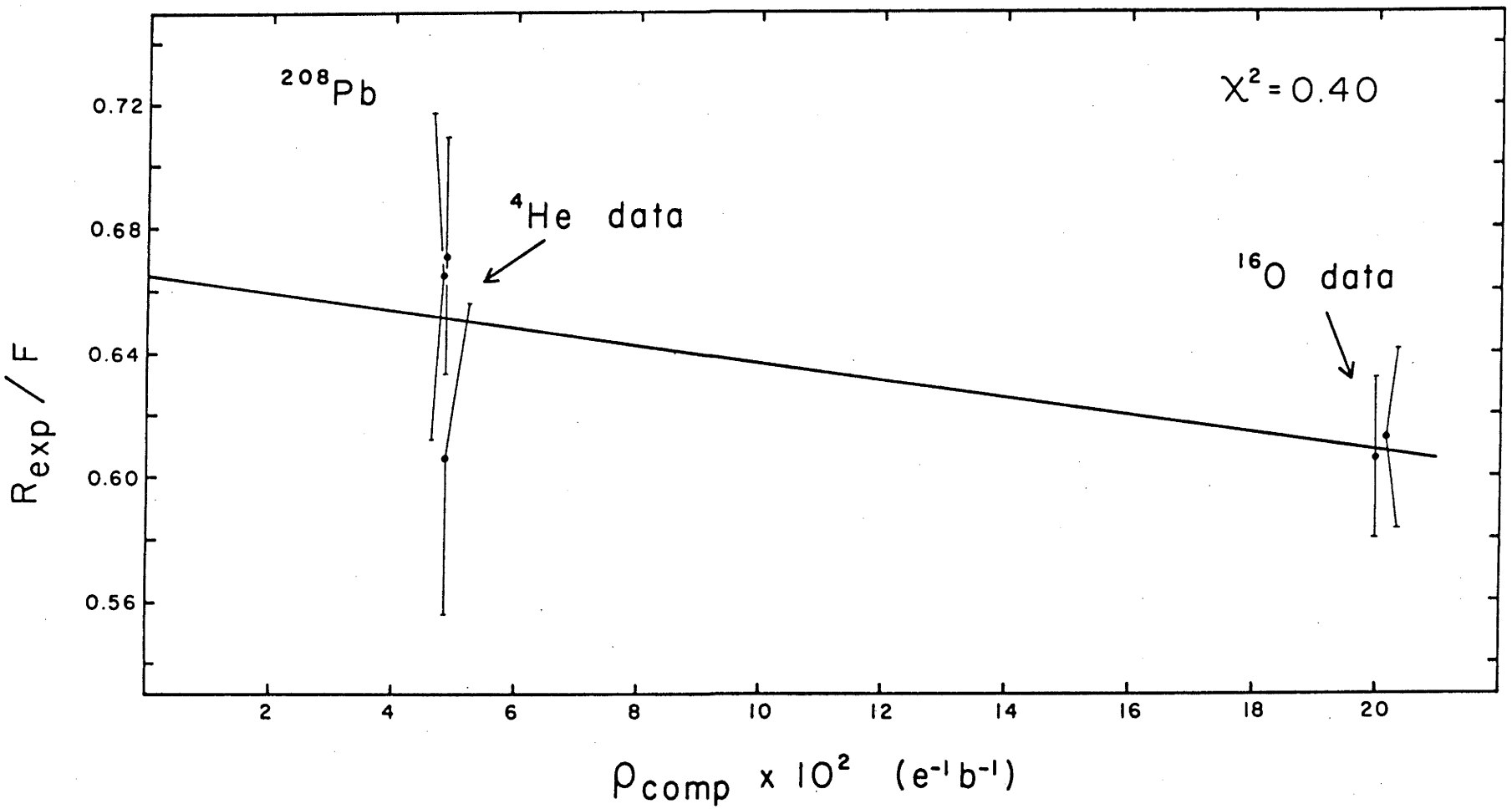

Fig. 5.9 The ratio R_{exp}/F for $^{208}Pb(3^-)$ as a function of the sensitivity parameter ρ_{comp}. The solid line represents a linear least squares fit to the data; the slope of this line is proportional to Q_{3-}.

are assumed to be the same as for E2 excitation, then the result would be to increase $|Q_{3-}|$ by 0.006 eb. (Such a small correction compared to that in $^{204,206}Pb$ is a consequence of the fact that quantal corrections are smaller for large values of the adiabaticity parameter ξ; for $^{208}Pb(3^-)$ $\xi \approx 1.3$ while for $^{204,206}Pb(2^+)$ $\xi \approx 0.4$.) The likely size of the quantum mechanical correction is therefore estimated to be much smaller than the uncertainty in Q_{3-}.

The effect of the giant dipole resonance (GDR) was simulated by including a single 1^- level at 14 MeV in the Winther-de Boer program (the reason for this procedure is explained in subsection 2.2.5). For the GDR a reduced transition probability $B(E1; 0^+ \rightarrow 1^-) \approx$ 10 W.u. has been found experimentally (Bu72, Pi74). Since there is no strong theoretical basis for assuming the $1^- \rightarrow 3^-$ (E2) transition to be either inhibited or enhanced, a value $B(E2; 1^- \rightarrow 3^-) = 1$ W.u. was adopted (Barnett and Phillips (Ba69) considered that even 0.1 W.u. was probably an overestimate). The results of this calculation show that the GDR would reduce $|Q_{3-}|$ by 0.16 eb; if a value $B(E2; 1^- \rightarrow 3^-) = 0.1$ W.u. is used, then $|Q_{3-}|$ is reduced by 0.11 eb. The isoscalar giant quadrupole resonance near 10 MeV (Bu72, Na73, Pi74, Ma75) is not expected to have any effect on the present results since an E1 transition to the 3^- state is forbidden by selection rules (Ko76).

The possibility of interference from the 4.09 MeV 2^+ state was also investigated. The value $B(E2; 0^+ \rightarrow 2^+) = 0.30 \pm 0.02$ e^2b^2 has been determined experimentally from electron scattering (Na71, Zi68). The strength of the $2^+ \rightarrow 3^-$ transition has not been measured but the value $B(E1; 2^+ \rightarrow 3^-) = 8 \times 10^{-5}$ e^2b assumed by Häusser (Hä72) has been adopted (this is somewhat larger than the value $B(E1; 2^+ \rightarrow 3^-) =$

2.3×10^{-5} e^2b assumed by Barnett and Phillips (Ba69), and the value $B(E1; 2^+ \rightarrow 3^-) = 1.12 \times 10^{-5}$ e^2b determined for ^{206}Pb (Hä72)). Calculations show that the effect of the 2^+ state is to change $|Q_{3-}|$ by $+0.01$ eb for constructive interference ($P_4 = -1$) and by -0.07 eb for destructive interference ($P_4 = +1$).

The 3.20 MeV 5^- state has been observed to decay to the 3^- state by a pure E2 transition (Ja72). The half-life for this transition is $T_{\frac{1}{2}} = 0.298 \pm 0.017$ ns (We62) from which a value $B(E2; 5^- \rightarrow 3^-) = (2.76 \pm 0.16) \times 10^{-3}$ e^2b^2 is deduced. A value $B(E5; 0^+ \rightarrow 5^-) = 0.05 \pm 0.01$ e^2b^5 is obtained from the average of experimental data (Al67, Fr72, Na71, Zi68). Interference from this state would change Q_{3-} by $\Delta|Q_{3-}| = +0.009$ eb ($P_4 = -1$) or $\Delta|Q_{3-}| = -0.010$ eb ($P_4 = +1$). The 3.71 MeV 5^- state is expected to have very little effect since its decay is mainly to the 3.20 MeV 5^- state with only a weak branch to the 3^- state (Pa69).

Finally one must also consider the process of virtual nucleon tunnelling whereby a nucleon can tunnel through the Coulomb barrier twice and leave the ^{208}Pb nucleus in its 3^- state. This problem is also present in E2 reorientation experiments but since it is likely to have a small cross section compared to that of E2 Coulomb excitation, it has been ignored. In the present case the E3 Coulomb excitation cross section is 40 times smaller than the E2 excitation cross section in $^{204,206}Pb$ and therefore virtual nucleon tunnelling may be a significant process. This problem was also considered to be important by Barnett and Phillips (Ba69) particularly since at 69.1 MeV they observed (Ba71) single nucleon transfer peaks, from the $^{208}Pb(^{16}O,^{17}O)^{207}Pb$ and $^{208}Pb(^{16}O,^{15}N)^{209}Bi$ reactions, whose intensities were comparable to the 3^- peak (particularly at backward

angles). In the present data taken near 60 MeV (see fig. 4.12) the peaks from the $^{208}Pb(^{16}O,^{17}O)^{207}Pb(g.s)$ and $^{208}Pb(^{16}O,^{15}N)^{209}Bi(0.897)$ reactions (these have been observed to be the strongest peaks (Ba71)) are 6 and 20 times smaller (respectively) than the 3^- peak. It is therefore concluded that in the present work the effect of virtual nucleon tunnelling is likely to be small.

CHAPTER 6

DISCUSSION OF RESULTS AND CONCLUSION

In the present chapter, the results obtained in chapter 5 for quadrupole moments and reduced excitation probabilities are compared with those of other experiments and with the predictions of theoretical calculations. For ^{208}Pb, arguments are presented against a large value of Q_{3-} in terms of its consequences on certain features of nuclear structure. In the case of ^{204}Pb and ^{206}Pb, intrinsic shape parameters are deduced according to the sum rule method described in chapter 1. Systematic trends in the intrinsic shapes of nuclei in the mass region A = 184 - 206 are presented.

6.1 The Nuclei ^{204}Pb and ^{206}Pb

6.1.1 Comparison of Present and Previous Experimental Results

The value $Q_{2+} = 0.23 \pm 0.09$ eb obtained for ^{204}Pb in the present measurement is in excellent agreement with the value $Q_{2+} = 0.19 \pm 0.14$ eb obtained by Olin et al. (0174), who also used the reorientation effect in Coulomb excitation. The experimental technique employed by Olin et al. consisted of bombarding an enriched ^{204}Pb target with 100 - 125 MeV ^{32}S ions, and detecting the ^{32}S particles scattered at 70^{o} and 180^{o} in coincidence with the de-excitation gamma rays. The gamma-ray coincidence served to select the inelastic events in the particle spectrum (a general outline of this experimental technique is given in subsection 3.1.1b). The determination of Q_{2+} made use of the dependence of the reorientation effect on the scattering

angle (see section 3.1). Coulomb-nuclear interference was investigated and Olin et al. found that the minimum safe distance (as defined in section 5.1) for ^{32}S projectiles was about 6.6 fm; this is in good agreement with the minimum safe distance of about 6.7 fm determined in the present work for ^{4}He, ^{12}C, and ^{16}O projectiles. In their analysis, Olin et al. included interference effects from the 1.274 MeV 4^+ state but did not include the effect of the 3^- state near 2.6 MeV; if the 3^- state is excluded from the present analysis, then a value $Q_{2+} = 0.21 \pm 0.08$ eb is obtained and the agreement with Olin et al. is improved. Olin et al. do not state whether corrections for the giant dipole resonance, electron screening, vacuum polarization, and quantal effects were included in their analysis; if these corrections are excluded from the present analysis, then the value $Q_{2+} = 0.19 \pm 0.08$ eb is obtained, which agrees exactly with the value of Olin et al.

No previous measurement of Q_{2+} has been made for ^{206}Pb. The present value $Q_{2+} = 0.05 \pm 0.09$ eb is smaller than that of ^{204}Pb, as would be expected as one approaches a double closed shell. The present result is also not inconsistent with the value $Q_{2+} = 0$ predicted for a harmonic vibrator.

The values of $B(E2; 0^+ \rightarrow 2^+)$ for ^{204}Pb and ^{206}Pb obtained in the present work are compared to those from previous measurements in table 6.1; ^{1}H and ^{4}He inelastic scattering measurements give results which differ substantially from the present results and have not been included. Some of the bombarding energies used by Hrynkiewicz (Hr66) were above the maximum safe energy and only the result taken at a safe bombarding energy is quoted in table 6.1. In the experimental method

used by Häusser et al. (Hä70a, Hä72) and by Grosse et al. (Gr71) the gamma-ray yield measured is the result of Coulomb excitation over all projectile scattering angles and over projectile energies ranging from the bombarding energy to zero energy as the projectile slows down in the thick target. In this situation, the minimum value of the distance of separation S between nuclear surfaces (as defined in section 5.1) is that arising from a projectile with an energy equal to the bombarding energy and which is scattered at 180^{o}. In the experiments of Häusser et al. and Grosse et al. the minimum values of S were 5.7 fm (17 Mev ^{4}He) and 4.9 fm (18 MeV ^{4}He) respectively, and since these values are less than the minimum safe distance of 6.7 fm (as determined in the present work) it is evident that the data obtained by these authors was not entirely free from nuclear effects. Coulomb-nuclear interference may therefore be the reason for the B(E2) of Häusser et al. and Grosse et al. being lower (with one exception) than those of the present work. Nevertheless, the values in table 6.1 are in good agreement with each other and all are within two standard deviations of the present results.

6.1.2 Theoretical Calculations of Q_{2+} and B(E2)

The lead region, especially those nuclei close to the doubly magic ^{208}Pb nucleus has been a popular region for shell model calculations. It is also a region where new models, and modifications and extensions to the shell model can be tested. Although there have been numerous calculations for ^{204}Pb and ^{206}Pb, many are concerned with reproducing energy level schemes only, while others use the experimental B(E2)'s as a basis to derive the neutron and proton

Table 6.1 Comparison of present and previous experimental values of B(E2; $0^+ \rightarrow 2^+$) (e^2b^2) for ^{204}Pb and ^{206}Pb

^{204}Pb	^{206}Pb	Ref	Comments
0.166 ± 0.002	0.103 ± 0.001	this work	
0.166 ± 0.009		0174	
0.151 ± 0.015	0.095 ± 0.005	Hä72	Coul.ex.; thick target yield
0.146 ± 0.015	0.103 ± 0.008	Gr71	"
0.156 ± 0.018	0.094 ± 0.006	Hä70a	"
	0.091 ± 0.006	Qu70	recoil-distance Doppler shift
	$0.118 \pm \begin{matrix} 0.020 \\ 0.023 \end{matrix}$	Hr66	Coul.ex.; particle-γ ray coincidence

effective charges and to determine transition probabilities for higher states. Therefore, only theoretical treatments which calculate quadrupole moments or which do not treat the effective charges as free parameters to reproduce the B(E2) values, will be discussed; these are listed in table 6.2.

Shell model calculations in which nuclear structure is described in terms of neutron holes occupying orbitals within an otherwise inert ^{208}Pb case can be characterised in terms of the effective residual force which is assumed for the interaction between two neutron holes. An early calculation by Hadermann et al. (Ha67) employed a delta force for the residual interaction, and numerical calculations were performed using the quasi-boson approximation. It can be seen that the large negative value predicted for the quadrupole moment is in strong disagreement with experiments. Nevertheless, this simple effective residual interaction is able to give a reasonable value

Table 6.2 Comparison between experimental and theoretical values of $B(E2; 0^+ \rightarrow 2^+)$ and Q_{2+} for the first 2^+ state in ^{204}Pb and ^{206}Pb. Details of calculations are explained in the text.

Nucleus	Q_{2+} (eb)	$B(E2;0^+\rightarrow2^+)$ (e^2b^2)	Reference	Description
^{206}Pb	+0.05±0.09	0.103±0.001	this work	experiment
	±0.29	-	eq. (1.11)	rotational model
	-0.51	0.128	Ha67	shell model
	-0.04	0.047	Ha68	shell model
		0.042	Ha69	shell model
		0.046	Gö70	shell model
		0.122	Ma72(Tr68)	shell model
		0.122	Ma72(Ku71)	shell model
		0.083	McGr75	shell model
		0.101-0.123	Va71	shell model
		0.107-0.130	Va71	random phase approximation (RPA)
	+0.33		Za72(Tr68)	(shell model)
	+0.32		So70	pairing plus quadrupole
		0.084	Sp73(RPA)	finite Fermi systems
		0.109	Sp73(Fr69)	finite Fermi systems
		0.120	Kl73(Ku71)	finite Fermi systems
	+0.08		Sp72	finite Fermi systems
	+0.02		Br72	particle vibration coupling
^{204}Pb	+0.23±0.09	0.166±0.002	this work	experiment
	±0.37	-	eq. (1.11)	rotational model
		0.256	Ha67	shell model
	+0.04		Br72	particle vibration coupling

for the B(E2) in ^{206}Pb. (However, the prediction of this theory that the B(E2) for ^{204}Pb should be twice as large as for ^{206}Pb clearly disagrees with experiment.) Hadermann (Ha68) subsequently used a residual interaction with a Gaussian radial dependence and with an angular dependence which was assumed to be a delta function. The quadrupole moment obtained in this calculation is considerably smaller in magnitude than the previous prediction and agrees with experiment. However the B(E2) is now too small by a factor of two. Adding spin-spin and tensor terms (Ha69) to the residual interaction produced little change to the theoretical B(E2) although better agreement with experiment was obtained for the energy level scheme of ^{206}Pb. Including four-particle core excitation (Go70) (note that only core spins 0 were considered) only marginally increased the predicted B(E2), although further improvements were obtained for the energy level scheme.

A number of more recent shell model calculations make reasonable predictions for the B(E2) in ^{206}Pb. Manthuruthil et al. (Ma72) have calculated the B(E2) from the wave functions of True (Tr68), who added a weak-coupling force to an effective interaction with a Gaussian radial dependence, and Kuo and Herling (Ku71), who used a "realistic" effective interaction based on the Hamada-Johnston potential. The same "realistic" interaction was recently employed in the shell model calculation of McGrory and Kuo (McGr75). Vary and Ginocchio (Va71) have compared a shell model calculation with a two-nucleon random phase approximation (RPA) calculation, and obtained similar results for both. True's wave functions were also used by Zamick (Za72) to calculate the quadrupole moment in ^{206}Pb; the result obtained is in poor agreement with experiment.

A pairing-plus-quadrupole interaction was used by Sorensen (So70) to approximate the residual interaction and a fourth order boson expansion calculation was performed. Since the effective charge was chosen to match approximately the experimental B(E2) for ^{206}Pb, only the quadrupole moment is compared to experiment in table 6.2; clearly the predicted value of Q_{2+} is too large in magnitude. Nevertheless, an interesting feature of Sorensen's calculation is that the potential energy of quadrupole deformation $V(\beta,\gamma)$ (see section 1.5) was calculated; this is shown for ^{206}Pb in fig. 6.1 where, for comparison, that for ^{208}Pb is also shown.

Speth et al. (Sp73, Kl73) have extended the theory of finite Fermi systems of Migdal (Mi67) to cover the case of even-mass nuclei. The advantage of this theory is that no effective charges are assumed. Theoretical B(E2) values for ^{206}Pb were calculated using results from a RPA calculation, from the wave functions of Freed and Rhodes (Fr69), and from the wave functions of Kuo and Herling (Ku71). All the predicted B(E2)'s are in reasonable agreement with experiment. This theory has also been used to calculate the quadrupole moment of ^{206}Pb (Sp72) and is in good agreement with the present experimental value.

In the particle-vibration model the motion of the neutron holes is coupled to the vibrational modes of the ^{208}Pb core via oscillations in the one-body potential. Broglia (Br72) has used the particle-vibration model to calculate the quadrupole moment of all the even-mass lead isotopes from ^{196}Pb to ^{206}Pb. All the values of Q_{2+} are predicted to be small and although the theoretical value of ^{206}Pb agrees with experiment, the agreement is not as good in the case of ^{204}Pb.

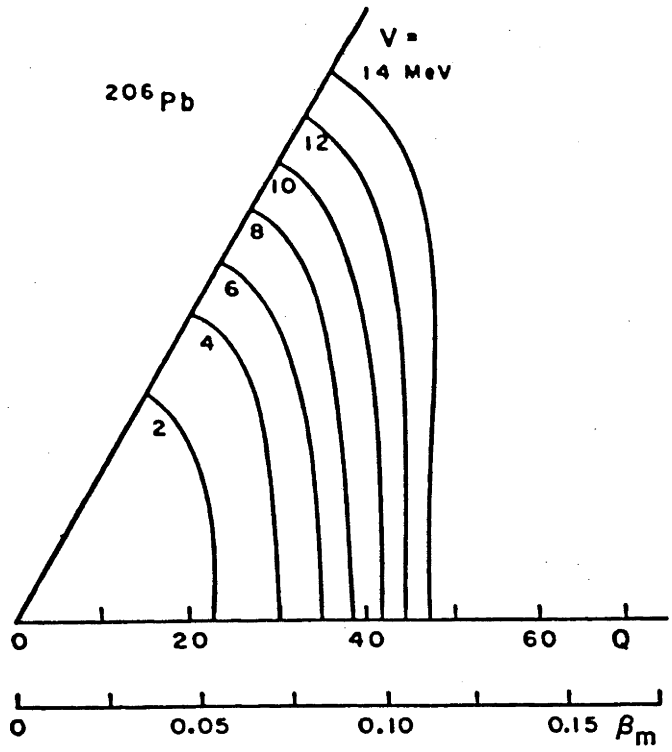

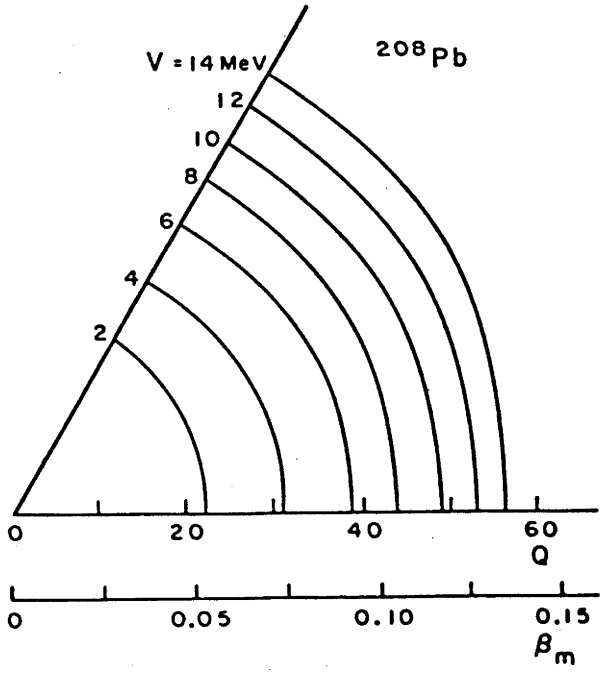

Fig. 6.1 Contour plots of the potential energy of quadrupole deformation $V(\beta,\gamma)$ calculated by Sorensen (So70). In this figure, Q is the intrinsic mass quadrupole moment, and β_m is the mass deformation parameter.

In conclusion, there is a definite need for further theoretical investigations in order to develop a theory that can simultaneously explain the observed quadrupole moment in both ^{204}Pb and ^{206}Pb. The present experimental results for Q_{2+} agree with the theoretical values of de Broglia and Speth, but disagree with those of Zamick and Sorensen.

6.1.3 Intrinsic Shape

It is interesting to apply the sum rule method, described in section 1.5, to calculate the intrinsic shape parameters for ^{204}Pb and ^{206}Pb. The result for ^{204,206}Pb will later be compared with those for other nuclei in the mass range A = 184 to A = 198. Table 6.3 shows the results of a sum rule analysis of the available E2 information for ^{204}Pb and ^{206}Pb; the second column indicates the state s for which Q_s^i, γ_s^i and β_s are calculated, and the third column shows the states included in the analysis. It can be seen that for the 0^+ ground state of ^{204}Pb and ^{206}Pb the deformation β_{0+} is very small - there is only a 3-4% deviation from sphericity - and follows the expected trend of increasing as one moves away from a double closed shell. Although the values of γ_{0+}^i imply that the ground states of ^{204}Pb and ^{206}Pb are asymmetric (see fig. 1.5), this asymmetry is of little consequence in view of the uncertainties in γ_{0+}^i and in view of the small magnitude of the deformation β_{0+}. Furthermore, nuclei are not rigid but can spend a fraction of their time in various shapes; in particular, nuclei near double closed shells are expected to have a potential energy of deformation $V(\beta,\gamma)$

Table 6.3 Intrinsic shape parameters obtained from the sum rule method. When a $2^{+'}$ state is included in the analysis, the uncertainty in the sign P_4 of the interference gives rise to two values for γ_s^i .

Nucleus	State	Intermediate States	Q_s^i (eb)	β_s	γ_s^i (deg)
^{206}Pb	0^+	$0^+,2^+$	1.018±0.005	0.0326±0.0002	33±6
	0^+	$0^+,2^+,2^{+'}$	1.023	0.0330	30($P_4=-1$)
					36($P_4=+1$)
	2+	$0^+,2^+$	0.465±0.034	0.0149±0.0011	45±26
	2^+	$0^+,2^+,2^{+'}$	0.646	0.0207	33($P_4=-1$)
					39($P_4=+1$)
^{204}Pb	0^+	$0^+,2^+$	1.292±0.008	0.0417±0.0003	43±8
	0^+	$0^+,2^+,2^{+'}$	1.296	0.0420	41($P_4=-1$)
					44($P_4=+1$)
	2^+	$0^+,2^+$	0.720±0.101	0.0233±0.0033	60^{+0}_{-16}
	2^+	$0^+,2^+,4^+$	0.721±0.101	0.0233±0.0033	60^{+0}_{-16}
	2^+	$0^+,2^+,4^+,2^{+'}$	0.849	0.0274	44($P_4=-1$)
					49($P_4=+1$)

similar to that shown in fig. 1.6, and are therefore expected to experience large fluctuations in the γ direction (i.e. they are "soft" in the γ direction).

An additional feature of the values in table 6.3 is the striking difference in Q_s^i and γ_s^i between the 0^+ ground state and the 2^+ first excited state. Although the values Q_s^i and γ_s^i are allowed to change from one state to another, one would expect only a gradual change for a rigid nucleus near a double closed shell. In

the case of ^{204}Pb and ^{206}Pb, only a few matrix elements are known from experiment and in addition to the errors for Q_s^i and γ_s^i (these errors being derived from the errors associated with the matrix elements) one must consider an additional uncertainty arising from E2 strength not included in the sums $p_s^{(2)}$ and $p_s^{(3)}$. To test the convergence of these sums, a $2^{+'}$ state was also included in the analysis; following the practice initiated in subsection 5.4.6, the matrix elements for this state were obtained from the pairing-plus-quadrupole calculation of Sorensen (So70) (with the matrix elements for ^{204}Pb assumed to be the same as for ^{206}Pb). It can be seen from table 6.3 that including the $2^{+'}$ state has little effect on the values of Q_{0+}^i and γ_{0+}^i for the ground state. On the other hand, there is a marked change in the values Q_{2+}^i and γ_{2+}^i when the $2^{+'}$ state is included, and these new values are much closer to those of the ground state. Including a $2^{+'}$ state also gives a "sensible" value of γ_{2+}^i for the 2^+ state in ^{204}Pb and resolves the problem of a value greater than one being obtained for the right-hand side of eq.(1.18), with a consequent $\gamma_{2+}^i = 60^o$ assignment. It may therefore be concluded that while the values Q_{0+}^i and γ_{0+}^i already show a good convergence when only two states (0^+ and 2^+) are included, the values Q_{2+}^i and γ_{2+}^i in table 6.3 are unreliable due to some missing E2 strength.

The systematics of nuclei in the region of the periodic table between A = 184 and A = 206 are shown in fig. 6.2; the values for Q_{2+} and B(E2; $0^+ \rightarrow 2^+$) are taken from Christy and Häusser (Ch72) for all nuclei except ^{204}Pb and ^{206}Pb where the values from the present work are used, and except ^{198}Hg where the values are those from a

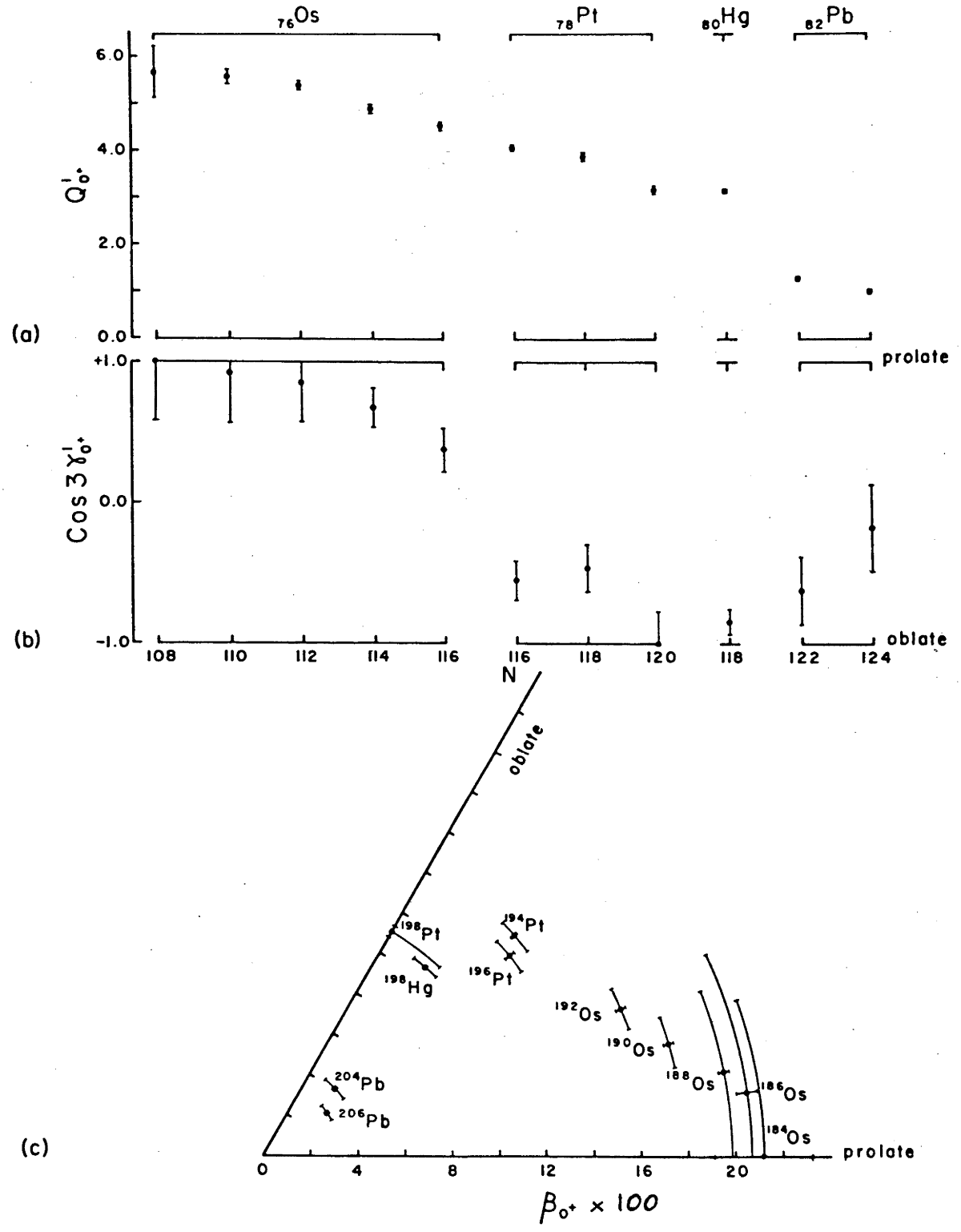

Fig. 6.2 Systematics of nuclei in the region of the periodic table between A = 184 and A = 206. Features of this figure are discussed in the text.

recent measurement in this laboratory (Fe77a). Fig. 6.2a shows the gradual increase in deformation as one moves away from the double closed shell. The well known oblate-prolate transition near ^{192}Os can clearly be seen in fig. 6.2b where $\cos 3\gamma^{i}_{0+} = -1$ corresponds to an oblate shape and $\cos 3\gamma^{i}_{0+} = +1$ corresponds to a prolate shape. The information in figs. 6.2a and 6.2b is combined in fig. 6.2c which is a plot of the values (β_{0+},γ_{0+}).

6.2 The Nucleus ^{208}Pb

6.2.1 Comparison of Present and Previous Experimental Results

The present experimental results for Q_{3-} and $B(E3; 0^{+} \rightarrow 3^{-})$ are compared to previous measurements in table 6.4. It can be seen that the present value of Q_{3-} is smaller than both previous measurements of Barnett et al. (Ba69, Ba72) by a factor of about three.

The first measurement of Q_{3-} by Barnett and Phillips (Ba69) employed the reorientation effect in Coulomb excitation and used an experimental technique similar to that used in the present work. An enriched target was bombarded with 17.5 MeV and 18 MeV ^{4}He and with 69.1 MeV ^{16}O projectiles, and the scattered particles were detected with silicon surface barrier detectors placed at laboratory scattering angles from about 85^{o} to about 170^{o}. Data were also taken with 19 MeV ^{4}He ions but at this energy, the effects of Coulomb-nuclear interference were observed and these data were not included in the analysis. Although Barnett and Phillips assumed that nuclear effects at the above energies were negligible, it appears that the majority of these data were in fact taken at energies where the distance of

Table 6.4 Comparison of present and previous experimental values of Q_{3-} and B(E3; $0^+ \rightarrow 3^-$) for ^{208}Pb.

Q_{3-} (eb)	B(E3; $0^+ \rightarrow 3^-$) (e^2b^3)	Reference	Comments
-0.42 ± 0.32	0.665 ± 0.035	this work	
-1.1 ± 0.4		Ba72	reorientation
-1.3 ± 0.6	0.58 ± 0.04	Ba69	reorientation
	0.54 ± 0.03	Hä72	Coul.exc.; thick target yield
	0.60 ± 0.07	Gr71	Coul.exc.; thick target yield
	0.69 ± 0.05	Ro74	(e,e')
	0.624 ± 0.04	Fr72	(e,e')
	$0.69 \begin{smallmatrix}+0.06\\-0.03\end{smallmatrix}$	Na72	(e,e')
	0.77 ± 0.09	Na71	(e,e')
	0.72 ± 0.04	Zi68	(e,e')

separation S between the nuclear surfaces is less than the minimum safe distance of about 7.4 fm as established in the present work (see chapter 5). If it is assumed that there is no angular dependence for the minimum safe distance, eq. (5.3) can be used to calculate the surface to surface separation at each angle and energy, and for each projectile. Table 6.5 gives the number of data points which satisfy the conditions $S \gtrsim 7.4$ fm (safe) and $S < 7.4$ fm (unsafe) for each of the data sets 17.5 MeV ^4He, 18 MeV ^4He, and 69.1 MeV ^{16}O; the smallest value of S, which corresponds to the most backward scattering angle used, is also given. The fact that most of the data contained nuclear effects has been recognised by Barnett (Fe76), and optical model

calculations (Fe76) indicate that for $S \approx 5$ fm, Coulomb-nuclear interference in ^{4}He scattering can cause the excitation probability to decrease by about 10% from that of pure Coulomb excitation. This decrease in excitation probability may explain the lower (by about 13%) B(E3) of Barnett and Phillips compared with the present result.

Table 6.5 Number of data points in the work of Barnett and Phillips (Ba69) for which nuclear effects are expected to be small ($S \gtrsim 7.4$ fm) and where nuclear effects are expected to be more than 1% ($S < 7.4$ fm). It is assumed that the minimum safe distance (7.4 fm) is independent of the scattering angle. For each data set, the smallest value of S is also indicated.

Data Set	$S \gtrsim 7.4$ fm	$S < 7.4$ fm	smallest S (fm)
17.5 MeV ^{4}He	1	6	5.4
18.0 MeV ^{4}He	1	8	5.0
69.1 MeV ^{16}O	2	8	5.2

A subsequent experiment by Barnett et al. (Ba72) employed an experimental technique similar to that described in subsection 3.1.1a. A thick natural lead target was bombarded with ^{12}C, ^{20}Ne, ^{32}S, and ^{40}Ar ions with energies 4.15 MeV/A, and decay gamma rays, following Coulomb excitation, were measured with a Ge(Li) detector. The value of Q_{3^-} was determined by comparing the total gamma-ray yields from the decay of the ^{208}Pb 3^- and ^{206}Pb 2^+ states. The result obtained was slightly dependent on the quadrupole moment Q_{2^+} of the 2^+ state

in ^{206}Pb, and since the value of Q_{2+} had not previously been measured, Barnett et al. quoted the values $Q_{3-} = -1.1 \pm 0.4$ eb assuming $Q_{2+} = 0$, and $Q_{3-} = -0.9 \pm 0.4$ eb assuming $Q_{2+} = +0.29$ eb (which is the value predicted by the rotational model; see eq. (1.11)). It is now possible to remove this ambiguity and, from the present measured value $Q_{2+} = +0.05 \pm 0.08$ eb for ^{206}Pb, it is deduced that the quadrupole moment measured by Barnett et al. is $Q_{3-} = -1.1 \pm 0.4$ eb. The discrepancy between this value of Q_{3-} and the value obtained in the present work is possibly explained by the fact that the bombarding energies used by Barnett et al. were above the maximum safe energy. Table 6.6 shows the distance S of separation between nuclear surfaces (for a scattering angle of 180^{o}) for each projectile and bombarding energy; it can be seen that all the values of S in this table are less than the minimum safe distance of 7.4 fm in the present work (see chapter 5). An additional reason for the discrepancy in the values of Q_{3-} is that since heavier projectiles were used in the later work of Barnett et al, their result is likely to be more strongly affected by virtual excitation via the giant dipole resonance, than in

Table 6.6 Distance S of separation between nuclear surfaces in the work of Barnett et al. (Ba72). The values quoted are for a scattering angle of 180^{o}.

Projectile	Bombarding Energy (MeV)	S (fm)
^{12}C	49.8	5.78
^{20}Ne	83	5.85
^{32}S	132.8	6.15
^{40}Ar	166	6.42

the present work where the heaviest projectile used was ^{16}O.

The comparison of B(E3) values in table 6.4 shows that the present value $B(E3; 0^+ \rightarrow 3^-) = 0.665 \pm 0.035\ e^2b^3$ is in reasonable agreement with previous measurements. While most inelastic electron scattering measurements tend to give results higher than the present value, the results from previous Coulomb excitation measurements are all lower. However, as was pointed out before, the latter may be affected by Coulomb-nuclear interference.

6.2.2 Consequence of a Large Value for Q_{3^-}

The large values for Q_{3^-} obtained by Barnett et al. (Ba69, Ba72) are rendered even more unlikely when the effects of such a large quadrupole moment on other features of nuclear structure are considered.

a) Energy splitting of the $(h_{9/2} \times 3^-)$ septuplet.

The coupling of an octupole phonon to the $h_{9/2}$ ground state of ^{209}Bi is expected to give rise to a septuplet of states with spins $J^\pi = 3/2^+, 5/2^+, \ldots, 15/2^+$. The experimentally observed (Un71) energy splitting is given in table 6.7. Hamamoto (Ha75) has been able to obtain good agreement with experiment for most members of the septuplet with the particle-vibration coupling model (The $3/2^+$ state is believed to contain about equal mixtures of the $(d_{3/2}^{-1}\ 0^+)$ and $(h_{9/2}\ 3^-)$ configurations (Bo75,p.570) and an additional coupling term was included in the calculations.); the results of this calculation are listed in table 6.7. In addition to the energy shifts calculated by Hamamoto, one must also consider the energy splitting (Bo75,Ha75) ,

Table 6.7 Energy splitting of the $(h_{9/2}\ 3)$ septuplet in ^{209}Bi. Column 3 refers to the values calculated by Hamamoto (Ha75) as discussed in the text. Columns 4 and 5 are values calculated from eq. (6.1). All values quoted are in MeV.

J^{π}	Expt	Ha75	$Q_{3^-} = -0.42$ eb	$Q_{3^-} = -1.0$ eb
$3/2^+$	- 0.121	- 0.190	- 0.215	- 0.512
$5/2^+$	+ 0.003	+ 0.007	+ 0.117	+ 0.279
$7/2^+$	- 0.030	- 0.006	- 0.008	- 0.019
$9/2^+$	- 0.050	- 0.089	- 0.086	- 0.205
$11/2^+$	- 0.015	- 0.031	+ 0.129	+ 0.307
$13/2^+$	- 0.015	- 0.063	- 0.078	- 0.186
$15/2^+$	+ 0.129	+ 0.156	- 0.117	- 0.279

$$\delta E\left[(h_{9/2}\ 3^-)J\right] = 14\ Q(n_3=1)\ Q(h_{9/2})\ (-1)^{J+\frac{1}{2}} \begin{Bmatrix} 3 & 9/2 & J \\ 9/2 & 3 & 2 \end{Bmatrix} \text{MeV b}^{-2} \qquad (6.1)$$

arising from the interaction of the quadrupole moment of the octupole phonon with the quadrupole moment associated with the $h_{9/2}$ proton. In eq. (6.1) $Q(h_{9/2})$ is the quadrupole moment of the ground state of ^{209}Bi which has been measured to be - 0.35 eb (Fu69). The values calculated from eq. (6.1), assuming $Q_{3^-} = -0.42$ eb and $Q_{3^-} = -1.0$ eb are listed in table 6.7. It can be seen that the energy shifts obtained assuming $Q_{3^-} = -1.0$ eb are unreasonably large and make such a large value for Q_{3^-} unlikely. Even for $Q_{3^-} = -0.42$ eb the energy splitting is larger than experiment; the disagreement is even worse when these values are added to those of column 3 in table 6.7.

Better agreement with experiment would be obtained by reducing the size of the coupling constant (which is incorporated in the factor 14 in eq. (6.1)).

b) Energy splitting of the $(3^- \times 3^-)$ quartet in ^{208}Pb

The simple vibrational model predicts a two-octupole-phonon quartet of degenerate states with spins $J^\pi = 0^+, 2^+, 4^+$, and 6^+ and with excitation energy $2\hbar\omega_3 = 5.23$ MeV. A large static quadrupole moment for the 3^- state would imply strong coupling between octupole and quadrupole motions and would give rise to a substantial splitting of the quartet. Blomqvist (B170) has calculated the amount of splitting and showed that the 0^+ member of the quartet was shifted most from the unperturbed position; if $Q_{3^-} = -0.7$ eb (corresponding to the lower bound set by the errors in Ba69 and Ba72), then the 0^+ state is depressed 1.5 MeV in energy. The particle-vibration coupling model can be used to obtain an expression for the energy shift of a member J of the quartet; using a self-consistent value for the quadrupole coupling constant, Bohr and Mottelson (Bo75, p.570) obtained for ^{208}Pb,

$$\delta E(n_3 = 2, J) \approx -16 \left(Q(n_3 = 1)\right)^2 \begin{Bmatrix} 3 & 3 & 2 \\ 3 & 3 & J \end{Bmatrix} \text{MeV b}^{-2} \qquad (6.2)$$

where n_3 refers to the number of octupole phonons. The calculated excitation energies of the members of the quartet are listed in table 6.8 for the values $Q_{3^-} = -0.42 \pm 0.32$ eb and $Q_{3^-} = -1.1 \pm 0.4$ eb. The lowest 0^+ excited states that have been observed in ^{208}Pb are at 4.87 MeV (Bj66) and at 5.26 MeV (Ig70), and the fact that no 0^+ excited state has been observed at a lower energy

is an argument against a large value of Q_{3-}, although there are large uncertainties in the calculated excitation energies in table 6.8.

Table 6.8 Calculated excitation energies of the members of the two-octupole-phonon quartet in ^{208}Pb. Results (in Mev) are given for the values Q_{3-} obtained in the present work, and obtained by Barnett et al. (Ba72).

J^π	$Q_{3-} = -0.42 \pm 0.32$ eb	$Q_{3-} = -1.1 \pm 0.4$ eb
0^+	4.83 ± 0.61	2.46 ± 2.01
6^+	5.06 ± 0.26	4.08 ± 0.84
2^+	5.10 ± 0.20	4.35 ± 0.64
4^+	5.42 ± 0.29	6.55 ± 0.96

6.2.3 Theoretical Calculations of Q_{3-} and B(E3)

The surprisingly large experimental result for Q_{3-} obtained by Barnett and Phillips (Ba69) has prompted a large number of theoretical investigations. The results of these theoretical studies are listed in table 6.9. It can be seen that the present value $Q_{3-} = -0.42 + 0.32$ eb is in agreement with most theoretical calculations, although these tend to be consistently lower (with the exception of Krainov (Kr68)). If the effect of the giant dipole resonance (GDR), estimated in section 5.5, is taken into account, then the experimental value becomes $Q_{3-} = -0.26$ eb and excellent agreement is obtained with theory. If one further includes the estimated effect of interference from the

Table 6.9 Comparison of experimental and theoretical values for Q_{3^-} and B(E3) for the 2.6 MeV 3^- state in ^{208}Pb. The abbreviations in column 3 are explained in the text.

Q_{3^-} (eb)	$B(E3;0^+\rightarrow 3^-)$ (e^2b^3)	Model	Ref.	Comments
-0.42 ± 0.32	0.665 ± 0.035		this work	experiment
	0.149	TDA	Le66	surface delta interaction
	0.349	RPA	Le66	
	0.11 - 0.13	TDA	Gi66	value depends on
	0.23 - 0.55	RPA	Gi66	interaction
-0.09			B170	Gi66 wave function
-0.10			B170	Kuo wave function
	0.372, 0.709, 0.682	RPA	B168	separable interaction
-0.12		coupled	So71	separable interaction
	0.58	RPA phonons	So71	
-0.52, -0.79		FFS	Kr68	
-0.21		FFS	Sp72	
-0.17	0.55	FFS	Sp73	
-0.20		PVC	Ha70	
-0.14		PVC	Ha75	
-0.10		PVC	Bo75	

4.09 Mev 2^+ state (see section 5.5), then one obtains $Q_{3^-} = -0.27$ eb for constructive interference ($P_4 = -1$) and $Q_{3^-} = -0.19$ eb for destructive interference ($P_4 = +1$). It can therefore be concluded that the present experimental result has resolved the discrepancy between theory and experiment, and that including the effects of the GDR and of the 4.09 MeV 2^+ state would further improve the agreement. Nevertheless, it is instructive to investigate the possible reasons

which, so far, have prevented theoretical calculations from predicting large values of Q_{3-}.

The original discrepancy between theory and the experimental results of Barnett et al. (Ba69, Ba72, Ba72a) led Guidetti et al. (Gu75) to find lower and upper bounds for the values of Q_{3-} and B(E3) which could be predicted by calculations based on the particle-hole model or on models where particle-hole excitations are coupled to a quadrupole phonon. The results of the investigation by Guidetti et al., which are independent of the Hamiltonian used in the models, are shown in fig. 6.3. Although both neutron and proton particle-hole configurations can make up a nuclear state, Guidetti et al. did not assume an effective charge for the neutron, and only proton particle-hole configurations were considered to calculate lower and upper bounds for Q_{3-} and B(E3). Consequently, points located on the "extremum curves" in fig. 6.3 correspond to a state with pure proton particle-hole configurations; such a state would be physically unlikely.

Fig. 6.3a shows that in the particle-hole model, Tamm-Dancoff approximation (TDA) calculations with a small particle-hole space are inadequate to describe the experimental B(E3). This observation is substantiated by the TDA results of Letourneux and Eisenberg (Le66) and Gillet et al. (Gi66). For TDA calculations to successfully reproduce the observed Q_{3-} and B(E3), particle-hole configurations up to $3\hbar\omega$* excitation would be required. The results from the random-

---

* Each major shell can loosely be considered to be separated from its neighbours by an energy $\hbar\omega$, which is the case for the pure harmonic oscillator shell model. Thus, particle-hole excitations up to $3\hbar\omega$ would consider all single-particle orbits of the 3 major shells above and below the Fermi surface.

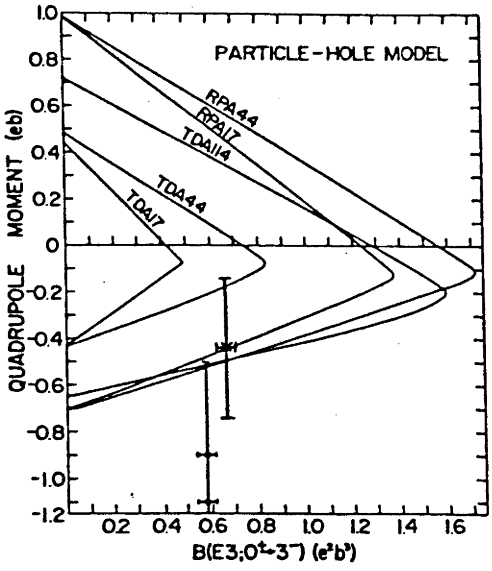

(a)

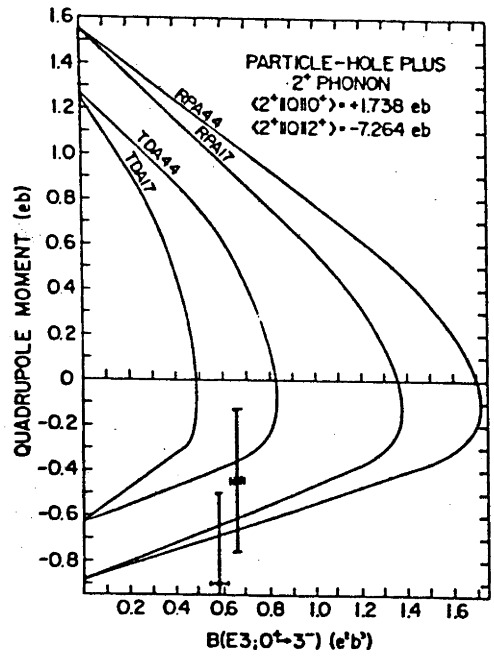

(b)

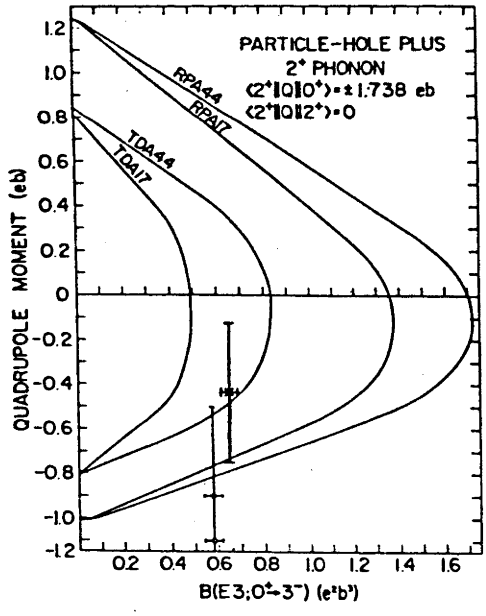

(c)

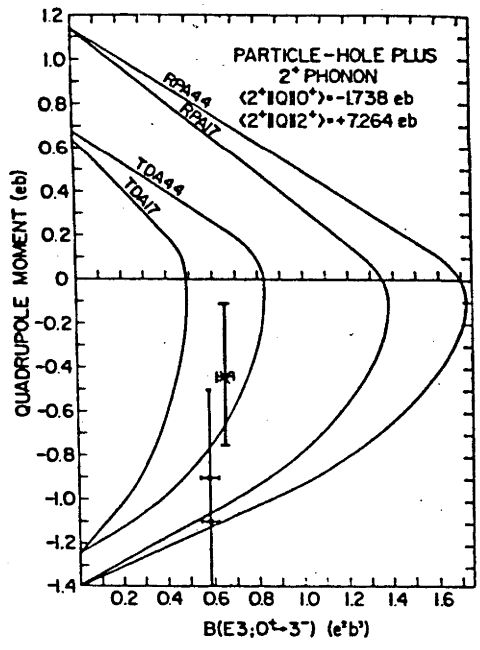

(d)

Fig. 6.3 Extremum curves for the particle-hole model (a), and for the particle-hole 2^+ phonon model (b)(c)(d), as calculated by Guidetti et al. (Gu75). The curves are labelled by the dimensions of the particle-hole space and according to whether it is treated in TDA or RPA. Circles indicate the results of Barnett et al. (Ba72) and crosses indicate the present results.

phase approximation (RPA) calculations of Gillet et al.(Gi66) and Kuo have been used by Blomqvist (Bl70) to deduce theoretical quadrupole moment values of - 0.09 eb and - 0.10 eb respectively; to predict larger values for Q_{3-}, more particle-hole configurations would need to be included. The results of RPA calculations by Letourneux et al. and by Gillet et al. for B(E3) are also too small, and Blomqvist (Bl68) has shown that the inclusion of $3\hbar\omega$ excitations can substantially increase the B(E3) so that it is brought into good agreement with experiment (including $5\hbar\omega$ excitations has relatively little effect).

Sorensen (So71) has predicted a value - 0.121 ± 0.024 eb for Q_{3-}, using a model where particle-hole states are coupled to a quadrupole phonon. The analysis of Guidetti et al., for this model, requires the knowledge of the values of the B(E2) and quadrupole moment of the 4.09 MeV 2^+ state in ^{208}Pb. Although the value $B(E2; 0^+ \rightarrow 2^+) = 0.30 \pm 0.02\ e^2b^2$ has been measured (Zi68), the value of the quadrupole moment has not and therefore Guidetti et al. performed calculations for the value $Q_{2+} = 0$ eb predicted by the vibrational model, and for the two values $Q_{2+} = \pm 0.5$ eb predicted by the rotational model; the results of these calculations are shown in figs. 6.3b, c, and d. The true quadrupole moment is expected to be somewhere between the rotational limits, but in view of the experimental results for Q_{2+} in ^{204}Pb and ^{206}Pb, and in view of theoretical calculations which predict $Q_{2+} = + 0.09$ eb (Sp73, Ri74, So70), Q_{2+} in ^{208}Pb is more likely to have a small positive value. Therefore fig. 6.3c is more likely to represent the real situation. It can be concluded that RPA calculations which include coupling of particle-hole excitations with a quadrupole phonon should be able to

reproduce the experimental values of Q_{3-} and B(E3) even with few particle-hole configurations.

The theory of finite Fermi systems (FFS) (Mi67) has been used by Krainov (Kr68) to calculate Q_{3-} but the units employed are not defined; the calculated value is either - 0.52 eb (see So71) or - 0.79 eb (see Ba72). Krainov's predicted value(s), which is(are) the only one(s) to agree with both the present experimental result and that of Barnett et al. (Ba69, Ba72), is(are) surprisingly large. Other calculations, performed by Speth, with the theory of finite Fermi systems predict the smaller values $Q_{3-} = -0.21$ eb (Sp72) and $Q_{3-} = -0.17$ eb (Sp73, Ri74). Both the work of Krainov and Speth included particle-hole configurations up to $2\hbar\omega$ excitation. However, the selection rules suggested by Bohr and Mottelson (Bo75, p.470) indicate that including $3\hbar\omega$ excitations could have a significant effect on the calculated values of Q_{3-} and B(E3).

Finally, Hamamoto has predicted the values $Q_{3-} = -2.0$ eb (Ha70) and $Q_{3-} = -0.14$ eb (Ha75) (the reason for the differing values is not stated) using the particle-vibration coupling (PVC) model. With the same model, Bohr and Mottelson (Bo.75, P.569) estimate a value $Q_{3-} \approx -0.10$ eb.

6.3 Conclusion

The present work has considerably improved the knowledge of the static and transition moments of the even-mass lead isotopes. The previously unknown quadrupole moment Q_{2+} of ^{206}Pb has now been measured. The quadrupole moment Q_{2+} of ^{204}Pb has been determined with a smaller uncertainty and with the inclusion of more excited states in

the analysis, than the previous measurement of Olin et al. (Ol74). For both ^{204}Pb and ^{206}Pb, the reduced excitation probabilities B(E2; $0^+ \rightarrow 2^+$) measured in the present work have been found to agree with previous Coulomb excitation measurements. Up to now, no single theoretical calculation has correctly predicted Q_{2+} for both ^{204}Pb and ^{206}Pb; now that both these quadrupole moments have been measured, renewed theoretical interest in these nuclei may be expected.

The controversy regarding the quadrupole moment of the first 3^- state of ^{208}Pb has been resolved by the present experimental result which is a factor of three smaller than the values from previous measurements. The present value of Q_{3-} now agrees with theoretical calculations. It has been suggested that the previous experiments of Barnett et al. may have been subject to Coulomb-nuclear interference effects, which would also explain the low value of B(E3; $0^+ \rightarrow 3^-$) which was obtained. Most theoretical calculations give values of Q_{3-} which are consistently lower in magnitude than the experimental values; to obtain larger values, more particle-hole configurations need to be included. On the other hand, it has been shown that including the effect of virtual excitation via the giant dipole resonance would bring the present value of Q_{3-} in yet closer agreement with theory. Some remaining uncertainties in the present experimental results are the size of the quantum-mechanical correction to be applied, the effect of the giant dipole resonance, the effect of virtual nucleon tunnelling, and the maximum safe bombarding energy for the ^{4}He data. These questions remain a challenge for further theoretical and experimental investigations.

REFERENCES

A156 K. Alder, A. Bohr, T. Huus, B. Mottelson, and A. Winther, Rev. Mod. Phys. 28 (1956) 432.

A167 J. Alster, Phys. Lett. 25B (1967) 459.

A169 K. Alder and H.K.A. Pauli, Nucl. Phys. A128 (1969) 193.

A172 K. Alder, F. Roesel, and R. Morf, Nucl. Phys. A186 (1972) 449.

A175 K. Alder and A. Winther, "Electromagnetic Excitation Theory of Coulomb Excitation with Heavy Ions", (North Holland, Amsterdam, 1975).

Ba69 A.R. Barnett and W.R. Phillips, Phys. Rev. 186 (1969) 1205.

Ba71 A.R. Barnett, W.R. Phillips, P.J.A. Buttle, and L.J.B. Goldfarb, Nucl. Phys. A176 (1971) 321.

Ba72 A.R. Barnett, S.F. Biagi, D.K. Olsen, and W.R. Phillips, Proc. Int. Conf. on Nuclear Moments and Nuclear Structure, Osaka, 1972.

Ba72a A.R. Barnett, S.F. Biagi, D.K. Olsen, and W.R. Phillips, Annual Report, Shuster Lab., Manchester, Sept. 1972.

Ba76 F.T. Baker, A. Scott, T.H. Kruse, W. Hartwig, E. Ventura, and W. Savin, Phys. Rev. Lett. 37 (1976) 193.

Be60 I. Bergström, E.C.O. Bonacalza, A. Jech, M. Perez, and P. Thieberger, Nucl. Inst. Meth. 8 (1960) 151.

Be69 P.R. Bevington, "Data Reduction and Error Analysis for the Physical Sciences" (McGraw-Hill, New York, 1969).

Be70 R. Beyer, R.P. Scharenberg, and J. Thomson, Phys. Rev. C2 (1970) 1469.

Be75 L. von Bernus, W. Greiner, V. Rezwani, W. Scheid, U. Schneider, M. Sedlmayr, and R. Sedlmayr, in "Problems of Vibrational Nuclei", G. Alaga, V. Paar, and L. Sips eds, (North Holland, Amsterdam, 1975).

Bi65 L. C. Biedenharn and P.J. Brussaard, "Coulomb Excitation", (Clarendon Press, Oxford, 1965).

Bj66 J.H. Bjerregaard, O. Hansen, O. Nathan, and S. Hinds, Nucl. Phys. 89 (1966) 337.

B168 J. Blomqvist, Phys. Lett. 28B (1968) 22.

B170 J. Blomqvist, Phys. Lett. 33B (1970) 541.

B172 J. Bleck, R. Butt, H. Haas, W. Ribbe, and W. Zeitz, Phys. Rev. Lett. 29 (1972) 1371.

Bo53 A. Bohr and B.R. Mottelson, Kgl. Danske Videnskab. Selskab Mat. fys. Medd. 27 (1953) 665.

Bo75 A. Bohr and B.R. Mottelson, "Nuclear Structure" vol. II, (Benjamin, Reading, Mass., 1975).

Bo75a E. Bodenstedt, in "The Electromagnetic Interaction in Nuclear Spectroscopy", W.D. Hamilton ed.,(North Holland, Amsterdam, 1975).

Br55 G. Breit and J.P. Lazarus, Phys. Rev. 100 (1955) 942.

Br56 G. Breit, R.L. Glückstern, and J.E. Russell, Phys. Rev. 103 (1956) 727.

Br72 R.A. Broglia, R. Liotta, and V. Paar, Phys. Lett. 38B (1972) 480.

Bu72 F.R. Buskirk, H.D. Gräf, R. Pittham, H. Theissen, O. Titze, and Th. Walcher, Phys. Lett. 42B (1972) 194.

Ca64 E.B. Carter, G.E. Mitchell, and R.H. Davis, Phys. Rev. 133 (1964) B1421.

Ch72 A. Christy and O. Häusser, Nucl. Data Tables A11 (1972) 281.

C172 D. Cline and C. Flaum, in Int. Conf. on Nuclear Structure Studies using Electron Scattering and Photoreactions, Sendai, 1972.

C172a D. Cline, Proc. Int. Conf. on Nuclear Moments and Nuclear Structure, Osaka, 1972.

Co71 B.L. Cohen, "Concepts of Nuclear Physics", (McGraw-Hill, New York, 1971).

Da58 A.S. Davydov and G.F. Filippov, Nucl. Phys. 8 (1958) 237.

deBo65 J. de Boer, R.G. Stokstad, G.D. Symons, and A. Winther, Phys. Rev. Lett 14 (1965) 564.

deBo68 J. de Boer and J. Eichler, in "Advances in Nuclear Physics" vol. 1, M. Baranger and E. Vogt eds, (Plenum Press, New York, 1968).

deMe73 R.J. de Meijer and H.W. Schreuder, in K.V.I. Annual Report, Jülich, 1973.

Di66 P.A.M. Dirac, "The Principles of Quantum Mechanics" 4th ed., (Oxford Univ. Press, 1966), p.167 ff.

Ei64 J. Eichler, Phys. Rev. 133 (1964) B1162.

Es76 M.T. Esat, Ph.D. Thesis, Australian National University, Canberra, 1976.

Fa76 C. Fahlander, L. Hasselgren, J.E. Thun, A. Bockisch, A.M. Kleinfeld, A. Gelberg, and K.P. Lieb, Phys. Lett. 60B (1976) 347.

Fe76 D.H. Feng, A.R. Barnett, and L.J.B. Goldfarb, Phys. Rev. C13 (1976) 1151.

Fe77 M.P. Fewell, D.C. Kean, R.H. Spear, and A.M. Baxter, J. Phys. G 3 (1977) L27.

Fe77a M.P. Fewell, private communication.

Fo54 L.L. Foldy and E. Eriksen, Phys. Rev. 95 (1954) 1048.

Fr69 N. Freed and W. Rhodes, Nucl. Phys. A126 (1969) 481.

Fr72 J. Friedrich, Nucl. Phys. A191 (1972) 118.

Fu69 G.H. Fuller and V.W. Cohen, Nucl. Data Tables A5 (1969) 433.

Gi66 V. Gillet, A.M. Green, and E.A. Sanderson, Nucl. Phys. 88 (1966) 321.

Gö70 U. Götz, J. Hadermann, and K. Alder, Helv. Phys. Acta 43 (1970) 514.

Go75 J.D. Goss, C.P. Browne, A.A. Rollefson, and P.L. Jolivette, Phys. Rev. C11 (1975) 710.

Gr70 L. Grodzins, and O. Klepper, Phys. Rev. C3 (1970) 1019.

Gr71 E. Grosse, M. Dost, K. Haberkant, J.W. Hertel, H.V. Klapdor, H.J. Körner, D. Proetel, and P. von Brentano, Nucl. Phys. A174 (1971) 525.

Gr73 L. Grodzins, B. Herskind, D.R.S. Somayajulu, and B. Skaali, Phys. Rev. Lett. 30 (1973) 453.

Gu75 M. Guidetti, D.J. Rowe, and H. Chow, Nucl. Phys. A238 (1975) 225.

Ha64 R.R. Harvey, J.T. Caldwell, R.L. Bramblett, and S.C. Fultz, Phys. Rev. 136 (1964) B126.

Ha67 J. Hadermann and M. Simonius, Helv. Phys. Acta 40 (1967) 531.

Ha68 J. Hadermann, Helv. Phys. Acta 41 (1968) 323.

Ha69 J. Hadermann and K. Alder, Helv. Phys. Acta 42 (1969) 497.

Ha69a H.J. Hay, in "Least Squares Methods in Data Analysis", R.S. Anderssen and M.R. Osborne eds., Australian National University Computer Centre Publication CC2/69, 1969.

Ha70 I. Hamamoto, Nucl. Phys. A155 (1970) 362.

Hä70a O. Häusser and D. Ward, Atomic Energy of Canada Limited, Physics Division Progress Report, AECL-3668, 1970.

Hä72 O. Häusser, F.C. Khanna, and D. Ward, Nucl. Phys. A194 (1972) 113.

Hä73 O. Häusser, T.K. Alexander, D.L. Disdier, A.J. Ferguson, A.B. McDonald, and I.S. Towner, Nucl. Phys. A216 (1973) 617.

Hä74 O. Häusser, in "Nuclear Spectroscopy and Reactions" part C, J. Cerny ed., (Academic Press, New York, 1974).

Ha75 I. Hamamoto, in "Problems of Vibrational Nuclei", G. Alaga, V. Paar, and L. Sips eds, (North Holland, Amsterdam, 1965).

Ha76 L. Hasselgren, C. Fahlander, F. Falk, L.O. Edvardson, J.E. Thun, B.S. Ghuman, and B. Skaali, Nucl. Phys. A264 (1976) 341.

He71 B. Herskind, in "Hyperfine Interactions in Excited Nuclei" vol. 4, G. Goldring and R. Kalish eds, (Gordon and Breach, New York, 1971).

Hr66 A.Z. Hrynkiewicz, S. Kopta, S. Szymczyk, T. Walczak, and I. Kuzniecov, Nucl. Phys. 79 (1966) 495.

Hu67 W.E. Hunt, M.K. Mehta, and R.H. Davis, Phys. Rev. 160 (1967) 782.

Hu73 E. Huenges, H. Rösler, and H. Vonach, Phys. Lett. 46B (1973) 361.

Hy64 E.K. Hyde, I. Perlman, and G.T. Seaborg, "The Nuclear Properties of the Heavy Elements" vol. I chpt. 3, (Prentice-Hall, New Jersey, 1964).

Ig70 G.J. Igo, P.D. Barnes, and E.R. Flynn, Phys. Rev. Lett.24 (1970) 470.

Ij64 M.A. Ijaz, P.B. Weiss, R.H. Davis, and R. Ijaz, J. Nat. Sc. and Math. 4 (1964) 1.

Iv69 M. Ivascu, G. Semenescu, D. Bucurescu, and M. Titirici, Rev. Roum. Phys. 14 (1969) 129.

Ja62 J.D. Jackson, "Classical Electrodynamics", (Wiley, New York, 1962).

Ja72 P. Jagam and D.S. Murty, Nucl. Phys. A197 (1972) 540.

Jo69 J. John, J.P. Aldridge, and R.H. Davis, Phys. Rev. 181 (1969) 1455.

Kl73 V. Klemt and J. Speth, K.V.I. Annual Report, Jülich, 1973.

Kl75 A.M. Kleinfeld, in "Problems of Vibrational Nuclei", G. Alaga, V. Paar, and L. Sips eds, (North Holland, Amsterdam, 1975).

Ko76 W.K. Koo and L.J. Tassie, Phys. Lett. 64B (1976) 9.

Kr67 J.J. Kraushaar, R.A. Ristinen, and R. Smythe, Phys. Lett. 25B (1967) 13.

Kr68 V.P. Krainov, Phys. Lett. 27B (1968) 341.

Ku69 K. Kumar, Phys. Lett. 29B (1969) 25.

Ku71 T.T.S. Kuo and G.H. Herling, Naval Research Laboratory Memorandum Report no. 2258, 1971 (unpublished).

Ku72 K. Kumar, Phys. Rev. Lett. 28 (1972) 249.

Ku75 K. Kumar, in "The Electromagnetic Interaction in Nuclear Spectroscopy", W.D. Hamilton ed., (North Holland, Amsterdam, 1975).

La72 R.D. Larsen, J.A. Thomson, R.G. Kerr, R.P. Scharenberg, and W.R. Lutz, Nucl. Phys. A195 (1972) 119.

Le57 J.S. Levinger, Phys. Rev. 107 (1957) 554.

Le66 J. Letourneux and J.M. Eisenberg, Nucl. Phys. 85 (1966) 119.

Le71 M.B. Lewis, Nucl. Data Sheets B5 (1971) 243.

Li67 R.M. Lieder, W. Delang, and M. Fleck, Z. Phys. 206 (1967) 29.

Ma55 M.G. Mayer and J.H.D. Jensen, "Elementary Theory of Nuclear Shell Structure" p.231, (Wiley, New York, 1955).

Ma71 M.J. Martin, Nucl. Data Sheets B5 (1971) 601.

Ma72 J.C. Manthuruthil, D.C. Camp, A.V. Ramayya, J.H. Hamilton, J.J. Pinajian, and J.W. Doornebos, Phys. Rev. C6 (1972) 1870.

Ma75 N. Marty, M. Morlet, A. Willis, V. Comparat, and R. Frascaria, Nucl. Phys. A238 (1975) 93.

McGo74 F.K. McGowan and P.H. Stelson, in "Nuclear Spectroscopy and Reactions" part C, J. Cerny ed., (Academic Press, New York, 1974).

McGr75 J.B. McGrory and T.T.S. Kuo, Nucl. Phys. A247 (1975) 283.

Mi62 J. Miller, C. Schuhl, and C. Tzara, Nucl. Phys. 32 (1962) 236.

Mi67 A.B. Migdal, "Theory of Finite Fermi Systems and Applications to Atomic Nuclei", (Interscience, New York, 1967).

Mi70 J.C.D. Milton, G.C. Ball, W.G. Davies, A.J. Ferguson, and J.S. Frazer, Atomic Energy of Canada Limited, Report AECL-3563, 1970.

Mo66 J.M. Morris and T.R. Ophel, Nucl. Instr. Meth. 40 (1966) 245.

Mo69 J.M. Morris and T.R. Ophel, Nucl. Instr. Meth. 68 (1969) 344.

My73 W.D. Myers, Nucl. Phys. A204 (1973) 465.

Na71 M. Nagao and Y. Torizuka, Phys. Lett. 37B (1971) 383.

Na72 M. Nagao, in Int. Conf. on Nuclear Structure Studies using Electron Scattering and Photoreactions, Sendai, 1972.

Na73 M. Nagao and Y. Torizuka, Phys. Rev. Lett. 30 (1973) 1068.

Ne75 J.O. Newton, in "The Electromagnetic Interaction in Nuclear Spectroscopy", W.D. Hamilton ed., (North Holland, Amsterdam, 1975).

No70 L.C. Northcliffe and R.F. Schilling, Nucl. Data Tables A7 (1970) 233.

O'Br77 J.J. O'Brien, J.X. Saladin, C. Baktash, and J.G. Alessi, Phys. Rev. Lett. 38 (1977) 324.

Ol74 A. Olin, O. Häusser, T.K. Alexander, A.J. Ferguson, and W. Witthuhn, Nucl. Phys. A221 (1974) 555.

Op74 T.R. Ophel, J.S. Harrison, J.O. Newton, R.H. Spear, E.W. Titterton, and D.C. Weisser, in "Large Electrostatic Accelerators", D.A. Bromley, ed., (North Holland, Amsterdam, 1974).

Op75 T.R. Ophel, Australian National University Internal Report ANU-P/610, 1975.

OR72 Oak Ridge National Laboratory, Physics Division Annual Report, ORNL-4844, p.61 ff, 1972.

Ov69 J.C. Overley, P.D. Parker, and D.A. Bromley, Nucl. Instr. Meth. 68 (1969) 61.

Pa69 A. Pakkanen, J. Kantele, and P. Suominen, Z. Phys. 218 (1969) 273.

Pi74 R. Pitthan, F.R. Buskirk, E.B. Dally, J.N. Dyer, and X.K. Maruyama, Phys. Rev. Lett. 33 (1974) 849.

Po76 E.C. Pollaco, Ph.D. Thesis, Australian National University, Canberra, 1976.

Qu70 J.L. Quebert, N. Nakai, R.M. Diamond, and F.S. Stephens, Nucl. Phys. A150 (1970) 68.

Ri74 P. Ring and J. Speth, Nucl. Phys. A235 (1974) 315.

Ro74 H. Rothhaas, J. Friedrich, K. Merle, and B. Dreher, Phys. Lett. 51B (1974) 23.

Ry51 A. Rytz, Com. Rend. Acad. Sc. Paris 233 (1951) 790.

Sa63 M. Salomon, L. Boström, T. Lindqvist, E. Matthias, and M. Perez, Nucl. Phys. 46 (1963) 377.

Sa69 J.X. Saladin, J.E. Glenn, and R.J. Prior, Phys. Rev. 186 (1969) 1241.

Se72 K.K. Seth, Nucl. Data Sheets B7 (1972) 161.

Se73 P.T. Sewell, J.C. Hafele, C.C. Foster, N.M. O'Fallon, and C.B. Fulmer, Phys. Rev. C7 (1973) 690.

Si72 C. Signorini and H. Morinaga, Phys. Lett. 40B (1972) 549.

Sk67 S.J. Skorka, J. Hertel, and T.W. Retz-Schmidt, Nucl. Data Tables A2 (1967) 347.

So70 B. Sorensen, Nucl. Phys. A142 (1970) 411.

So71 B. Sorensen, Phys. Lett. 35B (1971) 101.

Sp67 J.E. Spencer, H.A. Enge, Nucl. Instr. Meth. 49 (1967) 181.

Sp72 J. Speth, as quoted in Ba72a.

Sp73 J. Speth, in Proc. Int. Conf. on Nuclear Moments and Nuclear Structure, Osaka, 1972.

Sp76 R.H. Spear, D.C. Kean, A.M.R. Joye, and M.P. Fewell, Australian National University Internal Report ANU-P/651; to be published in Nucl. Instr. Meth.

Sp77 R. H. Spear, J.P. Warner, A.M. Baxter, M.T. Esat, M.P. Fewell, S. Hinds, A.M.R. Joye, and D.C. Kean, Australian National University Internal Report ANU-P/657; to be published in Aust. J. Phys.

St67 R.G. Stokstad, I. Hall, G.D. Symons, and J. de Boer, Nucl. Phys. A92 (1967) 319.

St70 S.G. Steadman, A.M. Kleinfeld, G.G. Seaman, J. de Boer and D. Ward, Nucl. Phys. A155 (1970) 1.

Ta62 K. Takahashi and K. Kotajima, J. Phys. Soc. Jap. 17 (1962) 1815.

To68 T. Tomimasu, J. Phys. Soc. Jap. 25 (1968) 655.

Tr68 W.W. True, Phys. Rev. 168 (1968) 1388.

Un71 J. Ungrin, R.M. Diamond, P.O. Tjom, and B. Elbek, Danske Videnskab. Selskab Mat. fys. Medd. 38 no. 8 (1971).

Va71 J. Vary and J.N. Ginocchio, Nucl. Phys. A166 (1971) 479.

Ve70 A. Veyssiere, H. Beil, R. Bergere, P. Carlos, and A. Lepretre, Nucl. Phys. A159 (1970)561.

Wa64 A.H. Wapstra, Nucl. Phys. 57 (1964) 48.

We62 R.S. Weaver, Can. J. Phys. 40 (1962) 1684.

Wi66 A. Winther and J. de Boer, in "Coulomb Excitation", K. Alder and A. Winther eds, (Academic Press, New York, 1966).

Za72 L. Zamick, as quoted in Ba72a.

Zi68 J.F. Ziegler and G.A. Peterson, Phys. Rev. 165 (1968) 1337.